Instability of Elliptic Liquid Jets

GHOBAD AMINI-BAZIANI

A Thesis

in

the Department

of

Mechanical and Industrial Engineering

Presented in Partial Fulfillment of the Requirements
for the Degree of Doctor of Philosophy (Mechanical Engineering) at
Concordia University
Montreal, Quebec, Canada

December 2011

Concordia University
School of
Graduate Studies

This is to certify that the thesis prepared

By: **GHOBAD AMINI-BAZIANI**
Entitled: **Instability of Elliptic Liquid Jets**

and submitted in partial fulfillment of the requirements for the degree of

Doctor of Philosophy (Mechanical Engineering)

Complies with the regulations of the University and meets the accepted standards with respect to originality and quality.

Signed by the final examining committee:

Dr. _____ Chair

Dr. Nasser Ashgriz _____ External Examiner

Dr. Amir G. Aghdam _____ External to Program

Dr. Georgios H. Vatistas _____ Examiner

Dr. Lyes Kadem _____ Examiner

Dr. Ali Dolatabadi _____ Thesis Supervisor

Approved by _____

PhD. Program Director,
Department of Mechanical and Industrial Engineering

_____ _____

Dean of Faculty

Abstract

INSTABILITY OF ELLIPTIC LIQUID JETS

GHOBAD AMINI-BAZIANI

The motion of liquid jets ejected from elliptical orifices is studied theoretically and experimentally. In the theoretical part of the study, the linear evolution of initially small disturbances on the inviscid jets is investigated using a three-dimensional analysis. In addition, to study the viscous free-surface flows, an approach based on the Cosserat theory (also called directed theory) is used. Temporal and spatial analyses are performed and the dispersion equations of waves on the jet column are derived to show the growth rate of disturbances for different modes under various conditions. An equation for the jet profile is suggested which describes the axis-switching phenomenon and breakup for various conditions. The equations are approximated for small and large ellipticities, and well-known dispersion relations of circular and planar jets are retrieved. It is shown that in the capillary dominant regimes, the effect of ellipticity is increasing the growth rate and range of unstable wavenumbers. In this case only modes symmetric to both major and minor axes are unstable. At higher Weber numbers, as the aerodynamic forces become dominant, by increasing the ellipticity, growth rate is decreased. In these Weber numbers, as the ellipticity increases, the growth rates of the modes that are symmetric with respect to the major axis are larger than those of antisymmetric with respect to the major axis. Increasing the gas to liquid density ratio increases the disturbances growth rate, while increasing the liquid viscosity dampens the growth rate and shifts the maximum growth rate toward longer waves. Experiments are performed to validate the linear results and to investigate the jet velocity profile. Several nozzles with different ellipticities and length to diameter

ratios are designed and their behaviors are examined under free (natural) and excited (forced) perturbations. The spatial evolution of the jet shape is captured using a high speed camera. In the forced breakup case, the stimulations are performed by modulating the jet velocity with a piezoelectric actuator through given sinusoidal perturbations. The measured data are in good agreement with theoretical predictions except at high ellipticities where nonlinear effects are strong.

Acknowledgements

I would like to thank my supervisor Dr. Ali Dolatabadi for all the help he has provided me throughout the course of my PhD. His advice has been invaluable to the completion of my thesis. I would also like to thank my committee members for their useful feedback and advice on thesis. The useful comments of Shahin Ghomeshi, Mohsen Najafi, and Carole El Ayoubi are greatly acknowledged. The technical assistance of Gilles Huard, Jordan Lafreniere, and Hadi Alaee is appreciated too. This work is partially supported by *Natural Sciences and Engineering Research Council of Canada (NSERC)*.

Table of Contents

List of figures

List of tables

Nomenclature

a	semi-major axis of nozzle
b	semi-minor axis of nozzle, sheet half-thickness, jet radius
Ce	cosine elliptic function
D	jet equivalent diameter ($2\sqrt{ab}$)
e	aspect ratio (b/a)
h	half of focal length
I_m	modified Bessel function of the first kind of order m
K	dimensionless wavenumber in axial direction (kR)
k	wavenumber in axial direction ($2\pi/\lambda$)
K_m	modified Bessel function of the second kind of order m
L	nozzle length
m	azimuthal mode number (wavenumber in θ direction)
Oh	*Ohnesorge* number ($\mu_l / \sqrt{\rho_l R \sigma}$)
p	pressure
Q	gas to liquid density ratio (ρ_g / ρ_l)
r	radial distance from jet's central axis
R	jet equivalent radius ($\sqrt{ab}$)
Re	jet *Reynolds* number ($\rho_l V R / \mu_l$)
Se	sine elliptic function
t	time
V	mean jet velocity (in z-direction)
We	jet *Weber* number ($\rho_l V^2 R / \sigma$)
x	transverse major-axis direction
y	transverse minor-axis direction
z	axial direction
Z_b	breakup length (liquid contact length)

Greek letters:

α	growth rate
β	dimensionless frequency, *Strouhal* number ($\alpha b / V$)
ω	dimensionless growth rate ($\alpha\sqrt{\rho_l R^3 / \sigma}$)
σ	surface tension coefficient
κ	curvature
μ	liquid dynamic viscosity
θ	azimuthal angle
η	interface displacement (disturbance amplitude)
λ	wavelength
ρ	density, radial component of elliptical coordinate system
ϕ_1	semi-major axis
ϕ_2	semi-minor axis
ϕ	velocity potential
δ_1	dimensionless major axis
δ_2	dimensionless minor axis
ζ_1	velocity of director in the major axis direction
ζ_2	velocity of director in the minor axis direction

Subscripts:

0	initial property
g	gas property
l	liquid property

"The history of science teaches only too plainly the lesson that no single method is absolutely to be relied upon, that sources of error lurk where they are least expected, and that they may escape the notice of the most experienced and conscientious worker."

Sir John William Strutt, Lord Rayleigh (1842-1919)

Chapter 1

Introduction

Liquid jet breakup is important in many practical applications such as the combustion of liquid fuels, ink-jet printing, coatings, painting, and agricultural systems. The breakup of a liquid into a spray increases the surface area of the liquid and subsequently increases the heat and mass transfer between the liquid and gas phases. As an example, in diesel engines, the combustion rate is controlled by the effective vaporization of the fuel which is a strong function of the liquid fuel atomization process.

The breakup of a liquid stream injected through a nozzle into a gas has been studied extensively. Previous studies have shown that the spray properties are influenced by a number of parameters, including the nozzle internal flow effects resulting from cavitation, the jet velocity profile, turbulence at the nozzle exit, and the thermodynamic states of both liquid and gas. Due to the influence of these large numbers of parameters, the governing mechanism of liquid jet breakup is not well understood and research on fragmentation is still an ongoing topic. As

categorized by Sirignano & Mehring (2000), there are four forces acting on the liquid that are typically important in liquid breakup. These forces are inertia, ρL^2V^2, surface tension, σL, viscous, μLV and gravity, $\rho L^3 g$; where L is the characteristic length of the jet (jet radius, in this work), V is the jet velocity, and g is the gravitational acceleration. In addition, ρ, σ, and μ are liquid properties representing density, dynamic viscosity, and surface tension coefficients, respectively. These four forces result in three independent non-dimensional groups: Reynolds number, $Re=\rho LV/\mu$, Weber number, $We = \rho LV^2/\sigma$, and Froude number, $Fr=V^2/gL$. Another number commonly used is the Ohnesorge number defined as $Oh=We^{0.5}/Re$.

The required energy to break up the bulk of the liquid into droplets can be provided through various mechanisms such as liquid pressure, air pressure, vibration, acoustics, and electric fields. Various types of injectors have been designed to inject the liquid streams with sufficient energy. However, the motion of the bulk of a liquid in another immiscible fluid is mainly either in form of circular jets or planar sheets. In the present chapter, the instability and breakup of liquid streams are reviewed and the behavior of circular jets and planar sheets is presented. Literature is also reviewed to study the behavior of elliptic jets, as an intermediate configuration between circular and planar shapes. Meanwhile, a brief explanation of the Cosserat theory is presented which will be used later in the analysis of viscous elliptic jets.

1.1 Circular liquid jets

The jet breakup phenomena have been classified into several regimes that reflect the differences in the appearance of jets as the operating conditions are changed. These regimes are the result of the action of the dominant forces on the jet, leading to its breakup. The most common way of categorizing the circular jet disintegration mechanisms is given by the jet

breakup curve. This curve includes the breakup length Z_b of the jet as a function of the average emerging velocity, V. The plot is sometimes referred to as the jet stability curve. The length of the continuous jet attached to the nozzle, i.e. the coherent portion of the jet, is defined as the breakup length. An analysis of the dynamics of jet stability has as its primary goal the prediction of the breakup length after which the first drops appear. The average emerging velocity is the jet volume flow rate divided by the cross-sectional area of the nozzle exit. The general shape of the breakup curve is schematized in figure 1.1, from which five separate breakup regimes are identified. These regimes are characterized by the dripping (region A), the Rayleigh (region B), the first wind-induced (region C), the second wind-induced (region D), and the atomization (region E) regimes. These breakup regimes correspond to different combinations of liquid inertia, surface tension, viscous, and aerodynamic forces acting on the jet. Table 1.1 categorizes the different regimes based on Weber number (We), Ohnesorge number (Oh), and gas to liquid density ratio (Q).

The first region, dripping regime (region A), corresponds to the situation where individual drops are formed and emitted from the nozzle exit, without the existence of any continuous liquid column or definable jet length. The dripping from the nozzle exit no longer occurs if the liquid inertia force becomes greater than the surface tension force, leading to a limit in terms of We for the region A as shown in table 1-1. As the jet velocity is increased, the Rayleigh regime (region B, figure 1.1) appears. Rayleigh (1879) explained that the liquid jet in this regime undergoes a capillary instability. Based on his analysis, the liquid column is disturbed by an axisymmetric perturbation with a wavelength greater than the jet's circumference. The amplitude of the perturbation increases until becomes equal to the jet radius, at which point, the jet breaks up, and a drop, whose diameter is equal to that of the jet, detaches from it. In this region, the

velocity of the jet with respect to the quiescent air remains small and as the velocity increases, the breakup length increases almost linearly. The jets within this region are commonly referred to as capillary jets as they are primarily influenced by surface tension.

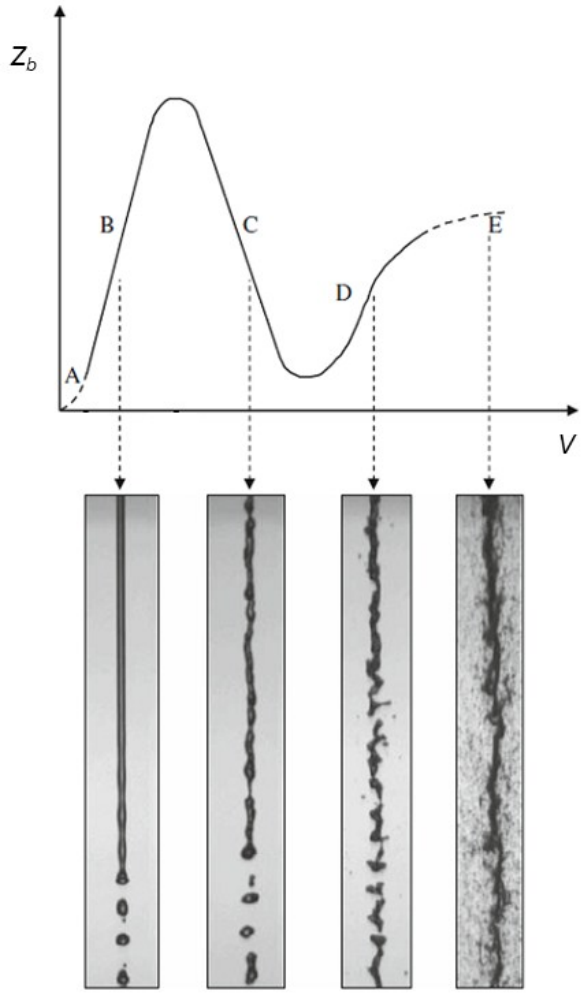

Figure 1.1: Stability curve of a circular jet for different Reynolds numbers, (B) *Re*=400, *QWe*=0.03, (C) *Re*=2250, *QWe*=1.35, (D) *Re*=8000, *QWe*=24, (E) *Re*=14000, *QWe*=35 (From Dumouchel 2008).

As the jet velocity increases, the jet length reaches a maximum that indicates the beginning of the first wind-induced regime (region C, figure 1.1). Weber (1931) demonstrated analytically that in this regime, the gas resistance produces an irregular weaving of the jet which increases in magnitude with jet velocity and results in a decrease of the jet length. The perturbation evolving

on the jet interface is antisymmetric (sinuous) and the drop production is not as organized as in the Rayleigh regime. In addition, the size of the formed droplets is slightly smaller than that of the Rayleigh regime.

In the second wind-induced regime (region D, figure 1.1), the inertia of the fluid overcomes the effect of the surrounding gas resistance and the jet length again increases with increasing velocity. In this regime, the liquid flow turbulence assists the aerodynamic forces toward increasing the growth rate of perturbations. In a very chaotic shape, the liquid jet column is perturbed right at the nozzle exit and small droplets are detached from its surface. Farther downstream, the remaining liquid flow breaks up into large liquid fragments; these eventually undergo a secondary breakup (Dumouchel 2008).

Disintegration regime	**Weber number Criteria**
Dripping	$We<4$
Rayleigh	$We>4$, $QWe<0.6+2.5Oh^{0.9}$
First wind-induced	$0.6+2.5Oh^{0.9}< QWe <6.5$
Second wind-induced	$6.5< QWe <20.15$
Atomization (spray)	$QWe>20.15$

Table 1.1: Jet breakup regimes and Weber number criteria (From Dumouchel 2008).

In the atomization regime, as characterized by region E in figure 1.1, immediately at the nozzle exit, deformations appear on the liquid interface. Due to the interaction between the liquid flow and the gas, these deformations grow in space and time and eventually result in the ejection of liquid fragments from the main liquid flow. The atomization regime includes primary breakup and secondary breakup steps. In the primary breakup step, the initial flow is deformed and liquid fragments are produced. Then, in the secondary breakup process, these liquid fragments distort and disintegrate into smaller elements. The fragmentation continues until the surface tension

forces are strong enough to ensure the cohesion of the liquid fragments (Dumouchel 2008). The size of the produced stable droplets is much smaller than the jet diameter. Within this regime, the spray properties including the condition for the onset of breakup are a strong function of the degree of flow development and the presence of turbulence. Chigier & Reitz (1996) emphasized the importance of liquid cavitation in the atomization regime: cavitating flows produce small breakup length jets whereas fully detached flows produce high breakup length jets.

The first wind-induced regime is reached when the surrounding gas inertia force reaches around a tenth of the surface tension force; these two forces become of the same order of magnitude as the second wind-induced regime is approached. Lin & Creighton (1990) calculated the energy budget of a disintegrating liquid jet based on a spatial linear stability theory. This budget revealed that in the Rayleigh and the first wind-induced regimes, capillary pinching remains the governing mechanism of jet breakup and the term associated to surface tension is always dominant. However, the second wind-induced and atomization regimes are strongly wind-induced and surface tension acts against the formation of small droplets generated by the interfacial pressure fluctuations. At low jet velocities, the growth of the long-wavelength small-amplitude disturbances on the interface, promoted by the interaction between the liquid and ambient gas, initiates the liquid breakup process. For high-speed liquid jets, the breakup is thought to result from the unstable growth of short wavelength waves created form the aerodynamic forces and turbulence effects (Reitz & Bracco, 1982).

The breakup of a liquid jet entering into another fluid has been quantitatively studied for more than 130 years. Plateau (1873) reported that for a given jet volume, the surface energy associated with a uniform circular cylindrical shape is not the minimum attainable. He mentioned that the jet tends to disintegrate into segments with a length equal to 2π times of the jet radius,

such that if a spherical drop is formed from each segment, the droplets have the minimum surface energy. Rayleigh (1879) argued that the breakup of a liquid jet is the consequence of hydrodynamic instability and showed that a circular cylindrical liquid jet is unstable with respect to disturbances of wavelengths larger than its circumference. Among all unstable disturbances, the maximum growth rate belongs to disturbances with wavelengths around 1.5 times of the jet circumference. Considering that one single drop is produced per wavelength, and applying the mass conservation law at the breakup, he reported a drop diameter of 1.89 times of the jet diameter.

To simplify the analysis, Rayleigh neglected the effects of the surrounding gas, liquid viscosity, and gravity. However, his theory provides a stability criterion for laminar liquid jets based upon a linear temporal analysis which remains as the fundamental basis of liquid jet instability studies. In Rayleigh's analysis it is assumed that the interface of a jet column of radius R is perturbed by an axisymmetric wave with a Fourier component of,

$$\eta(z,t) = \eta_0 e^{i(\alpha t - kz)} \tag{1.1}$$

in the cylindrical coordinate system (r, z). This wave follows the liquid whose origin $z = 0$ is at the nozzle exit at time $t = 0$. η is the displacement of the interface from the undisturbed position $r = R$, η_0 represents the initial amplitude of the perturbation, and k indicates the wavenumber of the disturbance in the z direction. α is a complex number as $\alpha = \alpha_r + i\alpha_i$, where its real part α_r is frequency and its imaginary part α_i represents the temporal growth rate of the perturbation. The combination of the continuity and momentum equations along with the kinematic and dynamic conditions that have to be satisfied at the liquid–gas interface leads to a dispersion equation. The dispersion equation, which gives the growth rate α_i for a given perturbation wavenumber k, shows that for a given wavenumber, the growth rate reaches a maximum α_{imax}. This dominant

perturbation is supposed to be responsible for the jet breakup when its amplitude is equal to the jet radius. This breakup criterion is written as,

$$R = \eta_0 e^{-\alpha_{i\max} t_b} \tag{1.2}$$

in which t_b is the breakup time. Multiplying the breakup time by the jet velocity, V, results in the breakup length Z_b as,

$$Z_b = -\frac{V}{\alpha_{i\max}} \ln \frac{R}{\eta_0}. \tag{1.3}$$

Equation (1.3) shows that the jet breakup length varies linearly with the liquid jet velocity as observed in region B of the stability curve (See figure 1.1).

Although Rayleigh later expanded his theory to include the influence of viscosity (1892), the analysis became excessively complicated and failed to yield any applicable results. Weber (1931) extended the Rayleigh theory by taking into account the liquid viscosity, the jet velocity and the surrounding gas effects. Using a quasi-one-dimensional analysis, he found that by increasing the liquid jet velocity, the aerodynamic forces increase the growth rate of the dominant wave and subsequently the breakup length decreases (region C of the jet stability curve). In addition, by increasing the jet velocity, the dominant wavelength decreases which leads to a reduction of the droplets size. Weber also showed that the viscosity tends to reduce the breakup rate and increase the drop size.

Taylor's analysis (1962) revealed that the density of the surrounding gas has a fundamental effect on the jet breakup regime. When the gas inertia force (which is proportional to the gas density) is sufficiently larger than the capillary force, at the gas-liquid interface, droplets are created with diameters that are much less than the jet diameter. This regime is referred to as the Taylor mode or the atomization mode which leads to fine spray formation.

As a result of the assumption that the perturbation magnitude remains small relative to the diameter of the jet, linear analyses fail near the point of jet breakup. Therefore, linear methods do not result in a prediction of the droplet sizes nor can they accurately forecast the production of satellite droplets (i.e. small droplets that formed from liquid threads between the main drops). Despite these shortcomings, the linear stability analysis provides a qualitative description of the physical mechanisms involved in the various regimes of the jet breakup process. The physical mechanism of breakup frequently remains the same during nonlinear evolution. However, the nonlinear evolution subsequent to the onset of breakup alters these physical mechanisms quantitatively only. The nonlinear instability for a circular liquid jet in the Rayleigh breakup regime has been studied extensively, through perturbation expansion (Nayfeh 1970, Lafrance 1975, Chaudhary & Redekopp 1980), quasi-one-dimensional approximation (Bogy 1979a, 1979b), and numerical simulation (Ashgriz & Mashayek 1995). Some nonlinear results showed that the growth rate is slightly less than the linear prediction and also the cut-off wavenumber; i.e. wavenumber below which jet is unstable, depends on the amplitude of perturbation. Bogy (1979c) attested that the perturbation solutions are capable of describing the process of liquid jet breakup, and a nonlinear analysis up to the third order of perturbation expansion in terms of the initial disturbance amplitude is generally sufficient to account for the inherent nonlinear nature of the breakup process.

The temporal stability analysis presents the growth of disturbances in time whereas, the spatial stability analysis considers the growth of perturbation in space. In conclusion, the wavenumber k in equation (1.3) is a complex number which its imaginary part k_i represents the spatial growth rate of the perturbation. Keller et al. (1973) argued that the disturbances initiating at the nozzle face actually grow in space and move downstream to break up the jet into drops.

They found that the spatial growth rate k_i is deduced from the temporal growth rate, α_i by the relation $k_i = \alpha_i + O(1/We)$. They also suggested that temporal and spatial analyses converge when $We > 3$.

Leib & Goldstein (1986a, b) demonstrated the existence of unstable absolute disturbances that propagate in both the downstream and upstream directions. These instabilities differ from the convective instabilities that are characterized by a downstream propagation only. Leib & Goldstein (1986a) found that an inviscid jet issuing in vacuum is subject to an absolute instability if $We < \pi$, otherwise the instability is convective. This cut-off value is slightly changed by taking into account the effects of the liquid viscosity and the gas density (Leib & Goldstein 1986b). According to Lin & Reitz (1998), absolute instability occurs when the inertia is not sufficiently large to carry downstream all the unstable disturbances that derive their energy from the surface tension. Thus, surface tension remains the source of instability and transition from absolute to convective instability corresponds to the beginning of the formability of the liquid jet. The theoretical delineation between absolute and convective instabilities is similar to the criterion for the dripping regime (Dumouchel 2008).

The three-dimensional equations describing the nonlinear motion of symmetric and asymmetric free-surface flow will be complicated if analytical solutions are to be obtained. Therefore generating simplified equations that still capture the essential physics of the problem is very helpful. This is possible when the liquid column is long and thin, so that the fluid flow is directed mostly along the axis and the velocity field is one-dimensional. Particularly, this slenderness assumption is valid close to breakup and converges asymptotically to its exact value close to pinch-off (Eggers & Duppont 1994).

In a pioneering work, Lee (1974) derived a nonlinear one-dimensional set of equations for inviscid, incompressible fluids using certain ad hoc assumptions regarding velocity and pressure variations across the jet. Lee's linearized equations agree with the inviscid form of Weber's equations. Using the basic theory of one-dimensional Cosserat continuum, Green (1976) presented a nonlinear quasi-one-dimensional theory for a straight, circular, viscous jet. These derivations are conceptually entirely different from the approach of Weber (1931) or Lee (1974). Rather than starting with a three-dimensional theory based on the Navier-Stokes and continuity equations, Green (1976) starts at the outset with a one-dimensional continuum model, called a Cosserat continuum that has a structure provided by deformable vectors. Using the theory of directed (or Cosserat) curve and consequently a one-dimensional continuum model, the jet motion becomes a function of time and axial distance only, thus simplifying the problem considerably.

Consider a surface embedded in a Euclidean 3-space to every point of which a vector, called a director, is assigned. Such a surface with deformable directors is called a Cosserat surface. Based on the idea of using directors in continuum mechanics and considering a body as a collection of points together with directions associated with the points, E. & F. Cosserat (1909) developed a theory for oriented medium called the Cosserat theory. The Cosserats recognized the significance of the idea of oriented bodies in one and two dimensions in the development of theories of rods and shells. The application of such a direct approach to elastic rods has received more attention than fluid jets. Green & Laws (1966) developed a Cosserat one-dimensional theory for analysis of rod-like bodies. In their model, the continuum is an oriented space curve corresponding to the rod axis with two deformable directors (representing the cross-section of the rod) attached to every point of the curve. Green (1976) presented a nonlinear quasi-one-

dimensional model for a straight, circular, viscous jet using the basic theory of a one-dimensional Cosserat continuum model. He started with the continuum model, which is based on postulated integral balance laws in one dimension, then used the principles of continuum physics such as invariance requirements and constitutive assumptions to derive the one-dimensional equations and appropriate boundary conditions. The results are valid for a straight jet of any incompressible material (solid and fluid). Finally, fluidity was accounted for and appropriate constitutive equations for a Newtonian viscous fluid were obtained.

The theory of directed (or Cosserat) curve is based on a general thermodynamic theory, which can be used for any kind of material, solid or fluid. This quasi-one-dimensional model which inherently contains the radial inertia effects in its equations, yields the jet profile as a function of the axial coordinate only, and simplifies the analysis considerably. The Cosserat equations of Green (1976) were successfully used by Bogy to study the instability of circular liquid jets in linear (1978a, 1978b), nonlinear (1979a, 1979b), and numerical analyses (1980). However, such a theory evidently cannot predict all the features of the original three-dimensional problem and is only able to specify its main characteristics. For example, according to Bogy (1979c), one limitation of this model is its inability to account for any axial velocity-profile effects. The axial jet velocity is assumed to be a function of the axial distance only and not the radial distance, meaning that only plug flow is considered.

Bechtel et al. (1992), Eggers & Dupont (1994), and Garcia & Castellanos (1994) used a perturbation approach to derive one-dimensional equations from Navier-Stokes equations. However, some differences appear among their resulted leading terms at higher orders. Asymptotically, the leading-order versions of this procedure for a slender jet result the Cosserat equations. Garcia & Castellanos (1994) substituted a truncated Taylor series in the radial

coordinate into the Navier–Stokes equations and boundary conditions at the interface and developed equations for parabolic velocity profiles. While the Cosserat equations of a circular jet were derived, their model allows the Cosserat equations to be applied for liquid jets emerging from long circular nozzles.

1.2 Planar liquid sheets

Most of the atomization systems rely on a large liquid surface-to-volume ratio to increase the rate of disintegration. Thin sheets of injected liquid are a very common mechanism for increasing the interface area. The most popular type of nozzle that produces flat liquid sheets is the fan nozzle. The orifice of a fan nozzle is formed by the intersection of a V groove with a hemispheric cavity communicating with an inlet cylindrical liquid. Flat liquid sheets are also produced by impinging two circular cylindrical jets. This way, the shape of the sheet is changed by varying the impingement angle as formed by the two jet axes (See figure 1.2). If this angle is equal to 180°, the liquid sheet is radial (figure 1.2a). It is important to note that the thickness of the liquid sheets produced by a fan nozzle or by the impingement of two jets is decreasing in the streamwise direction; the property which plays an important role in disintegration of the liquid stream into a spray (Dumouchel 2008).

Three modes of sheet disintegration were identified which are referred to as rim, wave, and perforated-sheet disintegration. In practice, all three disintegration modes exist in an atomizer and their relative importance govern the mean drop size and the drop size distribution. In the rim mode as the sheet develops downstream, due to the capillary force, the free edge of a liquid sheet contracts into a thick rim. The contraction lasts until the edges of the sheet coalesce and drops are emitted from the edges by a mechanism similar to the disintegration of a circular liquid jet. In

this mode, large drops, as well as numerous small satellite droplets are produced. Rim disintegration mode occurs mainly where both the surface tension and the viscosity of the liquid are high (Sirignano & Mehring 2000).

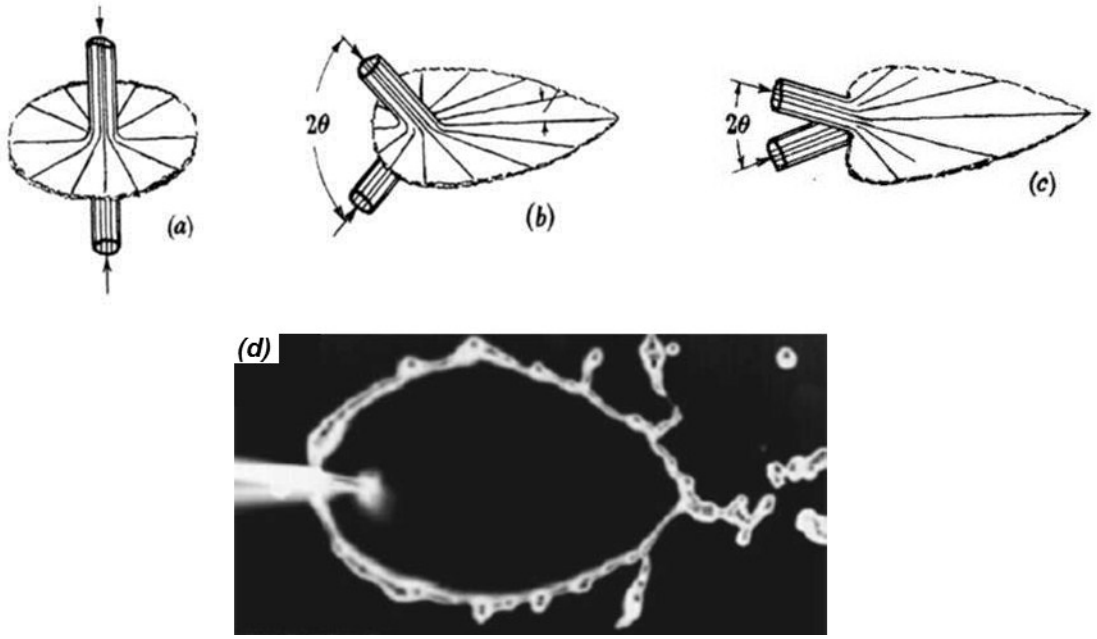

Figure 1.2: Sheets formed by the impact of two circular cylindrical jets (Sketches from Taylor 1960, image from Li & Ashgriz 2006).

At higher injection pressures, a large wavelength sinuous wave grows due to the Kelvin-Helmholtz instability and the sheet is eventually torn away before the two edges coalesce (figure 1.3). This kind of disintegration is referred to as wave disintegration. At sub-atmospheric pressure, perforation holes appear on the sheet; they consequently grow in size and produce ligaments of irregular shapes. The whole sheet is thus disintegrated into drops of varying sizes. This mode is known as the perforated-sheet disintegration (Sirignano & Mehring 2000).

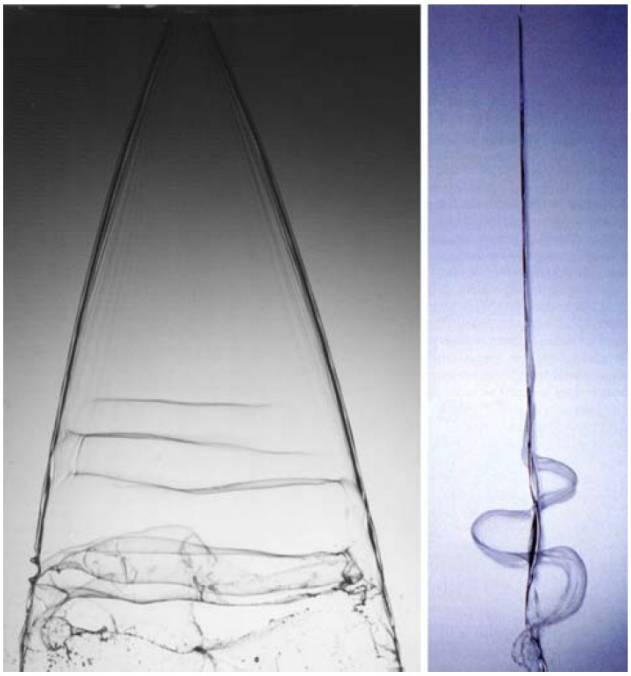

Figure 1.3: Sinuous mode of disintegration of a fan-nozzle liquid sheet (left front view, right side view, from Dumouchel 2005)

The mechanism of liquid sheet instability and breakup was investigated by Squire (1953) and Hagerty & Shea (1955) for an inviscid liquid sheet of uniform thickness in an inviscid gas medium. Squire (1953) stated that a minimum difference of velocity between the two fluids is required for the Kelvin–Helmholtz instability to develop. Hagerty & Shea (1955) found that only two types of waves are possible on a flat liquid sheet at any given frequency. These two correspond to the two surface waves oscillating exactly in and out of phase, commonly referred to as the sinuous and varicose modes (See figure 1.4). Their results show that the dominant type of disturbance is antisymmetrical (sinuous). The principal sources of sheet instability are the aerodynamic forces arising from the interaction of the sheet with the surrounding gas medium while the surface tension effects always tends to smooth out any perturbances. When the Weber number, which represents the ratio of the aerodynamic to the capillary forces, exceeds a critical

value of unity, sheet becomes unstable and breaks up. The sinuous mode is more unstable than the dilational mode when the gas-to-liquid density ratio is low (Dombrowski & Hooper 1962); conversely, the dilational mode is more unstable than the sinuous mode when the density ratio is high (Rangel & Sirignano 1991).

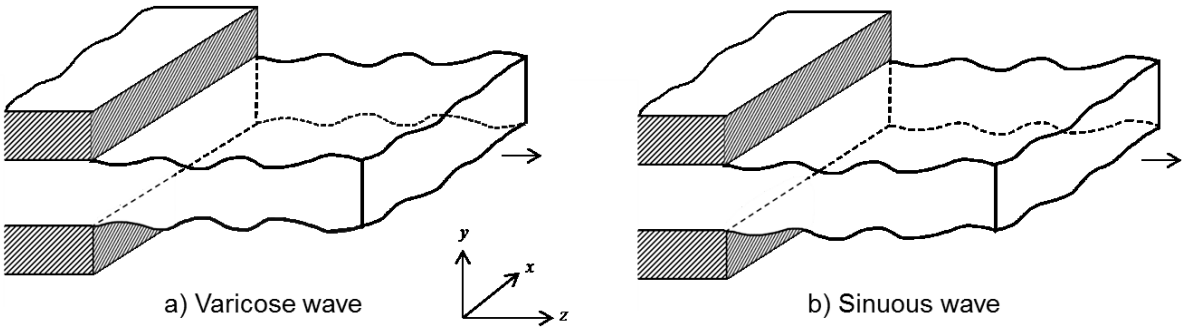

Figure 1.4: Schematic of a a) varicose disturbance and a b) sinuous disturbance.

The effect of liquid viscosity was investigated by Li & Tankin (1991). Their analyses show that liquid viscosity has a dual effect on the stability of liquid sheets. At low Weber numbers, viscosity introduces an additional mode of instability, which can grow even faster than the aerodynamic instability. At high Weber numbers, the aerodynamic forces always enhance the instability while the liquid viscosity always reduces the disturbance growth rates and shifts the dominant disturbances to longer wavelengths.

Based on the linear theory, the growth rate for both sinuous and dilational waves increases as the Weber number is increased. For all density ratios, there exists a region of wavenumbers, in which dilational waves are more unstable than the sinuous ones; the latter might even be stable in that region. For both sinuous and dilational waves, the disturbance wavelength with maximum growth rate decreases as the density ratio is increased (Sirignano and Mehring 2000).

Ibrahim & Akpan (1996) presented a three-dimensional linear analysis of a plane viscous liquid sheet in an inviscid gas medium. Based on their results, at low Weber numbers, two-dimensional disturbances always dominate the instability of symmetric and antisymmetric waves. At high Weber numbers, long-wave three dimensional symmetric disturbances have larger growth rates than their two-dimensional counterparts, while the opposite is true for antisymmetric disturbances. For disturbances with short wavelengths, both two- and three-dimensional disturbances grow at approximately the same rate. It was found that increasing the gas-to-liquid density ratio or decreasing the Ohnesorge number enhances the departure in the growth rates of two- and three-dimensional symmetric disturbances of long wavelength. In contrast to planar sheets in which only dilational waves are dispersive, both sinuous and dilational capillary waves are dispersive in the presence of disturbances parallel and transverse to the main flow direction (Sirignano and Mehring 2000).

In reality, the liquid sheet breakup process is nonlinear. The linear theory fails when the liquid sheet breaks up, because during the growth of the sinuous mode of disturbances predominant under practical conditions, the two gas-liquid interfaces have a constant distance and the sheet breakup cannot occur without variation of the sheet thickness. Nonlinear analysis was performed through a 2^{nd} order analysis by Clark & Dombrowski (1972), through a 3^{rd} order analysis by Jazayeri & Li (2000), and through a nonlinear discrete-vortex method by Rangel & Sirignano (1991). The results predicted the appearance of the first harmonic dilational mode due to the energy transfer occurring from the fundamental sinuous mode, which subsequently leads to the breakup at half-wavelengths of the fundamental sinuous mode. In addition, the nonlinear sinuous growth rates were found to be less than the value predicted by linear theory.

1.3 Elliptic liquid jets

Studies on liquid jets exiting asymmetric nozzles are scarce in literature even though there has been interest in them since the nineteenth century. The reason could be greater mathematical difficulty specifically if analytical methods are used. The interest in the study of non-circular jets arises, from the fact that the jets issued from asymmetric orifices may break up considerably earlier than axisymmetric jets. In fact, previous studies showed that the mechanism of liquid jet breakup is influenced by an unusually large number of parameters, namely, the inlet condition before the emanating, the orifice geometry, and the environmental situation into which the jet is injected. The effect of orifice geometry has been overlooked the most in the literature compared to the effect of the remaining parameters.

Among possible asymmetric shapes, elliptic orifices have been examined more. In effect, it has been shown that elliptic jets outperform circular jets in terms of rapid mixing and spreading when discharging into another fluid (Gutmark & Grinstein 1999). Elliptic orifices have been examined for possible practical applications such as pesticide spraying, spray painting and liquid propellant rocket injectors (McHale et al. 1971).

An interesting phenomenon occurring in elliptic jets is axis-switching. In many instances when a fluid exits an elliptic orifice, the free jet behavior is oscillatory; the elliptic cross-section of the jet transforms into a circular one, then again into an elliptic cross-section but with the major axis perpendicular to that of the elliptic orifice; then circular, then elliptic again with major axis in the original direction, and so on (See figures 1.5 and 1.6). The oscillation of the major axis of the free surface elliptic cross section between the perpendicular directions persists until the jet breaks up. Axis-switching was originally reported by Bidone (1830). Taylor (1960) mentioned

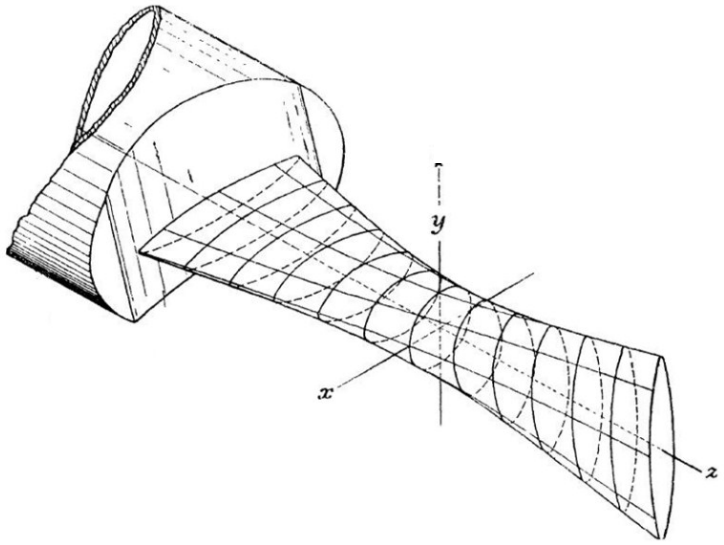

Figure 1.5: Change in the cross-sectional shape of a jet exiting from an elliptic nozzle (From Taylor 1960).

that surface tension causes a periodical transformation, and in the absence of surface tension this transformation occurs only once, after which the cross-section continues to flatten. Oscillations occur due to the competition between the surface tension that tries to restore the cross-section to a circular shape and the inertial force that tries to change the shape of the cross-section to an ellipse.

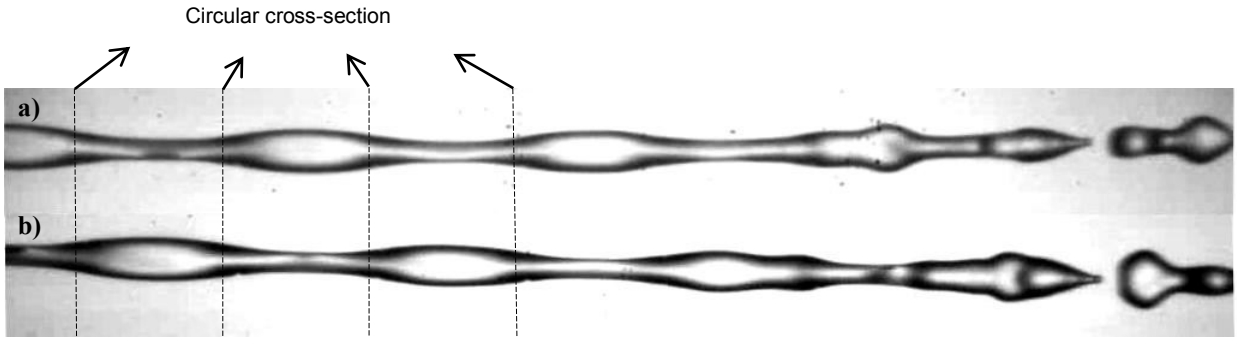

Figure 1.6: Axis-switching of an elliptic jet; a) major axis view, b) minor axis view (From Amini & Dolatabadi 2011c).

An asymmetric nozzle could be a very effective passive control device for enhancing the breakup length. Measurements with elliptic nozzles showed that elliptic jets are quite different from the extensively studied circular and planar jets. Because of the azimuthal curvature variation, the former has a more complicated behavior. In diesel spray applications, the droplet size characteristics have been measured by Yunyi et al. (1998). Results showed that for some experimental conditions, the angle of the elliptic spray is much larger than that of the circular spray while the SMD (Sauter mean diameter) of elliptic sprays is smaller than that of the circular sprays. Messina & Acharya (2006) studied experimentally the velocity field and spreading rate of a liquid spray issued from elliptic nozzles with and without primary air. By active forcing of air stream, they manipulated the mixing and growth of the spray. Their results showed that in comparison with the circular nozzle, the spray issued from the elliptic nozzle provides better mixing in terms of higher mass entrainment and greater jet width.

Kasyap et al. (2009) presented experimental results for the breakup of liquid jets issued from elliptic orifices. They reported visual observations of elliptic jets by the characterization of the axis-switching process. They found that a liquid jet emanating from an elliptic orifice exhibits more unstable behavior or a faster breakup process than a corresponding circular liquid jet in a specific range of flow for which axis switching was observed. Moreover, they found that decreasing the ratio of minor to major axes of the elliptic orifice in some ranges makes the elliptic liquid jet more unstable (See figure 1.7).

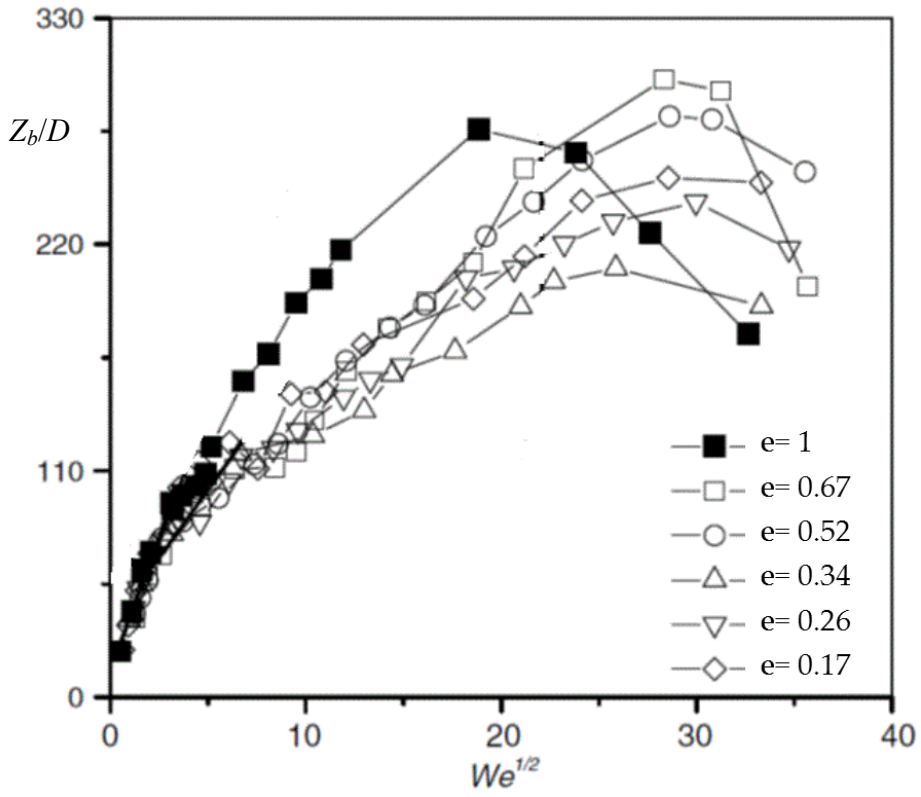

Figure 1.7: Variation of the dimensionless breakup length (Z_b/D) versus $We^{0.5}$ for orifices with different ellipticities. (From Kasyap et al. 2009).

Rayleigh (1890) extended his linear analysis to calculate the dynamic surface tension of liquids by measuring the axis-switching wavelength of inviscid liquid jets with elliptic cross sections. Rayleigh's model was based on the assumption that the departure from circularity of the cross-section of the jet is small. This calculation was further improved by Bohr (1909) by including the viscosity and the gas effects into the nonlinear model for small ellipticities. Geer & Strikwerda (1983) developed asymptotic theories and approximations to model the spatial evolution of the free surface of slender elliptic jets. The issues of instability and drop formation were not addressed in their work.

The instability of an inviscid elliptic liquid jet in an inviscid gas was investigated analytically by Dityakin (1954). Neglecting the gravity effect and considering the gas density, he derived a

temporal dispersion equation for axisymmetric disturbances. Dityakin considered an infinitely long quiescent cylindrical liquid column injected into a gas and modeled its response to a small perturbation to the shape of the circular cross-section. In calculating the surface tension which is the main source of instability, because of the usual complexities encountered in ellipse curvature calculations, he simply used curvature of a circle with the radius of semi-minor axis.

Based on a continuum mechanics approach, called the directed curve theory or Cosserat theory, Green (1977) showed the single axes transformation of an elliptic jet, while neglecting the surface tension and viscosity. Including the surface tension, Caulk & Naghdi (1977, 1979) used one-dimensional Cosserat equations to determine the position of the free surface of a viscous liquid jet with a finite ellipticity. Using the Cosserat theory, the motion of a fluid jet is replaced by the motions of a directed curve, in which the material line is identified along the z-axis and the director pair lies in the *x*-*y* plane. The directors are so restricted that they describe an elliptical cross-section of smoothly varying orientation along the length of the jet; for every z = constant, the directors lie along the major and minor axes of the ellipse. Caulk & Naghdi (1979) used their model to investigate the instability of a special case of circular jet only and did not study the issue of elliptic jet instability.

Using a Galerkin averaging method and integrating the Navier-Stokes equations over the elliptic jet's cross-section, Bechtel et al. (1988) obtained a system of one-dimensional equations for arbitrarily high order. Asymptotically, the leading-order versions of these integro-differential equations for a slender jet result in the Cosserat equations through which axis-switching can be explained. Bechtel et al. (1995) used the predicted axis-switching behavior to measure the dynamic surface tension and the elongational viscosity of fluids. In a subsequent article, Bechtel (1989) studied the effects of viscosity and gravity on oscillations of an elliptic jet. Bechtel's

model considers only the oscillating stable mode and does not lead to any instability or breakup. While accurate calculations of the jet curvature as the main cause of instability are vital for this kind of analysis, his model did not keep the full curvature term in its calculations.

Based on the above reviewed literature, and despite the fact that elliptic orifices have shown promising applications, a systematic study of the jet instability and breakup behavior has not been reported yet. The present work aims at conducting such study and analyzing the fundamental mechanisms governing the instability and breakup of jets issued from elliptic orifices.

1.4 Objectives

In the study of liquid jet breakup, the effects of the nozzle geometry have been overlooked. Interest in the study of asymmetric jets arises, in particular, from the fact that jets issuing from such orifices may break up considerably earlier than symmetric jets. Among possible asymmetric shapes, elliptic orifices are the most important; in effect, elliptic jets can be considered as an intermediate case between two simple configurations, the circular jets and the plane sheets, which have been studied very often. There is a greater mathematical difficulty in studying of asymmetric viscous jets, specifically if analytical solutions are to be obtained. Therefore, simplified equations that still capture the main physics of the flow are a helpful tool. In this work, a combination of theoretical and experimental methods is used to reach the following objectives.

- Developing a 3-D model and deriving the governing equations of inviscid jet motion.
- Developing the directed curve theory to study the motion of viscous elliptic jets.
- Performing a linear temporal and spatial analysis on the jet instability and depiction of the dispersion curves.
- Predicting the instability range and studying the behavior of elliptic jets under various azimuthal modes.
- Extracting the jet profile and predicting the axis-switching and breakup.
- Conducting experimental analysis to validate the theoretical results and investigating the effects of ellipticity and length of nozzles.

1.5 Thesis outline

In chapter 2, the three-dimensional equations of inviscid jets are studied. The temporal dispersion equation is derived to determine the instability range and characterize the behavior of the liquid jet at different azimuthal modes. The effect of jet velocity and gas to liquid density ratio is studied in this chapter. The derivation of the dispersion equations of circular and planar jets, which represent special cases of elliptic jets, is demonstrated as well. Chapter 3 contains results of the quasi-one-dimensional Cosserat theory (or directed curve theory) to describe the motion of viscous free-surface flow. The linear solution is obtained by implementing the perturbation methods. The jet behavior in breakup and the axis-switching process is illustrated. The possibility of growth of asymmetric perturbations is studied too. An introduction to the instability of viscous circular and planar jets is mentioned in this chapter. The details of the mathematical formulas derived in chapters 2 and 3 are included in the appendices.

Chapter 4 covers the experimental analysis that is conducted in the present research. An experimental setup is designed to validate the theoretical results and investigate the nozzle length effects. Instability and breakup under both natural and excited perturbations are studied. Based on the measurements of the breakup length, the disturbance growth rate is calculated and the corresponding results are compared with the predicted values from three-dimensional and quasi-one-dimensional analyses. The main physical features of an elliptic jet including the breakup length and the axis-switching are examined as well. Chapter 5 comprises the summary and conclusions of this work followed by useful suggestions for future studies.

Chapter 2

Instability of Inviscid Elliptic Jets

In this chapter the motion of an inviscid liquid jet issuing from an elliptic orifice into an inviscid gas is studied. The linear evolution of initially small disturbances on the liquid jet which includes the effect of the surrounding gas and liquid surface tension is investigated. Regarding the importance of instability analysis, classical linear analysis of circular and planar jets, as two commonly studied cases, are reviewed first. In continuous, using a perturbation-based approach, a similar analysis is performed to study wave propagation on the surface of an elliptic jet. Stability equations are presented in elliptical cylindrical coordinates and the nontrivial solutions that satisfy the boundary conditions are derived. The dispersion equation of waves on a jet column with elliptic cross-section is derived in terms of the m^{th} order Mathieu functions, where m is the m^{th} azimuthal mode. Growth of symmetric and antisymmetric waves is studied for various jet velocities. Elliptic configuration has two extreme cases; circular jet when the ratio of minor to major axis is unity and plane sheet when this ratio approaches zero. Equations are

approximated for small and large ellipticities and well-known dispersion equations of circular and planar jets are recovered.

2.1 Instability of inviscid circular jets

The response of a liquid jet, issuing from an orifice into a stationary gas, to a small perturbation can be modeled by linear stability theory originally used by Rayleigh (1879). By growing the perturbation, jet breakup occurs when magnitude of the radius of perturbed jet exceeds the radius of the undisturbed jet. In the jet instability theory, the governing equations for mass and momentum conservations are solved subject to boundary conditions at the interface that include a normal stress balance, a tangential stress balance, and a kinematic condition. The normal stress balance considers the balance between the surface stresses on both sides of an interface between two fluids, which includes the pressure jump across the interface due to surface tension. In the tangential stress balance the gas is typically assumed to be inviscid. Kinematic boundary condition states that the velocity component normal to the interface is continuous across the interface. The instability of liquid surface due to perturbations is converted mathematically to the condition of the existence of nontrivial solution of the linear system which ultimately leads to a dispersion relation. Dispersion equation relates the growth rate, α, of an initial perturbation of infinitesimal amplitude to its wavenumber k (or wavelength).

Consider a column of fluid of density, ρ_l, and surface tension, σ, streaming with uniform velocity, V, through a stationary inviscid incompressible medium of density, ρ_g. The column is assumed to be infinite in the axial direction and of radius b. A cylindrical coordinate system (r, θ, z) is considered where the z axis coincide with the axis of the column. A small asymmetric

disturbance with a Fourier component of the following form is imposed on the surface of this initially steady motion,

$$\eta = \eta_0 e^{i(\alpha t - kz + m\theta)}. \tag{2.1}$$

In equation (2.1), η represents the displacement of the surface in the radial direction from its undisturbed position $r = b$, t is time, η_0 is the initial amplitude, $k=2\pi/\lambda$ is the axial wavenumber, λ is the wavelength, and α is the complex frequency. The imaginary part of α is the growth rate of the disturbance. Mode number m is an integer and representing transverse modes of disturbances on a liquid jet, i.e. the azimuthal wavenumber. Figure 2.1 represents schematic of few selected modes. Mode zero (m=0) represents a circular cross-section where radius varies only along the axial direction (See figures 2.1a and 2.2). In this case deformation is called varicose mode. For m=1 (figure 2.1b), the cross-section is nearly circular and the axis of the jet is sinuous. This mode is referred to as sinuous mode. When m becomes large, the development of the m^{th} azimuthal mode leads to m peaks in the circumferential direction (figures 2.1c and 2.1d) and the breakup mechanism of the liquid jet consists of ripping away the small droplets from the surface (Yang 1992).

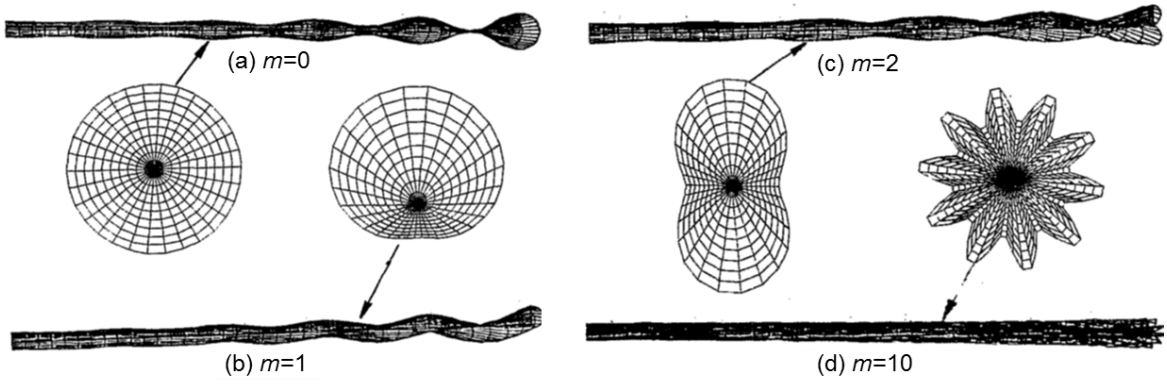

Figure 2.1: Geometrical presentation of azimuthal modes (From Yang, 1992).

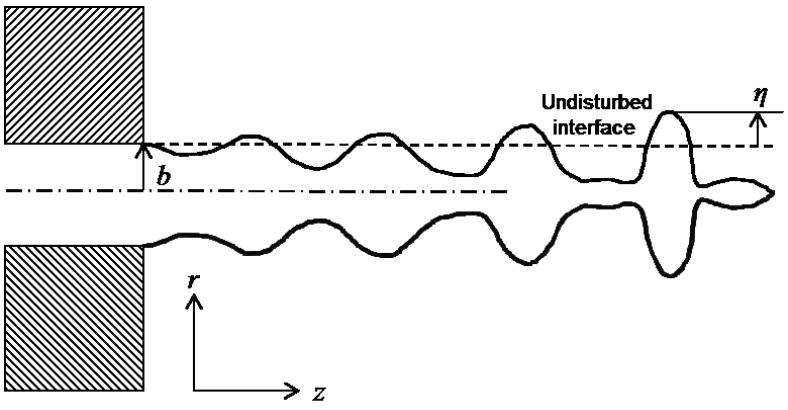

Figure 2.2: Geometrical presentation of axisymmetric disturbances (*m*=0) on a circular jet.

The dependent variables for liquid jet radius, pressure, and velocity component can each be presented as the sum of the value found in the undisturbed state plus the perturbation (denoted by tildas). In particular

$$r = b + \eta, \qquad p = p_0 + \bar{p}, \qquad v = V + \bar{v}. \tag{2.2}$$

Pressure and velocity fluctuations are described by Laplace's equations,

$$\nabla^2 \phi = 0. \tag{2.3}$$

where ϕ is the velocity potential of the disturbance motion. For simplicity the bars are dropped in the following notations. The boundary conditions to be applied at the interface ($r=b+\eta$), which can be taken as $r \approx b$ as an approximation, require that there is no net flux of mass across the interface and that the normal stress is continuous. These boundary conditions are expressed as,

$$u_l = \frac{\partial \eta}{\partial t} + V \frac{\partial \eta}{\partial z}, \quad u_g = \frac{\partial \eta}{\partial t}, \tag{2.4}$$

and

$$p_l - p_g = \sigma \kappa \tag{2.5}$$

where p is the fluctuating pressure in the surrounding medium, σ is surface tension coefficient, and κ is the mean curvature of the surface. The subscripts l and g denote quantities for the liquid and the gas medium, respectively. In addition, u and v are components of fluctuating velocity in r and z directions, respectively. The mean curvature due to disturbance can be obtained linearly as follows,

$$\kappa = -\frac{1}{b^2}(1-m^2-k^2b^2)\eta \ . \tag{2.6}$$

Note that the inertial effects of the surrounding medium enter the analysis only through the fluctuating pressure, p, in boundary condition (2.5). This pressure is found from Bernoulli's equation for liquid phase as,

$$p_l = -\rho_l(\frac{\partial \phi_l}{\partial t} + V\frac{\partial \phi_l}{\partial z}) \tag{2.7}$$

and similarly for gas phase,

$$p_g = -\rho_g(\frac{\partial \phi_g}{\partial t}). \tag{2.8}$$

As it was assumed that fluids are inviscid, the velocity can be expressed in terms of a velocity potential as,

$$u_l = \frac{\partial \phi_l}{\partial r}, \quad u_g = \frac{\partial \phi_g}{\partial r}. \tag{2.9}$$

One can assume that ϕ is in the form of,

$$\phi = f(r)e^{i(\alpha t - kz + m\theta)} \tag{2.10}$$

and seek solutions of equation (2.10) which are free from the singularities at the axis and at infinity. These solutions are,

$$\phi_l = i(\frac{\alpha}{k} - V)\xi\eta_0 e^{i(\alpha t - kz + m\theta)} \tag{2.11}$$

and

$$\phi_g = -i(\frac{\alpha}{k})\zeta\eta_0 e^{i(\alpha t - kz + m\theta)} \tag{2.12}$$

where,

$$\xi = \frac{I_m(kb)}{I'_m(kb)} \tag{2.13}$$

and

$$\zeta = -\frac{K_m(kb)}{K'_m(kb)}. \tag{2.14}$$

I_m and K_m are the m^{th} order modified Bessel functions of the first and second kind, respectively. In addition,

$$I'_m(kb) = \frac{dI_m(kr)}{dr}\Big|_{r=b} \tag{2.15}$$

and

$$K'_m(kb) = \frac{dK_m(kr)}{dr}\Big|_{r=b}. \tag{2.16}$$

Using velocity potential functions (2.11) and (2.12), substituting (2.7) and (2.8) into the normal stress boundary conditions (2.5) yields the nontrivial solution of,

$$\frac{\alpha_i b}{V} = -\frac{\sqrt{(\xi/\zeta)QK^2 + (\xi/\zeta + Q)(1 - m^2 - K^2)/\zeta We}}{(\xi/\zeta) + Q} \tag{2.17}$$

where,

$$Q = \frac{\rho_g}{\rho_l}, \quad K = kb, \quad We = \frac{\rho_l b V^2}{\sigma}. \tag{2.18}$$

Dispersion equation (2.17) was originally derived by Yang (1992). Based on this equation, growth rate of three azimuthal modes are shown in figure 2.3 in which growth rate is nondimensionalized using $\beta = -\alpha_i b/V$.

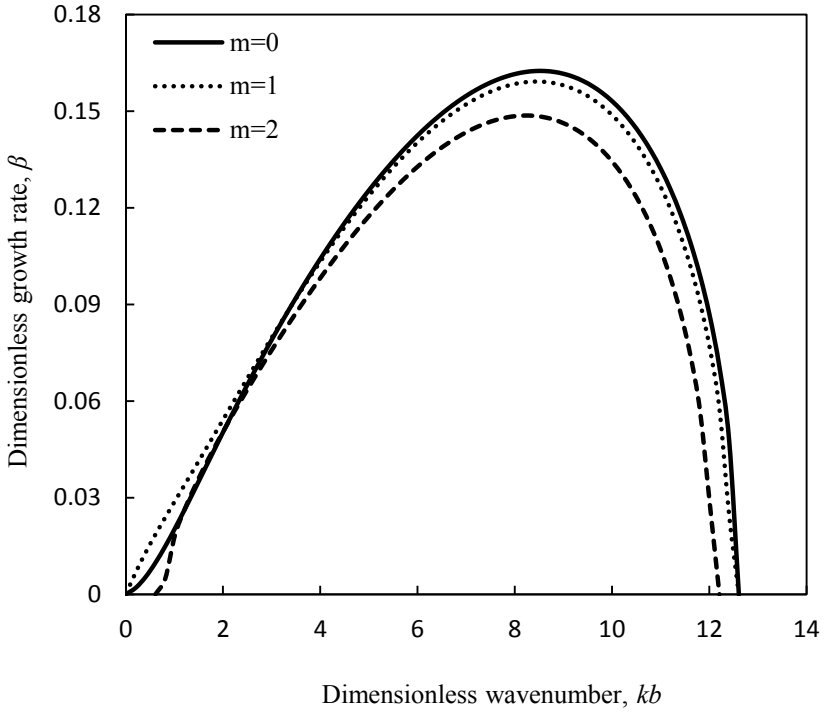

Figure 2.3: Growth rate of symmetric and asymmetric disturbances on a circular jet (Q=0.0013, We=10^4).

Yang (1992) suggested that higher modes (i.e. m=1, 2, 3 …) grow only in higher speeds when aerodynamic effects become significant and in general, axisymmetric modes (m = 0) are always dominant. For long waves (kb << 1) the effect of viscosity is small and the above mentioned inviscid theory can be used. For short waves (kb >> 1) and (m << kb) the viscous axisymmetric theory (Sterling & Sleicher 1975) predicts quite well the behavior of asymmetric disturbances since all modes have the same growth rate. However, for high modes (m >> kb >> 1) the growth rate is lower than the low modes growth rate. The viscous asymmetric theory becomes important only for low Reynolds number (less than a few thousands) and when m >>

kb. In general, no asymmetric disturbances with maximum wave growth rate higher than the axisymmetric one was found (Avital 1995).

For axisymmetric disturbances (m=0) and negligible gas densities ($\rho_g = 0$), equation (2.17) reduces to,

$$\alpha_i \sqrt{\frac{\rho b^3}{\sigma}} = -\sqrt{kb(1-k^2b^2)\frac{I_1(kb)}{I_0(kb)}}, \tag{2.19}$$

a result originally due to Rayleigh. Without the effect of ambient gas, unstable modes are only possible when $kb < 1$, i.e. jet is stable to all non-axisymmetric disturbances but is unstable to axisymmetric ones whose wavelength $\lambda=2\pi/k$ is larger than the circumference of the jet, $2\pi b$.

2.2 Instability of inviscid planar sheets

Consider a two-dimensional, inviscid, incompressible liquid sheet of thickness 2b moving with velocity V through a quiescent, inviscid, incompressible gas medium (See figure 2.4). The liquid and gas have densities of ρ_l and ρ_g, respectively. A spectrum of infinitesimal disturbances of the form,

$$\eta = \eta_0 e^{i(\alpha t - kz)} \tag{2.20}$$

are imposed on the initially steady motion. The instability produces fluctuating velocities and pressures u_l, v_l and p_l for the liquid, and u_g, v_g and p_g for the gas. u and v are velocity components in y and z directions, respectively. In equation (2.20), η_0 is the initial wave amplitude, $k=2\pi/\lambda$ is the axial wavenumber, and $\alpha=\alpha_r+i\alpha_i$ is the complex growth rate. It is desired to obtain a dispersion relation $\alpha=\alpha(k)$ from which the most unstable disturbance can be deduced. To obtain the dispersion relation, the Laplace's equations for the flow inside (liquid) and outside (gas) the sheet are to be solved, i.e.

$$\nabla^2\phi = 0. \tag{2.21}$$

Using a modal analysis, a solution is assumed in the form of,

$$\phi = (C_1 e^{ky} + C_2 e^{-ky}) e^{i(\alpha t - kz)} \tag{2.22}$$

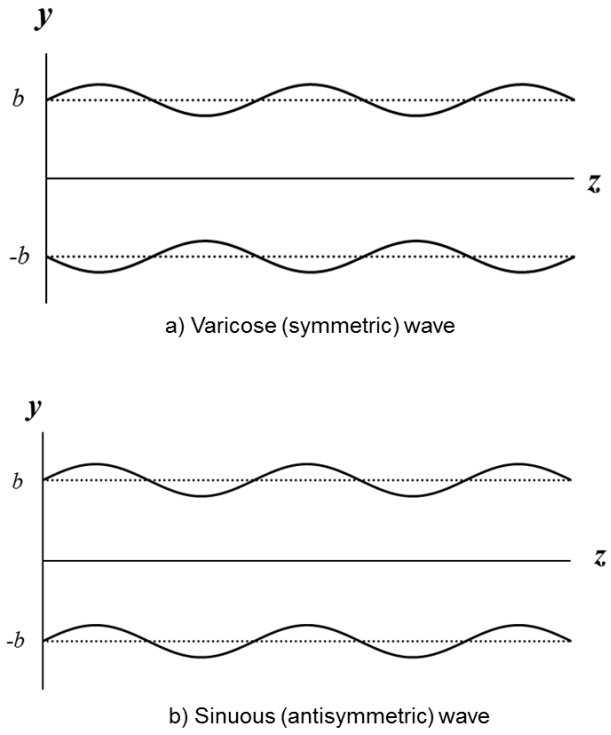

Figure 2.4: Scheme of symmetric and asymmetric waves on a liquid sheet.

with the velocity potential ϕ subject to the following boundary conditions at the interfaces (y = $\pm b$) of the liquid and gas,

$$u_l = \frac{\partial \eta}{\partial t} + V\frac{\partial \eta}{\partial z}, \quad u_g = \frac{\partial \eta}{\partial t} \tag{2.23}$$

and

$$p_l - p_g = \sigma\kappa. \tag{2.24}$$

The subscripts l and g denote quantities for the liquid and the gas medium, respectively. In addition, σ is the surface tension coefficient and κ denotes the local interface curvature given by,

$$\kappa_{\pm} = \mp\sigma \frac{\partial^2 \eta_{\pm}}{\partial z^2} \tag{2.25}$$

where $\pm$ sign denotes the solutions of upper ($y = b$) and lower ($y = -b$) interfaces of the liquid sheet. Note that $\eta = \eta_+ = -\eta_-$ for the symmetric case and $\eta = \eta_+ = \eta_-$ for the antisymmetric case. Equations (2.23) and (2.24) are mathematical statements of the linearized kinematic free surface condition and continuity of normal stress, respectively. Velocity can be described by potential flow theory as,

$$u_l = \frac{\partial \phi_l}{\partial y}, \quad u_g = \frac{\partial \phi_g}{\partial y} \tag{2.26}$$

and the linearized unsteady Bernoulli equation is used within both fluids to find pressure as,

$$p_l = -\rho_l \left(\frac{\partial \phi_l}{\partial t} + V \frac{\partial \phi_l}{\partial z} \right) \tag{2.27}$$

and

$$p_g = -\rho_g \frac{\partial \phi_g}{\partial t}. \tag{2.28}$$

The gas phase boundary conditions require that far from the interface $(y \to \pm\infty)$, the disturbance vanishes, i.e.

$$u_g, \ v_g, \ p_g \to 0 \quad (\phi_g \to \text{constant}). \tag{2.29}$$

The following conditions also should be applied at the sheet centerline, i.e. y=0.

$$\phi_l = 0 \tag{2.30}$$

for sinuous case and,

$$\frac{\partial \phi_l}{\partial y} = 0 \tag{2.31}$$

for varicose case. As determined by Hagerty & Shea (1955), two solutions or modes exist which satisfy equation (2.22) subject to the boundary conditions at the upper and lower interfaces, corresponding to the varicose and sinuous modes. For the varicose (dilational) mode, the waves are π radians out of phase as shown in figure 2.4a. On the other hand, for the sinuous mode, the waves at the upper and lower interfaces are exactly in phase as shown in figure 2.4b.

For the case of varicose waves, solutions for the liquid and gas velocity potential are given by,

$$\phi_l = i(\frac{\alpha}{k} - V)\frac{\cosh(ky)}{\sinh(kb)}\eta_0 e^{i(\alpha t - kz)} \tag{2.32}$$

$$\phi_{g\pm} = -i(\frac{\alpha}{k})e^{\mp k(y\mp b)}\eta_0 e^{i(\alpha t - kz)} \tag{2.33}$$

where $\pm$ sign denotes the solutions for the velocity potential of the semi-infinite streams above and below the fluid sheet. For the sinuous mode, velocity potential functions are as follows.

$$\phi_l = i(\frac{\alpha}{k} - V)\frac{\sinh(ky)}{\cosh(kb)}\eta_0 e^{i(\alpha t - kz)} \tag{2.34}$$

$$\phi_{g\pm} = \mp i(\frac{\alpha}{k})e^{\mp k(y\mp b)}\eta_0 e^{i(\alpha t - kz)}. \tag{2.35}$$

When the velocity and pressure solutions are substituted into the normal stress condition (2.24), the following dispersion relation between α and k is obtained for the case of sinuous waves,

$$\frac{\alpha_i b}{V} = -\frac{\sqrt{\tanh(kb)Qk^2b^2 - (k^3b^3/We)[\tanh(kb)+Q]}}{\tanh(kb)+Q} \tag{2.36}$$

and for the case of varicose modes,

$$\frac{\alpha_i b}{V} = -\frac{\sqrt{\coth(kb)Qk^2b^2 - (k^3b^3/We)[\coth(kb)+Q]}}{\coth(kb)+Q}. \tag{2.37}$$

Q denotes the density ratio between gas and liquid, ρ_g / ρ_l, and Weber number is defined as $We = \rho_l b V^2 / \sigma$. Dispersion equations (2.36) and (2.37) were originally derived by Hagerty & Shea (1955).

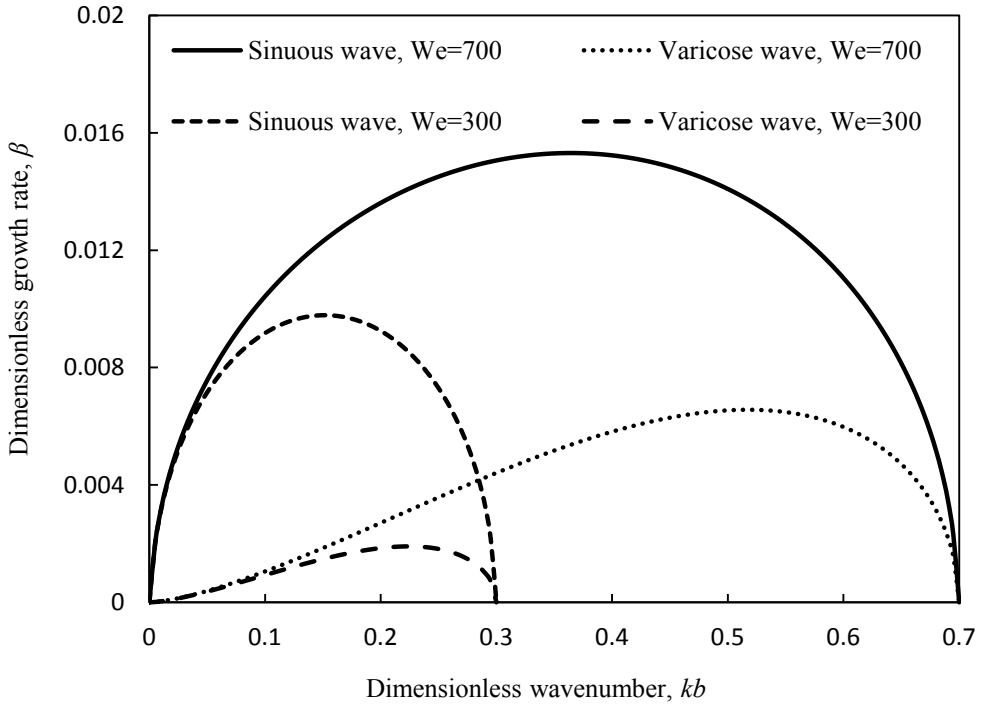

Figure 2.5: Dimensionless growth rate of an inviscid liquid sheet versus dimensionless wavenumber for a density ratio of *Q*=0.0013 and Weber numbers of *We*=300 and 700.

For Weber numbers of *We*=300 and 700, equations (2.36) and (2.37) for the sinuous and varicose growth rates are plotted in figure 2.5. Growth rate is nondimensionalized by $\beta = -\alpha_i b / V$. It is clear that for the selected *We* case, the growth of sinuous waves dominate the growth of varicose waves. While long waves have been seen to grow on the surfaces of low velocity sheets, it is possible that short waves grow at higher velocities or higher Weber numbers. The identification of long and short wavelength regimes for liquid sheet breakup is similar to the first and second wind-induced regimes for circular jet breakup (Reitz & Bracco

1986, Senecal et al. 1999). However, while the gas inertia assists the surface tension force in the destabilization process for circular jets (in the first wind-induced regime), surface tension is stabilizing for sheets. This is apparent if Q is set to zero in either equation (2.36) or (2.37) so that only surface tension is acting on the sheet. Thus, for a sheet the breakup length decreases continuously as the Weber number is increased (See figure 2.5) while the destabilizing effect of surface tension on a circular jet causes the breakup length to grow from zero to a maximum and then decrease again as We is increased (See figure 1.1).

In the limit of $kb >> 1$ and $Q << 1$, dispersion equations (2.36) and (2.37) reduce to,

$$\frac{\alpha_i b}{V} = -\sqrt{Qk^2b^2 - k^3b^3/We}. \tag{2.38}$$

Equation (2.38) is essentially the Kelvin-Helmholtz relation and can also be derived from dispersion equation (2.17) associated to a circular jet in the range of $kb >> 1$ (b is the jet radius), i.e. in the limit that the jet radius is much larger than the disturbance wavelength (Levich 1962). On the other hand, based on the classical results, short waves begin to dominate for sheets if $\lambda/b < 2\pi$, i.e., if the wavelength is less than about six times the sheet half-thickness. It can be suggested that short waves are independent of the nature of the surface on which they grow in which case the curvature of the surface has no effect on the instability (Senecal et al. 1999).

By comparing instability analysis of circular jets and planar sheets, it can be found that behavior of circular and planar jets are different from each other. In circular jets, without the effect of the ambient gas, the jet is stable to all asymmetric disturbances, but is stable to axisymmetric waves whose wavelength is greater than the circumference of the jet. Under higher speed conditions, however, the growth of disturbances on the jet surface is asymmetric. In planar sheet, without the effect of the ambient gas the jet is always stable. In the presence of

surrounding gas the dominant mode is sinuous (asymmetric) and when density ratio becomes significant, varicose mode (symmetric) becomes dominant. In low speed regimes, source of instability for circular jets is capillary and aerodynamic forces, while for liquid sheet is aerodynamic force only. In fact capillary force induces instability for circular jets but opposes the instability for liquid sheets.

2.3 Instability of inviscid elliptic jets

Consider an inviscid liquid jet of density ρ_l and surface tension σ streaming with a uniform velocity V through a stationary, inviscid, and incompressible gas with density of ρ_g. The jet is issuing from an elliptic nozzle with semi-major and semi-minor axes of a and b, respectively. This geometry can be analyzed in elliptical cylindrical coordinates (ρ, θ, z) which represents, the radial, azimuthal, and axial directions, respectively. The elliptical coordinate system is shown in figure 2.6.

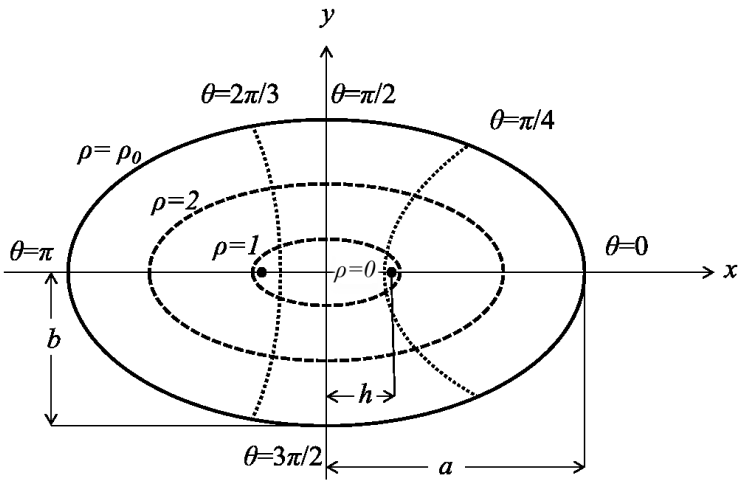

Figure 2.6: Elliptical coordinates system.

Range of these coordinates are $0 \le \rho, z < \infty$ and $0 \le \theta \le 2\pi$. The axis of the jet is aligned with the z axis. ρ equal to constant curves comprise a family of confocal ellipses and θ equal to

constant curves are the orthogonal hyperbolas. We note that the two extreme cases representing a planar jet ($\rho \to 0$) and a circular jet ($\rho \to \infty$). The transformation from Cartesian to elliptical coordinate is given by,

$$\begin{aligned} x &= h \cdot \cosh\rho \cdot \cos\theta \\ y &= h \cdot \sinh\rho \cdot \sin\theta \\ z &= z \end{aligned} \tag{2.39}$$

where h is the distance of the foci to the origin. Furthermore, the following geometric relationships will be used in our analysis,

$$e = \frac{b}{a}, \quad h = b\frac{\sqrt{1-e^2}}{e}, \quad \rho_0 = \tanh^{-1} e \tag{2.40}$$

where e is aspect ratio and the unperturbed jet surface is given by $\rho=\rho_0$. The linear field equation for the inviscid flow inside and outside the jet is given by Laplace's equation, which in the elliptical coordinate is given by,

$$\frac{\partial^2\phi}{\partial\rho^2} + \frac{\partial^2\phi}{\partial\theta^2} + h^2(\sinh^2\rho + \sin^2\theta)\frac{\partial^2\phi}{\partial z^2} = 0 \tag{2.41}$$

where ϕ is the velocity potential. A solution for ϕ is sought in the following form,

$$\phi(\rho,\theta,z) = \mathrm{P}(\rho)\cdot\Theta(\theta)e^{i(\alpha t - kz)} \tag{2.42}$$

where α is the complex wave frequency and k is the axial wavenumber. P and Θ must satisfy,

$$\Theta'' + \Theta(\lambda + 2q\cos 2\theta) = 0 \tag{2.43}$$

and

$$\mathrm{P}'' - \mathrm{P}(\lambda + 2q\cosh 2\rho) = 0 \tag{2.44}$$

where

$$q = \frac{1}{4}k^2h^2 \tag{2.45}$$

and λ is the separation constant. Equations (2.43) and (2.44) are known as Mathieu and the modified Mathieu equation with parameter $-q$, respectively. Details of the evolution of the Mathieu and modified functions can be found in McLachlan (1964). The solutions of Θ and P take the forms of,

$$\Theta(\theta) = D_1 ce_m(\theta,-q) + D_2 fe_m(\theta,-q) \tag{2.46}$$

and

$$\mathrm{P}(\rho) = D_3 Ce_m(\rho,-q) + D_4 Fek_m(\rho,-q). \tag{2.47}$$

In the above equations, ce_m and fe_m are the m^{th} order Mathieu functions of the first and second kinds, respectively and also Ce_m and Fek_m are the m^{th} order modified Mathieu functions of the first and second kinds, respectively. D_1, D_2, D_3, and D_4 are unspecified constants. Only certain combinations of these functions satisfy the physical boundary conditions. Since solutions must be periodic and f_{em} is not a periodic function, Θ takes the following form,

$$\Theta(\theta) = D_1 ce_m(\theta,-q) \tag{2.48}$$

which yields,

$$\phi = [C_1 Ce_m(\rho,-q) + C_2 Fek_m(\rho,-q)]ce_m(\theta,-q)e^{i(\alpha t - kz)} \tag{2.49}$$

where C_1 and C_2 are unspecified coefficients. To solve Laplace's equation, appropriate boundary conditions and interface conditions have to be prescribed. Far from the interface, i.e. in the surround gas as $\rho \to \infty$, the disturbances must vanish. For even disturbances about major axis, the boundary condition may be written as,

$$\frac{\partial}{\partial \rho}\phi(0,\theta,z) = 0. \tag{2.50}$$

This condition leads to the following forms of solution,

$$\phi_l = C_1 Ce_m(\rho,-q)ce_m(\theta,-q)e^{i(\alpha t-kz)}$$
$$\phi_g = C_2 Fek_m(\rho,-q)ce_m(\theta,-q)e^{i(\alpha t-kz)} \tag{2.51}$$

where the subscripts l and g denote quantities for the liquid and the gas medium, respectively. For symmetric disturbances about major and minor axes m is even and for symmetric disturbances only about major axis and antisymmetric about minor axis m is odd. Similar to the notation of Crighton (1973), symmetric modes about major axis are called (C, F) modes.

Another possibility is when disturbances are antisymmetric (odd) about major axis. In this case the boundary condition may be written as,

$$\phi(0,\theta,z) = 0 \tag{2.52}$$

and the solutions of the potential function are in the form of,

$$\phi_l = C_1 Se_m(\rho,-q)se_m(\theta,-q)e^{i(\alpha t-kz)}$$
$$\phi_g = C_2 Gek_m(\rho,-q)se_m(\theta,-q)e^{i(\alpha t-kz)}. \tag{2.53}$$

In this case m is even when disturbances are antisymmetric about the major and minor axes and m is odd when disturbances are antisymmetric about the major axis and symmetric about the minor axis. This case is referred to as the (S, G) mode (Crighton 1973). se_{m} is another form of the Mathieu function of the first kind and also Se_m and Ge_m are other alternative forms of m^{th} order modified Mathieu functions of the first and second kinds, respectively. Readers are referred to Appendix A for definition of above mentioned Mathieu functions.

Upon an initially steady motion, an arbitrary infinitesimal disturbance is imposed which its Fourier component has the following form,

$$\eta = \eta_0 e^{i(\alpha t - kz)} \tag{2.54}$$

where η represents the displacement of the surface in the radial direction from its undisturbed state, i.e. $\rho = \rho_0$, t is time, η_0 is the initial amplitude, k is the axial wavenumber, and α is the complex frequency. The imaginary part of α is the growth rate of the disturbance. While accounting 3-D characteristic of the jet, η_0 is a function of azimuthal angle, θ.

The boundary conditions to be applied at the surface require that there is no net flux of mass across the interface, i.e,

$$u_{\eta,l} = \frac{d\eta}{dt} = \frac{\partial \eta}{\partial t} + V\frac{\partial \eta}{\partial z} \tag{2.55}$$

where $u_{\eta,l}$ is the radial component of interface velocity in the liquid phase and similarly for the gas phase,

$$u_{\eta,g} = \frac{\partial \eta}{\partial t}. \tag{2.56}$$

Since the fluids have been assumed inviscid, the velocity can be expressed in terms of velocity potential which in elliptical coordinate yields,

$$u_\eta = \frac{1}{h\sqrt{\sinh^2\rho + \sin^2\theta}}\frac{\partial \phi}{\partial \rho}. \tag{2.57}$$

Replacing equation (2.57) into equations (2.55) and (2.56) leads to the following set of equations for liquid and gas,

$$i(\alpha - kV)h\eta_0\sqrt{\sinh^2\rho + \sin^2\theta} = C_1 ce_m(\theta,-q)Ce'_m(\rho_0,-q) \tag{2.58}$$

and

$$i\alpha h\eta_0\sqrt{\sinh^2\rho + \sin^2\theta} = C_2 ce_m(\theta,-q)Fek'_m(\rho_0,-q) \tag{2.59}$$

where the primes denote differentiations with respect to ρ which is calculated at $\rho = \rho_0$. Equations (2.58) and (2.59) can be combined to yield a condition for the velocity potentials at the interface,

$$C_1[\alpha Ce'_m(\rho_0,-q)] - C_2[(\alpha - kV)Fek'_m(\rho_0,-q)] = 0. \tag{2.60}$$

Antisymmetric waves follow the same process as above and a similar result may be obtained for the (*S*, *G*) mode.

Another boundary condition is the force balance along the normal direction at the liquid-gas interface, given by,

$$p_l - p_g = \sigma\kappa \tag{2.61}$$

where p_l and p_g are the fluctuating pressure in the liquid and the surrounding gas, respectively. σ is the surface tension coefficient and κ denotes the local interface curvature. For the inviscid case, unsteady Bernoulli equation is used to calculate the pressure fluctuations at interface for both of the liquid and gas as,

$$\begin{aligned} p_l &= -\rho_l\left(\frac{\partial \phi_l}{\partial t} + V\frac{\partial \phi_l}{\partial z}\right), \\ p_g &= -\rho_g\left(\frac{\partial \phi_g}{\partial t}\right). \end{aligned} \tag{2.62}$$

Mean curvature, κ, is (Caulk & Naghdi 1979, Bechtel 1988, Jones & Narayanan 2002),

$$\begin{aligned} &\kappa = [(\phi_1\phi_{2z}\sin^2\theta + \phi_2\phi_{1z}\cos^2\theta)^2 + \phi_1^2\sin^2\theta + \phi_2^2\cos^2\theta]^{-1.5} \times \\ &[(\phi_1^2\sin^2\theta + \phi_2^2\cos^2\theta)(\phi_{1zz}\phi_2\cos^2\theta + \phi_{2zz}\phi_1\sin^2\theta) + \\ &2(\phi_1\phi_{2z} - \phi_2\phi_{1z})(\phi_1\phi_{1z} - \phi_2\phi_{2z})\sin^2\theta\cos^2\theta - \phi_1\phi_2(\phi_{1z}^2\cos^2\theta + \phi_{2z}^2\sin^2\theta + 1)] \end{aligned} \tag{2.63}$$

where ϕ_1 and ϕ_2 are semi-major and semi-minor axes, respectively and subscript z represents derivation to z. In the linearized form, this equation is,

$$\kappa = l_1 + l_2\phi_1 + l_3\phi_2 + l_4\phi_{1zz} + l_5\phi_{2zz} \tag{2.64}$$

where coefficients l are functions of R, e, and θ and have been defined in Appendix B. Substituting the equations (2.62) and (2.63) in equation (2.61) results in the following equation,

$$C_1[\rho_l(\alpha - kV)^2 Ce_m(\rho_0,-q) + \frac{\sigma\gamma(\gamma^2 - K^2)}{b^3} Ce'_m(\rho_0,-q)] - C_2[\rho_g\alpha(\alpha - kV)Fek_m(\rho_0,-q)] = 0 \tag{2.65}$$

where γ is given by,

$$\gamma = \frac{e}{(\sin^2\theta + e^2\cos^2\theta)^{0.5}} \tag{2.66}$$

and e is the aspect ratio, i.e. ratio of the minor to major axes.

The nontrivial solution of equations (2.60) and (2.65) exists if the determinant of the coefficients vanishes. This condition gives following dispersion equation which relates the growth rate of an initial disturbance to the wavenumber in dimensionless form as,

$$\frac{\alpha_i b}{V} = -\frac{\sqrt{\frac{\xi}{\zeta}QK^2 + (\frac{\xi}{\zeta} + Q)(\frac{1}{\zeta We})\gamma(\gamma^2 - K^2)}}{\frac{\xi}{\zeta} + Q} \tag{2.67}$$

in which the following parameters have been used,

$$Q = \frac{\rho_g}{\rho_l}, \quad K = kb, \quad q = \frac{K^2(1-e^2)}{4e^2}, \tag{2.68}$$

and Weber number is defined as,

$$We = \frac{\rho_l b V^2}{\sigma}. \tag{2.69}$$

Furthermore, the following parameters have been used,

$$\xi = \frac{Ce_m(\rho_0, -q)}{Ce'_m(\rho_0, -q)} \tag{2.70}$$

which represents the effect of capillary force and similarly,

$$\zeta = -\frac{Fek_m(\rho_0, -q)}{Fek'_m(\rho_0, -q)} \tag{2.71}$$

which represents the effect of the aerodynamic interaction between the surrounding gas and the liquid. For *m=0*, one can regard this mode as analogous to the axisymmetric mode of a circular jet in which they are symmetric about both axes. On the other hand, for odd values of *m*, modes are even about the major axis and odd about the minor axis, representing sideway oscillations in the plane of the major axis.

The above equations (2.58)-(2.71) belong to the (*C*, *F*) mode representing disturbances symmetric to the major axis. With the similar analyses one can derive dispersion equation (2.67) for (*S*, *G*) mode, i.e. disturbances antisymmetric to the major axis. In this case, ξ and ζ are equal to,

$$\xi = \frac{Se_m(\rho_0, -q)}{Se'_m(\rho_0, -q)} \tag{2.72}$$

and

$$\zeta = -\frac{Gek_m(\rho_0, -q)}{Gek'_m(\rho_0, -q)}. \tag{2.73}$$

For *m* odd, these modes are even about the minor axis, odd about the major axis, and thus represent a flapping of the jet column in the plane of the minor axes; on the other hand, for *m*

even, modes are odd about both axes and describe a torsional oscillation of the column. It is important to note that $\xi/\zeta > 0$ for all ranges of parameters.

In equation (2.66), γ is a parameter related to the curvature and can be expressed by the following equation,

$$\gamma = \frac{r}{a} \tag{2.74}$$

where r is the distance between the origin and a point on the circumference with angle of θ, and a is the semi-major axis. Based on equation (2.67), the maximum growth rate which is responsible for jet breakup, occurs when θ=0. In conclusion, γ =1 and a term of 1-K^2 appears in dispersion equation (2.67). This term comes from jet curvature and indicates the capillary instability range. Similarly, in dispersion equation of a circular jet (Rayleigh 1879), as shown in equation (2.19), the 1-K^2 term exists. Regarding the definition of K=kb in equation (2.68), it can be assumed that capillary term of an elliptic jet is equal to that of a circular jet with a radius equal to the semi-minor axis. Dityakin (1954) used the same assumption and derived dispersion equation of elliptic liquid jets.

Similar to the analysis of asymmetric disturbances on a circular jet, to the Fourier form of an initial disturbance η_0 in equation (2.54), a term of azimuthal mode of $e^{im\theta}$ can be added (Rayleigh 1879; Yang 1992) and consequently in equation (2.67),

$$\gamma^2 - K^2 = 1 - m^2 - K^2. \tag{2.75}$$

It is important to note that in a circular jet, higher modes grow only in short wavelengths disturbances, i.e. when $K >> 1$ so that $m << K$ (Yang 1992).

2.4 Results and discussion

In this section, the growth rate of initial disturbances is shown for a wide range of Weber numbers covering Rayleigh as well as the first and second wind-induced regimes. In addition, the effect of gas to liquid density ratio is studied. Dispersion relation of (2.67) gives the growth rate of disturbances for various azimuthal modes. However, the theoretical study is limited to the modes with lower transverse orders, because only the lowest order modes dominate the unstable fluid flow and the higher order eigensolutions are more oscillatory and are not frequently encountered in practice.

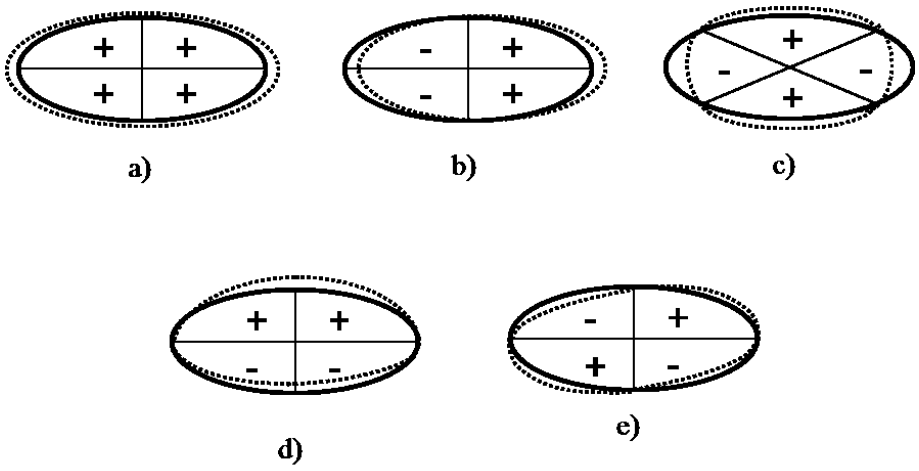

Figure 2.7: Depiction of the selected five modes of instability waves for elliptic jets: (*C*, *F*) modes including, a) Ce_0, b) Ce_1, c) Ce_2, and (*S*, *G*) modes including d) Se_1 and e) Se_2 (From Amini & Dolatabadi 2011b).

Results are summarized in two parts as (*C*, *F*) and (*S*, *G*) modes, which are even and odd to the major axis, respectively. These deformation modes are shown schematically in figure 2.7. The notations *Ce* and *Se* refer to "cosine elliptic" and "sine elliptic", respectively. (*C*, *F*) form is composed of Ce_0, Ce_1, and Ce_2 modes, while (*S*, *G*) form is composed of Se_1, and Se_2 modes. Ce_0 represents disturbances which are symmetric about both the major and minor axes, and

corresponds to an axisymmetric motion in a circular jet. Ce_1 represents disturbances which are symmetric (even) about major axis but antisymmetric (odd) about minor axis indicating flapping of the jet about the major axis. On the other hand, Se_1 is representing disturbances symmetric (even) about minor axis and antisymmetric (odd) about major axis indicating flapping of the jet about the minor axis. This mode is similar to the sinuous mode in planar liquid sheets and corresponds to the helical mode, m=1, in the circular jet. Ce_2 and Se_2 represent axis-switching and torsional modes, respectively. When aspect ratio is one (i.e. a circular jet) shapes of Ce_m and Se_m modes are the same.

Instability regions and disturbance growth rates are plotted in figures 2.8 to 2.13. Dimensionless growth rate, i.e. Strouhal number, is represented by β and is defined as $-\alpha_i R/V$ where R is radius of the equivalent area circle and V is mean jet velocity in the axial direction. In addition, dimensionless axial wavenumber is defined as kR. In these figures, Weber number is calculated based on the jet equivalent radius, R, i.e. $We = \rho_l R V^2 / \sigma$. The gas to liquid density ratio, Q, is typically of order of 10^{-3}. A density ratio of 0.0013 has been used in the current calculations which corresponds to that of air to water. Additionally, to show the effect of density ratio, growth rate of different unstable modes was shown for a density ratio of 0.1. Details of modes even (C, F) and odd (S, G) to the major axis are presented in the next sections.

2.4.1 (*C*, *F*) modes

These modes represent configurations where disturbances are even to the major axis. Figures 2.8 to 2.11 present disturbance growth rates and the corresponding wavenumbers for several aspect ratios and Weber numbers. Figure 2.8 shows Ce_0 mode for Weber numbers of 10, 10^2, 10^3 and 10^4. This figure reveals that for all aspect ratios, by increasing the Weber number, range of

unstable wavenumbers is continuously increased. Weber numbers of 10 and 10^2 belong to the Rayleigh regime, while the Weber numbers of 10^3 and 10^4 belong to the first and second wind-induced regimes, respectively. Similar to the circular and planar jets, long wave regime is dominant for low-speed instability, while short waves are responsible for breakup in the case of high-speed jets. Thus instability growth rate decreases continuously as *We* number is increased from 10 to 10^3. Transition from a long wave regime to a short wave regime is comparable with the first and second wind-induced breakup regimes of circular liquid jets (Senecal et al. 1999). The jet inertia assists the surface tension force in the destabilization process in the first wind-induced regimes. However, capillary force has a stabilizing effect when the Weber number is sufficiently high (i.e. 10^4, in the second wind-induced regime) and the growth rate increases significantly as shown in figure 2.8d.

As shown in figure 2.8, for Weber numbers up to 10^3, by decreasing the aspect ratio, the maximum growth rate becomes larger and shifts toward the shorter wavelengths. Furthermore, increasing the ellipticity increases the range of unstable wavenumbers. However, the behaviour is different for Weber number of 10^4 representing the second wind-induced regime. In this case, by increasing the ellipticity, disturbance growth rate and the range of unstable wavenumbers are decreased. This transition can be explained by the fact that for Rayleigh and the first wind-induced regimes, the capillary force plays a destabilizing role. Therefore for a given volume, elliptic cylindrical jet has more surface area (and energy) than a circular cylindrical jet, and tends to disintegrate faster. On the other hand, for higher Weber numbers, the effect of ellipticity is diminishing the instability due to the stabilizing effect of surface tension force against destabilising effects of aerodynamic forces. This conclusion is confirmed by current experimental results and also by measurements of Kasyap et al. (2009).

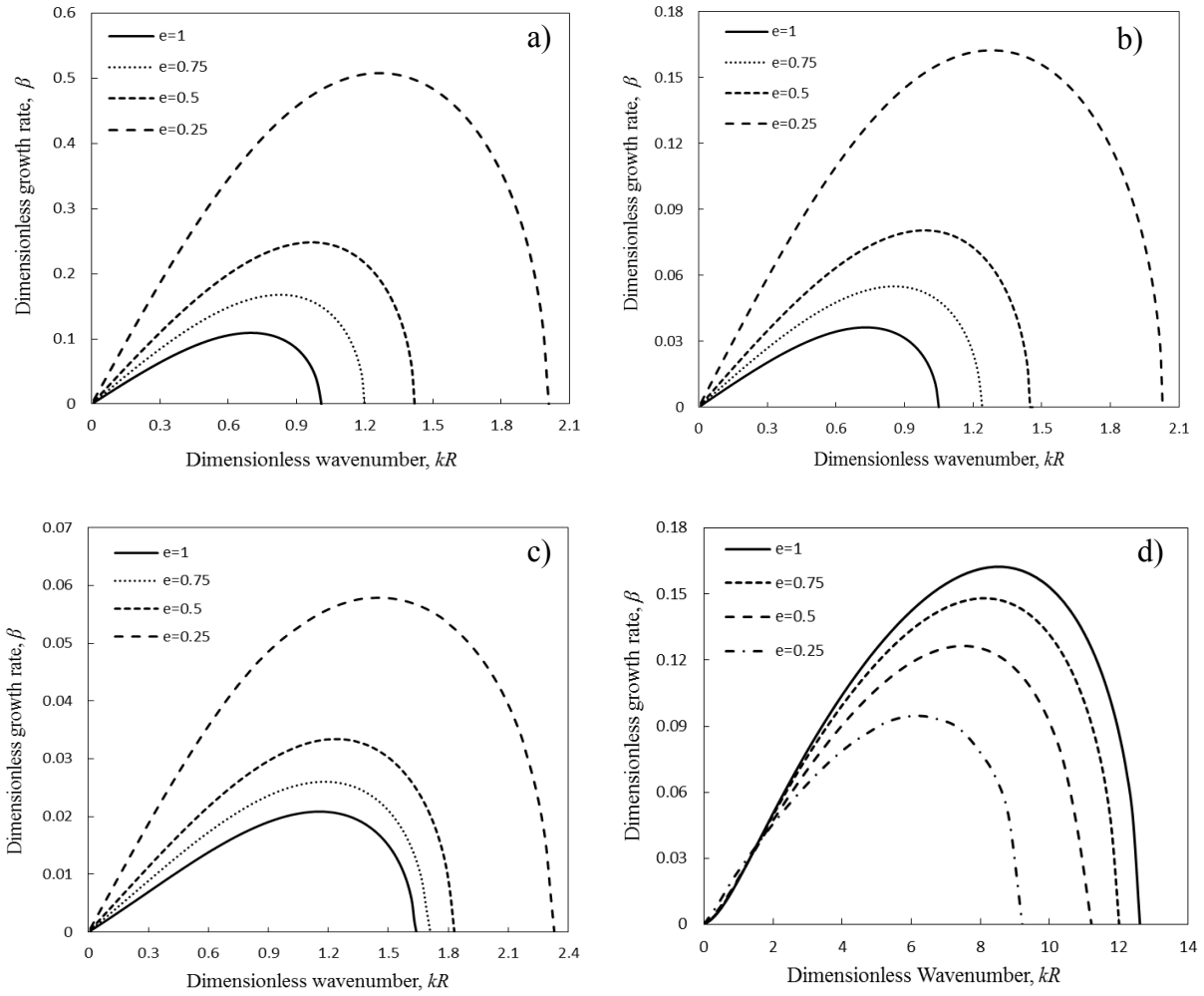

Figure 2.8: Growth rate of Ce_0 mode at Q=0.0013 for a) We=10, b) We =10^2, c) We=10^3, and d) We=10^4.

At Weber numbers of 10 and 10^2 only the axisymmetric mode (Ce_0) can grow and all other modes are stable. When the Weber number is increased to 10^3, the Ce_1 has a nonzero growth rate. Figure 2.9 shows Ce_1 mode for Weber numbers of 10^3 and 10^4. Results show that for Ce_1 mode, by decreasing the ratio of the minor to the major axis, e, growth rate is decreased. For Weber number of 10^3, the axisymmetric mode (Ce_0) possesses a higher growth rate than Ce_1 mode. However for Weber number of 10^4, the growth rate of these two modes are almost of the same order of magnitude. In addition, for Weber number of 10^3 and for aspect ratios less than

0.75, Ce_1 mode does not grow as shown in figure 2.9a. By further increasing the Weber number to the value of 10^4, in addition to Ce_0 and Ce_1, Ce_2 mode also grows (figure 2.10). Similar to the case of Ce_1 mode, figure 2.10 shows that by decreasing the aspect ratio, the growth rate of Ce_2 mode is decreased.

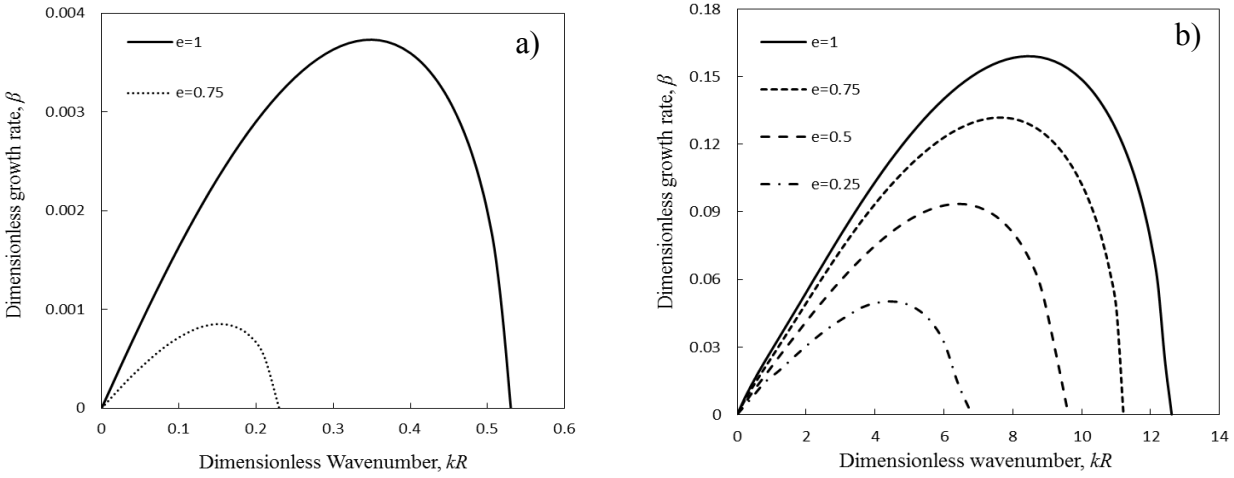

Figure 2.9: Growth rate of Ce_1 mode for a) We=10^3 and b) We =10^4 in Q=0.0013. Invisible aspect ratios are stable in this mode.

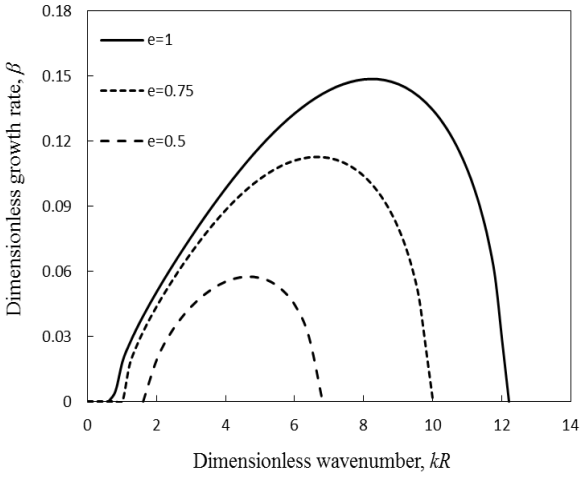

Figure 2.10: Growth rate of Ce_2 mode for We=10^4 at Q=0.0013. Aspect ratios less than 0.5 are stable in this mode.

In the circular jet case, Ce_0, Ce_1, and Ce_2 modes reduce to the axisymmetric, helical and elliptic modes, respectively (See figure 2.1). Due to symmetry of circular jets, results in Ce_1, and Ce_2 modes are, respectively equal to Se_1, and Se_2 modes. The growth rate calculation for e=1 for all modes are equal to those of Yang (1992) for a circular jet (See figure 2.11).

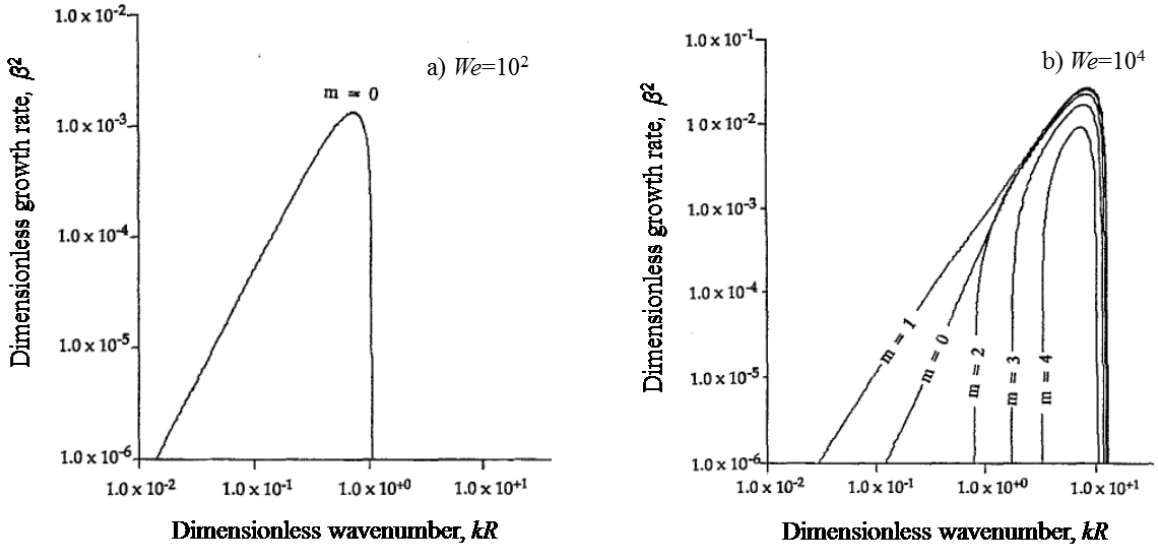

Figure 2.11: Growth rate of various azimuthal modes on a circular jet for a) We=10^2 and b) We=10^4 at Q=0.0013 (Adapted from Yang 1992).

2.4.2 (*S*, *G*) modes

These modes represent configurations where disturbances are odd to the major axis. Figure 2.12 shows the growth rate of disturbances in these modes for various aspect ratios. Se_1 mode can be identified with a flapping motion in the plane of the minor axis while Se_2 mode represents torsion. These modes did not appear in Weber numbers of 10, 10^2, and 10^3. In fact, these disturbances grow only for a sufficiently high Weber numbers (i.e. We=10^4) as shown in the experiments of Kasyap et al. (2009). As can be seen from figure 2.12, the growth rate of Se_1 mode in elliptic jets is less than circular jets. On the other hand, Se_1 mode exists for aspect ratios

$e \geq 0.75$ and Se_2 mode exists only for aspect ratios $e \geq 0.9$. In fact, the ellipticity has a stabilizing effect for these modes. As mentioned in the previous section, for a circular jet Se_1 and Ce_1 are the same. This is also the case for Se_2 and Ce_2 modes.

To summarize the results obtained for (*C*, *F*) and (*S*, *G*) modes, one can conclude that for capillary elliptic jets, the only growing mode is Ce_0 (i.e. axisymmetric mode), and the other modes appear only in higher Weber numbers where aerodynamic effects cannot be ignored. The Ce_1 mode, which represents a flapping motion in the plane of the major axis, has a larger amplification rate than that of Se_1 mode, which represents a flapping motion in the plane of the minor axis. Generally, results show that the amplification rates of (*S, G*) modes are smaller than those of (*C, F*) modes. In small Weber numbers, disturbances in Ce_0 mode control the instability process, while in large Weber numbers, disturbances of Ce_1, Ce_2 modes are also taken into account.

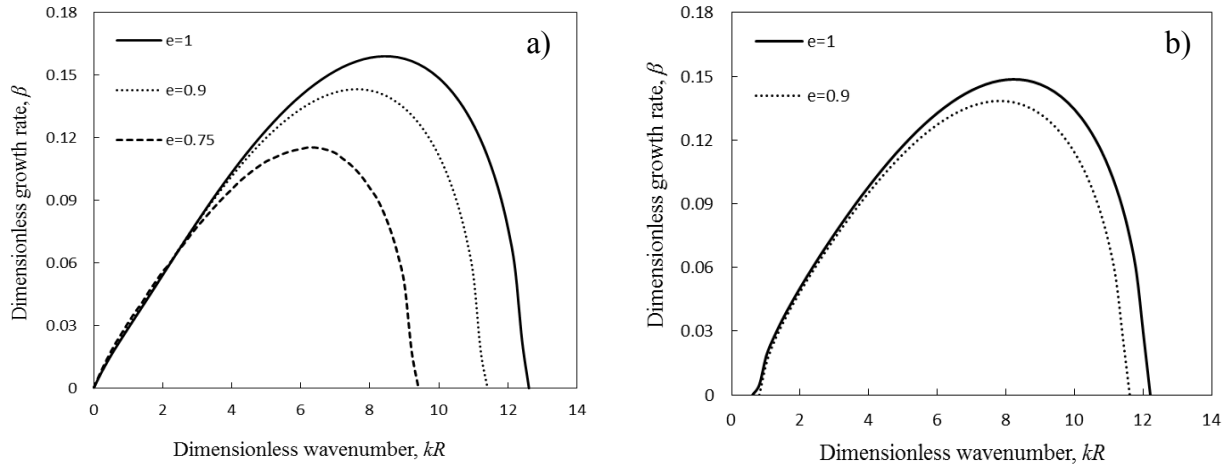

Figure 2.12: Growth rate of a) Se_1 and b) Se_2 modes for $We=10^4$ and $Q=0.0013$. Growth rate of invisible aspect ratios are zero in these modes.

The effect of surrounding gas density on the disturbance growth rate can be illustrated from figure 2.13. The results are presented for a gas to density ratio of 0.1 and Weber number of 10^2. Comparing the growth rate of different modes for this density ratio with those of figures 2.8b for the same Weber number but a density ratio of 0.0013, reveals the strong effect of this parameter. At $Q = 0.0013$ the only growing mode was Ce_0 whereas, for $Q = 0.1$ other modes appear. Figure 2.12a represents the growth rate of axisymmetric mode for various ellipticities. Compared to the results of the same Weber number as presented by figure 2.8b, increasing the density ratio significantly changes the trend of instability region. In this case, compared to the capillary force, the aerodynamic forces are dominant. Therefore a circular jet is associated with the highest growth rate and ellipticity stabilizes the perturbing waves. Additionally, due to the effect of high density ratio, other modes including Ce_1, Ce_2, Se_1, and Se_2 appear which were not present for $We = 10^2$ at $Q = 0.0013$.

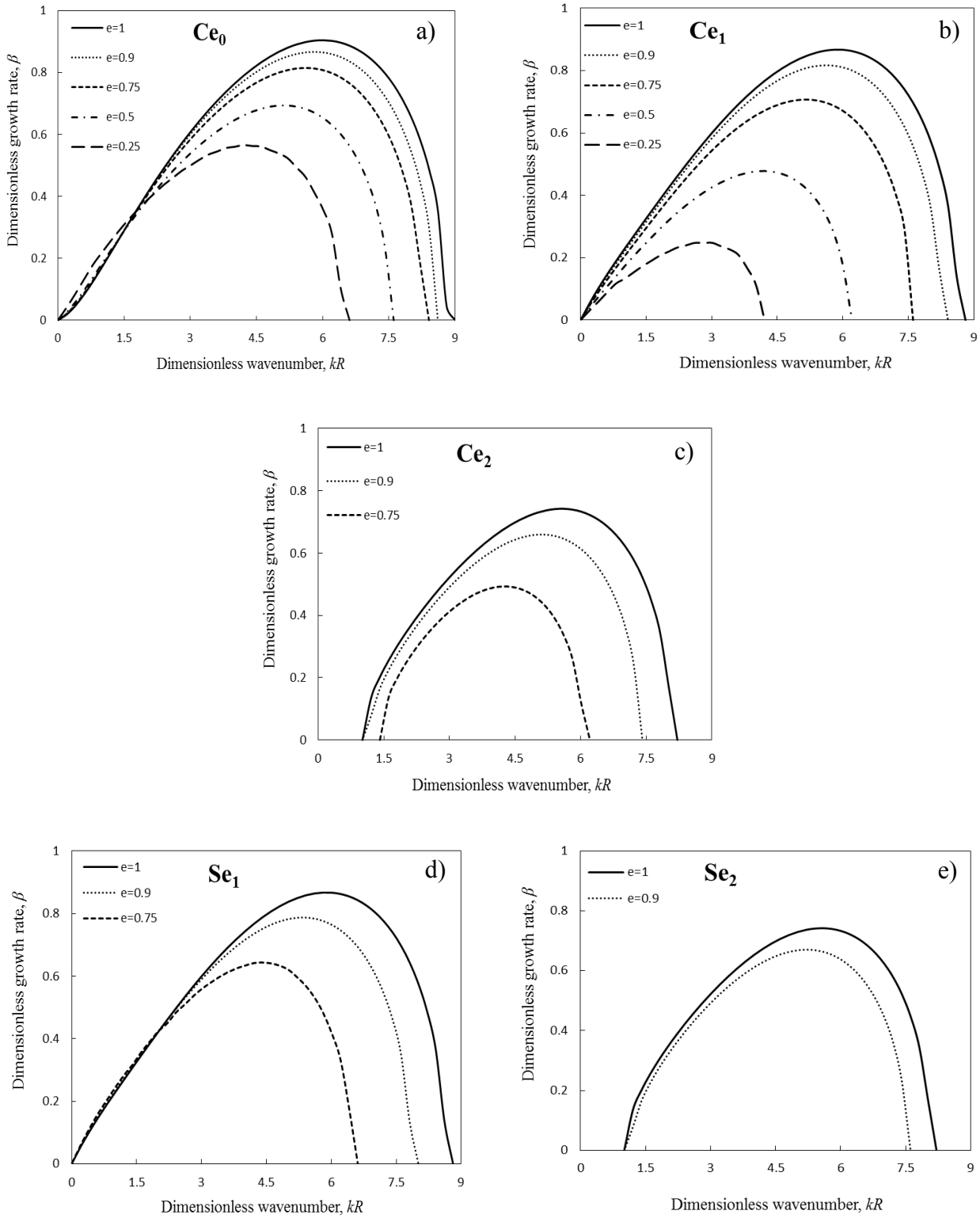

Figure 2.13: Growth rate of different modes for We=10^2 and Q=0.1. Growth rate of invisible aspect ratios are zero.

2.4.3 Special case 1: circular jet

Circular configuration can be considered as a special case of an ellipse when major and minor axes are equal. Correspondingly, dispersion relation of a circular jet can be found from that of the elliptic jet. In equation (2.67), asymptotics for the modified Mathieu functions as $\rho \to \infty$ and $q \to 0$, i.e. a circular jet (McLachlan 1964) are,

$$\xi \to \frac{I_m(K)}{I'_m(K)}, \quad \zeta \to -\frac{K_m(K)}{K'_m(K)} \tag{2.76}$$

and consequently,

$$\frac{\xi}{\zeta} = -\frac{I_m(K)}{I'_m(K)} \frac{K'_m(K)}{K_m(K)}. \tag{2.77}$$

With these asymptotic values, equation (2.67) is the direct analogy to the dispersion equation (2.17) for the m^{th} order azimuthal perturbations of a circular jet of radius b (Yang 1992). For a specific case of $m=0$,

$$\frac{\xi}{\zeta} = \frac{I_0(K)}{I_1(K)} \frac{K_1(K)}{K_0(K)}. \tag{2.78}$$

For a negligible value of ρ_g, equation (2.67) reduces to,

$$\alpha_i \sqrt{\frac{\rho_l b^3}{\sigma}} = -\sqrt{K(1-K^2)\frac{I_1(K)}{I_0(K)}}, \tag{2.79}$$

which is derived originally by Rayleigh (1879).

Calculation of growth rate and phase velocity for a case of density ratio equal to one and no surface tension effects for a cylindrical vortex sheet is possible through equation (2.67). In this case, imaginary roots of nontrivial solution from equation (2.67), i.e. growth rate, will be in the following form,

$$\frac{\alpha_i b}{V} = -\frac{\sqrt{K^2(\xi/\zeta)}}{1+(\xi/\zeta)}. \tag{2.80}$$

Considering $K = kb$, equation (2.80) takes the form,

$$\frac{\alpha_i}{k} = -\frac{\sqrt{(\zeta/\xi)}}{1+(\zeta/\xi)}V. \tag{2.81}$$

Similarly, the real root of nontrivial solution in equation (2.67) will result in phase velocity (wave speed) as follows,

$$\frac{\alpha_r}{k} = \frac{(\xi/\zeta)}{1+(\xi/\zeta)}V. \tag{2.82}$$

Equations (2.81) and (2.82), respectively, result in amplification factor and wave speed for a disturbance to an elliptical cylindrical vortex sheet as derived by Morris (1986). In specific case of e=1, the above equations reduce to those of Batchelor & Gill (1962) for a circular vortex sheet.

2.4.4 Special case 2: planar sheet

A liquid sheet can also be modeled as a special case of an elliptic jet when ellipticity is large. Asymptotic for the modified Mathieu functions as $\rho \to 0$ and $q \to \infty$ (McLAchlan 1964, Crighton 1973) in (C, F) mode is given by,

$$\frac{\xi}{\zeta} \to \coth(K) \tag{2.83}$$

and similarly in (S, G) mode is given by,

$$\frac{\xi}{\zeta} \to \tanh(K). \tag{2.84}$$

Using asymptotic values in equations (2.83) and (2.84), dispersion equation of (2.67) takes a form similar to varicose shape (equation (2.37)) for (C, F) mode and sinuous shape (equation

(2.36)) for (*S*, *G*) mode. These two dispersion equations were derived originally by Hagerty & Shea (1955) for the waves propagating on the surface of a two dimensional liquid jet with a thickness of 2*b*. It is important to note that for this case, term γ in equation (2.66) should be calculated for $\theta=\pi/2$, i.e. along the minor axis, where by increasing ellipticity, the radius of curvature is infinity (similar to a planar sheet). However, term of k^3b^3 in equations (2.36) and (2.37) is not fully recovered from equation (2.67).

Chapter 3

Instability of Viscous Elliptic Jets

The complexity of viscous free surface flow analysis for an asymmetric geometry can be simplified using an approach based on the Cosserat theory (also called director theory). This method reduces the exact three-dimensional equations to a system depending only on time and on a single spatial variable. One-dimensional Cosserat equations can be assumed as a low order form of Navier-Stokes equations for slender jets (Bechtel et al. 1988). This quasi-one-dimensional model which inherently contains the radial inertia effects in its equations gives the jet profile as a function of axial coordinate only and simplifies the analysis considerably. The Cosserat equations which are used here were derived originally by Caulk & Naghdi (1979) for liquid jets emerging from a nozzle with elliptic cross-section. Governing equations are high order nonlinear partial differential equations (PDE) which determine the position of the free surface.

In this chapter, an overview of the instability of viscous circular and planar jets comes first. Then using perturbation methods, one-dimensional Cosserat equations are linearized and solved

to investigate the Rayleigh instability of viscous elliptic liquid jets. The current model considers only long wavelengths disturbances and the case of short wavelength which prevails when aerodynamic forces become important is not covered. Both temporal and spatial instability analyses are performed while the main focus is on the spatial instability to examine the key characteristics of an elliptic jet such as jet profile, axis-switching and breakup length. Liquid jet instability is studied for various ellipticities over a specific range of jet velocities and excitation frequencies. Results are compared with conventional circular nozzles which can be considered as a special case of an elliptic jet.

3.1 Instability of viscous circular jets

Considering the aerodynamic forces and liquid viscosity, Sterling and Sleicher (1975) derived a dispersion equation for axisymmetric disturbances on the surface of a circular jet. Their equation, in case of long wave disturbances ($kb << 1$) reduces to the following form,

$$\frac{\alpha_i b}{V} = -\frac{\sqrt{(3k^2b^2\,Oh/\sqrt{We})^2 + 2Qk^3b^3\,[K_0(kb)/K_1(kb)] + (2k^2b^2/We)(1-k^2b^2)}}{2} + \frac{(3k^2b^2\,Oh/\sqrt{We})}{2} \tag{3.1}$$

where α_i is the disturbance growth rate and k is the axial wavenumber. Jet radius is represented by b, and K_0 and K_1 are modified Bessel functions of the second kind, order of zero and one, respectively. Ohnesorge number, Weber number, and density ratio are defined as $Oh = \mu_l / \sqrt{\rho_l b \sigma}$, $We = \rho_l b V^2 / \mu_l$, and $Q = \rho_g / \rho_l$, respectively. For a case of insignificant aerodynamic forces ($Q = 0$), the equation (3.1) reduces to dispersion equation of weber (1931). In this case, growth rates of disturbances are plotted in figure 3.1 where $\omega = -\alpha_i \sqrt{\rho_l R^3 / \sigma}$. As

can be seen, the effect of viscosity is reducing the amplification factor (growth rate) and shifting the maximum growth rate to the larger wavelengths which results in larger droplets.

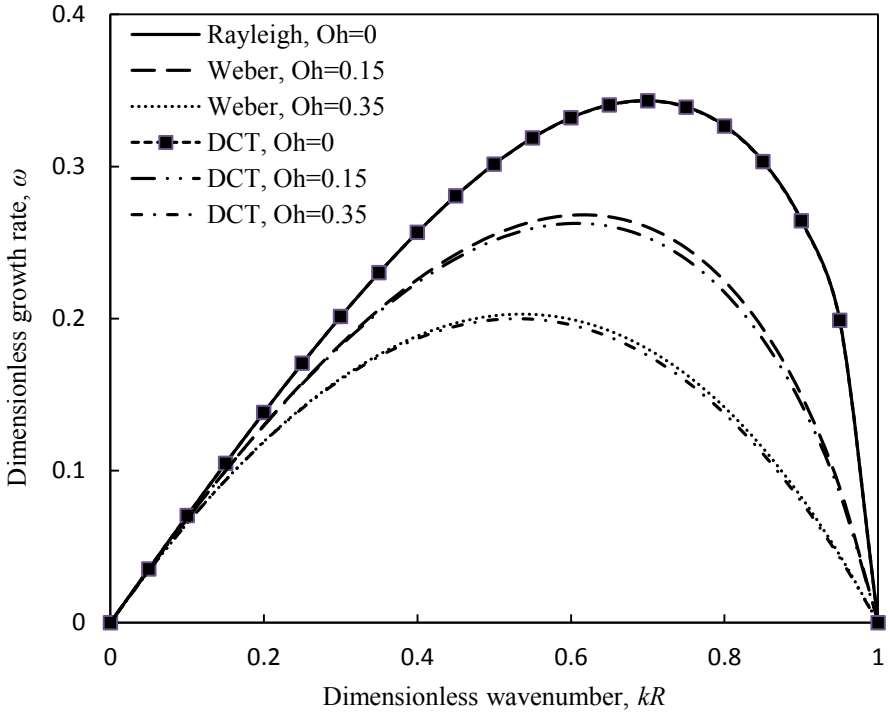

Figure 3.1: Temporal growth rate of axisymmetric disturbances on a viscous circular jet; comparison of results of Rayleigh (1879) and Weber (1931) with that of DCT (Directed Curve Theory) model (From Amini & Dolatabadi 2011a).

In the classic approach, Navier-Stokes equations and mass conservation are followed by normal stress and kinematic boundary conditions. Accordingly, in the directed curve model the field equations are consequences of balance of mass, linear momentum, director momentum and moment of momentum which followed by boundary conditions including the attachment of material to surface and discontinuity in normal traction balance. Applying Cosserat theory on a circular jet results in the following equations (Green 1976); the continuity equation results in,

$$(\phi^2)_t + (v\phi^2)_z = 0 \tag{3.2}$$

and momentum balance in the radial and axial directions reads as,

$$-\frac{1}{8}\pi\rho\phi^4(v_{zt}+vv_{zz}-0.5v_z^2)=p-\pi\sigma(\frac{\phi}{(1+\phi_z^2)^{0.5}}-\frac{\phi^2\phi_{zz}}{(1+\phi_z^2)^{1.5}})+\mu\pi\phi^2v_z-\frac{1}{8}\mu\pi(\phi^2v_{zz})_z$$
$$\pi\rho\phi^2(v_t+vv_z)=-p_z+2\pi\sigma(\frac{\phi}{(1+\phi_z^2)^{0.5}})_z+2\mu\pi(\phi^2v_z)_z \tag{3.3}$$

where ϕ is the jet radius, v is the axial jet velocity, p is the resultant pressure across a section of the jet, ρ is mass density (assumed constant), μ is the liquid viscosity, and σ is surface tension coefficient. Subscripts t and z represent partial derivative with respect to t and z, respectively. Equations (3.2) and (3.3) have been solved linearly by Bogy (1978a) and Caulk & Naghdi (1979) and a temporal dispersion equation was derived. Based on this analysis, the effect of viscosity on growth rate of disturbances is shown in figure 3.1. The results obtained by Weber (1931) and Rayleigh (1879) are also presented in this figure which shows an excellent agreement with the above quasi-one-dimensional analysis.

3.2 Instability of viscous planar sheets

Li & Tankin (1991) and Senecal et al. (1999) added the viscous terms to the inviscid analysis of Hagerty and Shea (1955) and derived new dispersion equations for viscous liquid sheets. As a result, the dispersion equation (2.36) of inviscid sheet takes the following form,

$$\frac{\alpha_i b}{V}=-\frac{\sqrt{[2k^2b^2\tanh(kb)Oh/\sqrt{We}]^2+Qk^2b^2\tanh(kb)-(k^3b^3/We)[\tanh(kb)+Q]}}{\tanh(kb)+Q}$$
$$+\frac{[2k^2b^2\tanh(kb)Oh/\sqrt{We}]}{\tanh(kb)+Q} \tag{3.4}$$

for the sinuous mode, and equation (2.37) changes to,

$$\frac{\alpha_i b}{V} = -\frac{\sqrt{[2k^2b^2\coth(kb)Oh/\sqrt{We}]^2 + Qk^2b^2\coth(kb) - (k^3b^3/We)[\coth(kb)+Q]}}{\coth(kb)+Q} + \frac{[2k^2b^2\coth(kb)Oh/\sqrt{We}]}{\coth(kb)+Q} \tag{3.5}$$

for varicose mode. Li & Tankin (1991) showed that there exist two modes of instability for viscous liquid sheets; aerodynamic and viscosity enhanced instability, in contrast to inviscid liquid sheets for which the only mode of instability is aerodynamic. Aerodynamic instability dominates and the viscous effect reduces the wave growth rate for the sinuous mode at large Weber numbers and for the varicose mode at any Weber number. However, liquid viscosity can enhance the liquid sheet instability for the sinuous mode at low Weber numbers, and under this condition the viscosity enhanced instability can even become predominant. At an intermediate Weber-number range, liquid viscosity has complicated effects. For axisymmetric disturbances, liquid viscosity always reduces the growth rate dominant wavenumber, and aerodynamic instability always prevails. For a liquid sheet, the surface tension always stabilizes, while surrounding gas and relative velocity between the sheet and gas favor the onset and development of instability. Linear analysis shows that, in contrast to circular jets, no temporal capillary instability exists for purely two dimensional planar sheets (in absence of edge-effects).

3.3 Instability of viscous elliptic jets

In this section, quasi-one-dimensional Cosserat equations of Caulk & Naghdi (1979) will be used to study instability of elliptic liquid jets. Governing equations are high order nonlinear PDEs which determine the position of the free surface. These equations are linearized and solved to investigate the Rayleigh instability of viscous elliptic liquid jets. Since gas phase does not present in the current analysis, for simplicity subscript *l* is deleted from all notations.

Cosserat theory for elliptic liquid jets is based on a quasi-one-dimensional continuum model where continuum is an oriented space curve corresponding to the jet axis. The behavior of the liquid jet is studied as the motion of a directed curve in a fixed system of coordinates (x, y, z), in which the material line is identified along the z-axis. Two deformable vectors (i.e. directors) are attached to every point of the curve and lie in the x-y plane which represent the cross-section of the jet. A complete set of the equations includes,

$$\zeta_1 + \zeta_2 + v_z = 0 \tag{3.6}$$

as the continuity equation and,

$$\begin{aligned} &\phi_{1t} + v\phi_{1z} - \phi_1\zeta_1 = 0 \\ &\phi_{2t} + v\phi_{2z} - \phi_2\zeta_2 = 0 \end{aligned} \tag{3.7}$$

as equations for motion of directors and finally,

$$\begin{aligned} &\frac{1}{4}\pi\rho\phi_1^3\phi_2(\zeta_{1t} + v\zeta_{1z} + \zeta_1^2) = p + \phi_1\phi_2 h(\phi_1,\phi_2) - 2\mu\pi\phi_1\phi_2\zeta_1 + \frac{1}{4}\mu\pi(\phi_1^3\phi_2\zeta_{1z})_z \\ &\frac{1}{4}\pi\rho\phi_2^3\phi_1(\zeta_{2t} + v\zeta_{2z} + \zeta_2^2) = p + \phi_1\phi_2 h(\phi_2,\phi_1) - 2\mu\pi\phi_1\phi_2\zeta_2 + \frac{1}{4}\mu\pi(\phi_2^3\phi_1\zeta_{2z})_z \\ &\pi\rho\phi_1\phi_2(v_t + vv_z) = -p_z - \phi_2\phi_{1z}h(\phi_1,\phi_2) - \phi_1\phi_{2z}h(\phi_2,\phi_1) + 2\mu\pi(\phi_1\phi_2 v_z)_z \end{aligned} \tag{3.8}$$

as the conservation of momentum in x, y, and z directions, respectively. In the above equations, ϕ_1 and ϕ_2 are semi-major and semi-minor axes, respectively. They are both functions of time, t, and axial distance, z (See figure 3.2). ζ_1 and ζ_2 are the material derivatives of the semi-major and the semi-minor axes divided by their length, respectively. They indicate the jet column deformation in the transverse directions and will be eliminated from the equations during the solution. v is the axial jet velocity, p is the average pressure over the jet cross-section, ρ is the density, and μ is the dynamic viscosity. Subscripts z and t represent the partial derivatives with

respect to the axial coordinate and time, respectively. h is related to the average of capillary force over the cross-sectional area and is presented by equation (3.9),

$$h(\phi_1,\phi_2)=\int_0^{2\pi}(\sigma\kappa\cos^2\theta)d\theta \tag{3.9}$$

where σ is the surface tension coefficient and κ is the mean curvature of ellipse given by,

$$\kappa=[(\phi_1\phi_{2z}\sin^2\theta+\phi_2\phi_{1z}\cos^2\theta)^2+\phi_1^2\sin^2\theta+\phi_2^2\cos^2\theta]^{-1.5}\times$$

$$[(\phi_1^2\sin^2\theta+\phi_2^2\cos^2\theta)(\phi_{1zz}\phi_2\cos^2\theta+\phi_{2zz}\phi_1\sin^2\theta)+ \tag{3.10}$$

$$2(\phi_1\phi_{2z}-\phi_2\phi_{1z})(\phi_1\phi_{1z}-\phi_2\phi_{2z})\sin^2\theta\cos^2\theta-\phi_1\phi_2(\phi_{1z}^2\cos^2\theta+\phi_{2z}^2\sin^2\theta+1)]$$

and θ is the azimuthal angle in the plane of the cross-section given by,

$$(y/x)=(\phi_2/\phi_1)\tan\theta. \tag{3.11}$$

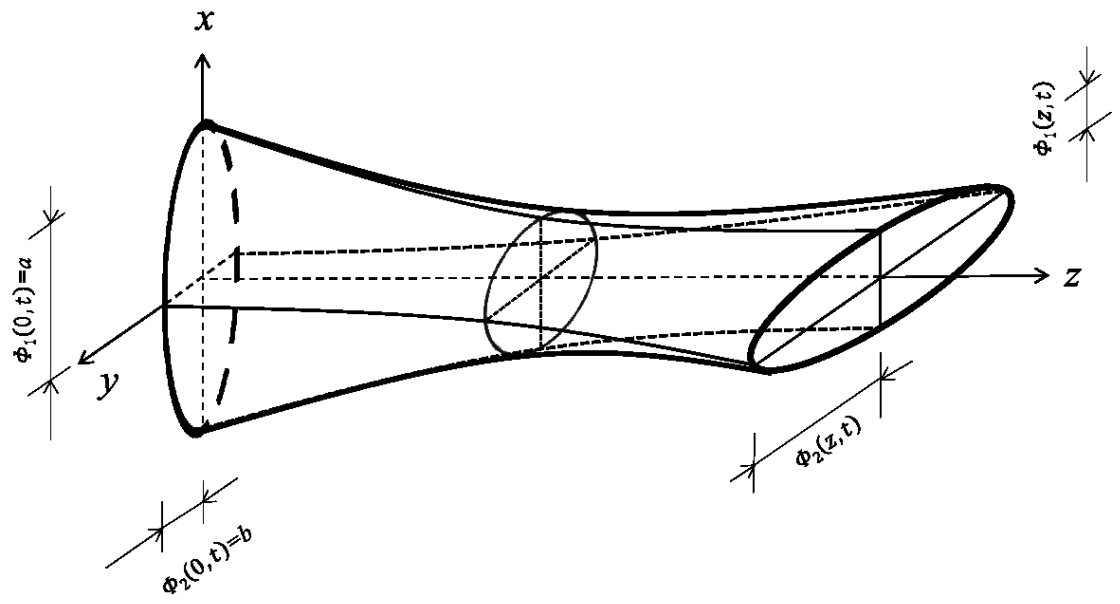

Figure 3.2: Change in cross-sectional shape of an elliptic jet in Cartesian coordinates.

Equations (3.6), (3.7), and (3.8) are highly nonlinear and difficult to solve analytically or numerically. Applying perturbation methods may simplify them considerably. To linearize equations of (3.6), (3.7), and (3.8), the main parameters are expanded as,

$$\phi_1 = a + \bar{\phi}_1, \qquad \phi_2 = b + \bar{\phi}_2, \qquad p = p_0 + \bar{p}, \qquad v = V + \bar{v}. \tag{3.12}$$

The bar mark represents the value of the perturbed parameter. a and b are the initial semi-major and semi-minor axes, respectively (See figure 3.2). The uniform jet velocity is represented by V, and p_0 is the initial pressure and is assumed constant inside the liquid column.

Perturbation can be considered as a superposition of Fourier components which have the form of $A\exp[(i(\alpha t - kz)]$, where A is the wave amplitude and $k = k_r + ik_i$ is the complex axial wavenumber whose real and imaginary parts represent, respectively, the number of waves over a distance 2π and the exponential spatial growth rate per unit length in the axial z-direction. Similarly, $\alpha = \alpha_r + i\alpha_i$ is the complex wave frequency, the real and imaginary parts of which give, respectively, the frequency of the Fourier wave and the exponential temporal growth rate. The instability of liquid surface to perturbations is converted mathematically to the condition of the existence of nontrivial solution of the linear system which ultimately leads to a dispersion equation. Dispersion equation relates the growth rate α of an initial perturbation of infinitesimal amplitude to its wavenumber k (or wavelength). The results indicate that there is a maximum wave growth rate α_{max}, which occurs at a wavelength of λ_{max}. The maximum wave growth rate and the corresponding wavelength characterize the fastest growing (or the most probable) waves on the liquid surface that are eventually responsible for the breakup.

Temporal analyses consider the growth of the perturbation magnitude with time rather than along the jet axis, as is considered in spatial analyses. Solution of the dispersion equation in

spatial case shows predicted wave growth rate, α, versus wavenumber, k, as a function of Weber number. In the following sections, equations (3.6), (3.7), and (3.8) will be solved temporally and spatially using linear expansions.

3.3.1 Temporal solution

In the temporal analysis, the perturbations are spatially harmonic, therefore with a selected frame of reference one may write $V=0$. $\bar{\phi}_1$ and $\bar{\phi}_2$ can be expanded as,

$$\bar{\phi}_1 = f_1(k)\exp[i(\alpha t - kz)]$$
$$\bar{\phi}_2 = f_2(k)\exp[i(\alpha t - kz)]. \tag{3.13}$$

Additionally, pressure term can be eliminated among three equations in (3.8). As the perturbation is small, the products of its magnitude can be neglected, resulting in a linear analysis and remaining only the following two equations.

$$S_1\bar{\phi}_1 + S_2\bar{\phi}_2 = 0$$
$$S_3\bar{\phi}_1 + S_4\bar{\phi}_2 = 0. \tag{3.14}$$

S_1, S_2, S_3 and S_4 are functions of wavenumber and have been defined in Appendix C. Temporal dispersion equation can be found by condition of nontrivial solution of $S_1S_4 - S_2S_3 = 0$ which finally leads to the following fourth order polynomial.

$$\sum_{j=0}^{4} a_j \omega^j = 0. \tag{3.15}$$

The coefficients in dispersion equation (3.15) have been defined in Appendix D which are functions of the following dimensionless numbers; (a) wavenumber defined as $K = kR$, (b) growth rate defined as $\omega = -\alpha_i\sqrt{\rho R^3/\sigma}$, and (c) Ohnesorge number defined as $Oh = \mu/\sqrt{\rho\sigma R}$.

R is the radius of a circle which has the same cross-sectional area as an ellipse, and *e* is the ratio of minor to major axes (i.e. aspect ratio).

Equation (3.15) has four roots which two of them are real and related to the oscillatory mode and do not grow with time. The other two roots are conjugate complex, one is damping with time and the other is growing with time responsible for the jet breakup. Dispersion curves have been plotted in figures 3.3 through 3.5 to demonstrate the variation of dimensionless growth rate, ω, versus dimensionless wavenumber, kR.

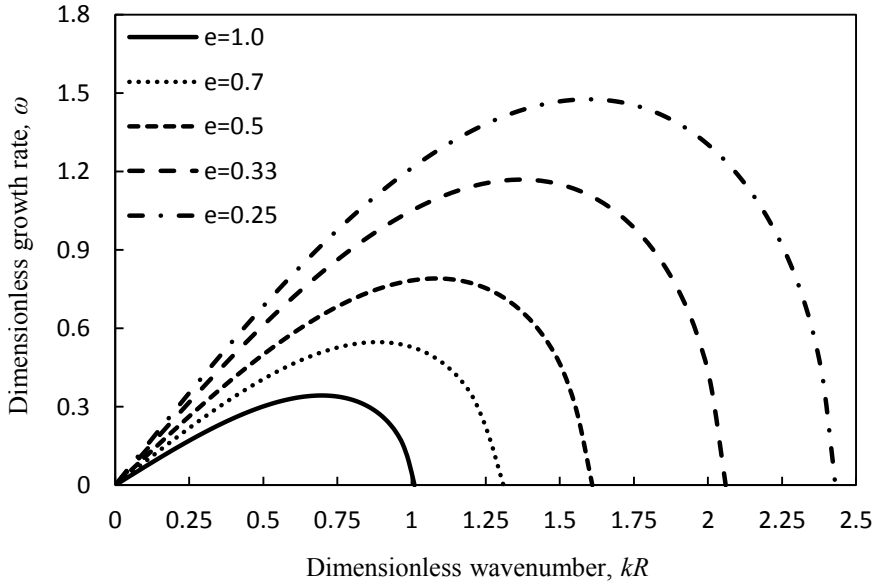

Figure 3.3: Growth rate ω versus wavenumber kR for different aspect ratios in inviscid elliptic jets.

Figure 3.3 shows that in comparison with a circular jet, the elliptic jet is more unstable and by decreasing the aspect ratio (i.e. by increasing the ellipticity), the instability grows faster. Since the maximum growth rate is responsible for breakup, one can conclude that breakup length of elliptic jet is shorter than that of the circular jet which confirms the results obtained experimentally. In addition as can be seen from figure 3.3, the range of unstable wavenumbers in the elliptic jets is larger than the circular jets.

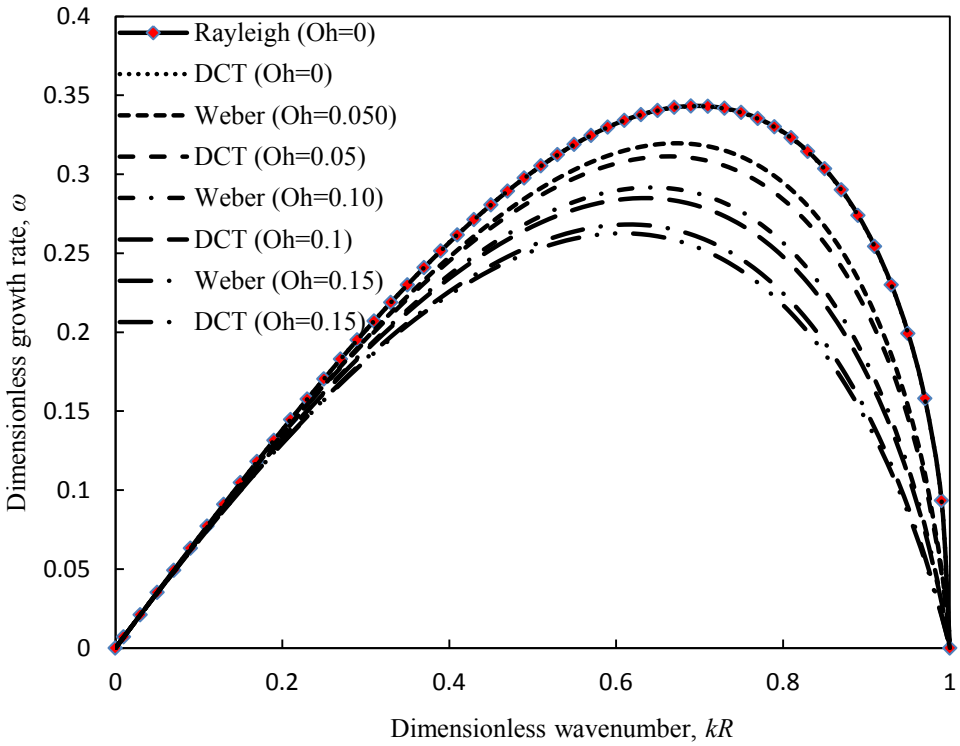

Figure 3.4: Comparison of the growth rate obtained by DCT (Directed Curve Theory) model in circular case, and the results of Rayleigh (1879) and Weber (1931) for different *Oh* numbers.

Figure 3.4 shows the effect of viscosity on the growth rate of disturbances on a circular jet. As can be seen, the effect of viscosity is diminishing the growth rate and shifting the maximum growth rate to longer wavelengths. These results are comparable with those of Rayleigh (1879) and Weber (1931). This figure shows that in the inviscid case, the difference between the results of quasi-one-dimensional model and Rayleigh's axisymmetric analysis is almost negligible (less than 0.25 %) which can serve as the validation for the developed quasi-one-dimensional modeling. Furthermore, quasi-one-dimensional results offer an improvement over Weber's result since Weber's model overpredicts the growth rate for moderate viscous jets (Caulk & Naghdi 1979). Similarly, figure 3.5 shows the effect of viscosity on growth rate of disturbances for a special case of $e = 0.5$.

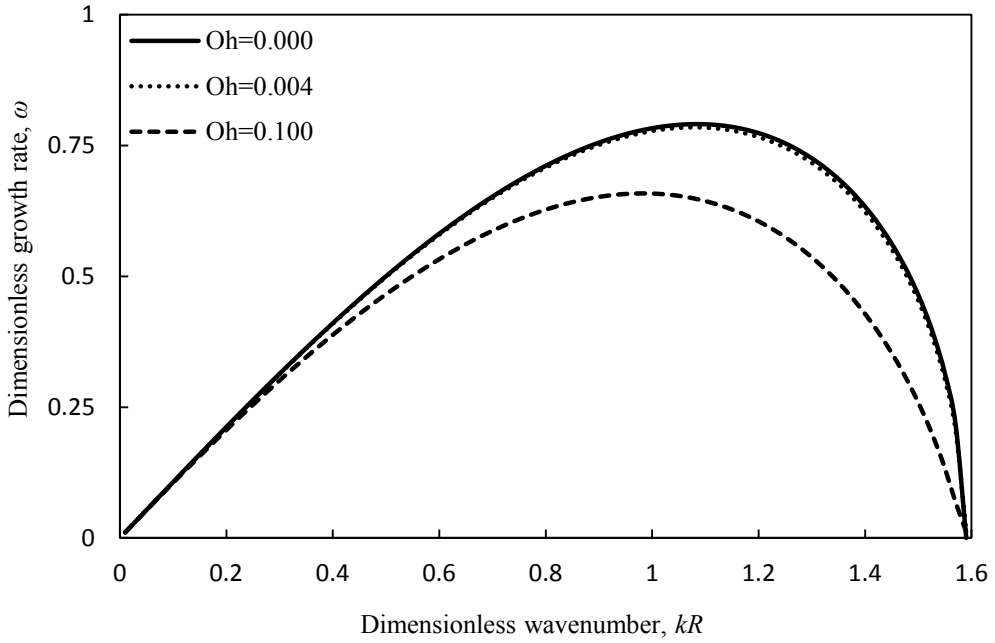

Figure 3.5: The effect of viscosity on the growth rate of disturbances on an elliptic jet with *e*=0.5.

Dityakin (1954) considered an infinitely long quiescent cylindrical liquid column issuing in a gas and modeled its response to a small perturbation of the shape of cross-section from basic circular shape. In his 3-D model, density of liquid and gas were included but their viscosities and gravity were ignored. In calculating the surface tension which is the main source of instability, due to the complexity of curvature calculation for ellipse, Dityakin (1954) restricted his analysis to small departures of the jet cross-section from circular shape. Instead of ellipse curvature, he simply used curvature of a circle with the radius of semi-minor axis. Even in this case calculations are long and tedious which detail can be found in the original article. The condition of nontrivial solution of resulted linear system leads to a dispersion equation. In case that gas density is ignorable in comparison with liquid density, his dispersion equation has been plotted in figure 3.6 for three aspect ratios.

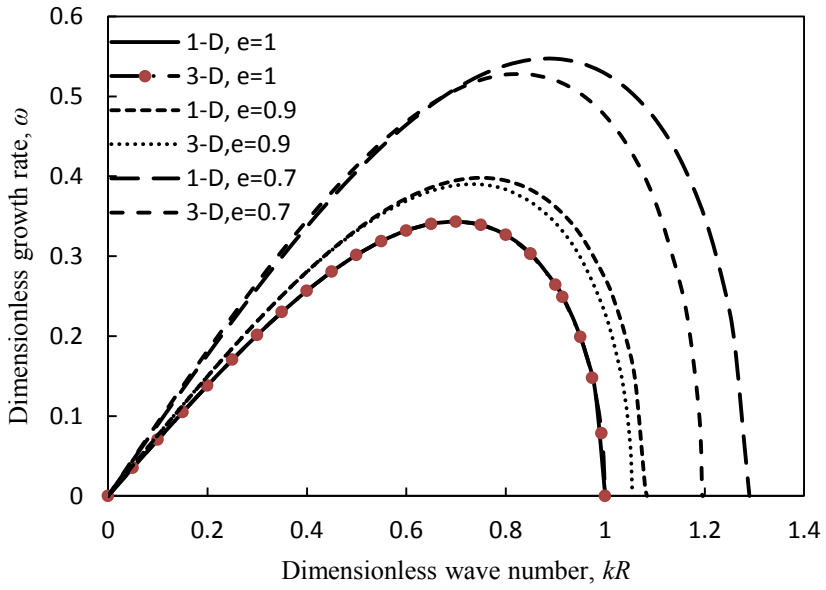

Figure 3.6: Growth rate ω versus wavenumber *KR* for inviscid 3-D (by Dityakin 1954) and present 1-*D* model.

As can be seen from figure 3.6, the difference between 3-D and 1-D results is negligible when aspect ratio is one (i.e. circle) but as aspect ratio is decreased, their difference is increased too. This result is reasonable because Dityakin's model is limited to infinitesimal deviations from a circle.

Knowing the ratio of $\bar{\phi}_2/\bar{\phi}_1$, both symmetric and asymmetric perturbations can be identified. A ratio of unity represents symmetric perturbation, while other values result in asymmetric perturbations. The ratio can be found from equation (3.14) as,

$$\frac{\bar{\phi}_2}{\bar{\phi}_1} = -\frac{S_1}{S_2} = -\frac{S_3}{S_4}. \tag{3.16}$$

Calculations show that for an elliptic orifice with an aspect ratio of *e*, unstable roots gives a ratio of one and stable roots gives a ratio of "–*e*" which means that unstable modes are symmetric and stable modes are asymmetric. For unstable mode, aspect ratio is increasing toward unity (but not

exceeding one), i.e. recovering a circular cross-section which has a smaller surface energy. When ratio is "-*e*", periodically major axis is decreasing while minor axis is increasing and the cross-section of the perturbed jet is an oscillating ellipse exchanging alternately its major and minor axes. For a given jet volume, a circular cylindrical shape results in the minimum lateral surface area and consequently provides the minimum surface energy. Increasing the ellipticity of a cylindrical jet increases the lateral surface area and jet surface energy. Due to the higher surface energy associated with elliptical jets, they disintegrate faster than circular jets. The results are in agreement with those of Caulk & Naghdi (1979) and experiments of Bechtel *et al*. (1995) and will be verified further in chapter 4 by an experimental analysis.

Cut-off wavenumber, defined as a value above which perturbations are stable, has been shown in figure 3.3 for various aspect ratios. Based on the above calculations, cut-off wavenumber is equal to,

$$K_c = \sqrt{\frac{-e(1+e)E_1 + 3e^2E_2 + 3e^3E_3}{eE_4 + E_5}} \tag{3.17}$$

where E coefficients are related to elliptic integral and have been defined in Appendix C. Only disturbances with wavelengths greater than $2\pi R/K_c$ destabilize the jet and lead to the jet breakup. R is the radius of a circle which has the same cross-sectional area as an ellipse. According to the Rayleigh theory, K_c is equal to one which means that for circular jet only disturbances with wavelengths greater than circle perimeter are unstable.

3.3.2 Spatial solution

The above mentioned temporal analyses was applied to an infinite jet, which considers the growth of the perturbation magnitude with time rather than along the jet axis, as is considered in

the spatial analyses for a semi-infinite jet. Jet profile can be derived from results of spatial linear analysis which allows prediction of axis-switching and breakup of elliptic liquid jets. To start spatial analysis, the following non-dimensional parameters are defined,

$$\tilde{z}=\frac{z}{R},\quad \tilde{t}=\frac{Vt}{R},\quad \tilde{v}=\frac{\bar{v}}{V},\quad \tilde{\delta}_1=\frac{\bar{\phi}_1}{a},\quad \tilde{\delta}_2=\frac{\bar{\phi}_2}{b} \tag{3.18}$$

For simplicity the tildas are dropped in the following notations. Substituting equation (3.12) into equations (3.6) and (3.7) and neglecting all the nonlinear terms of the disturbance quantities, the following dimensionless equation is derived,

$$(\delta_1+\delta_2)_t+(\delta_1+\delta_2)_z+v_z=0 \tag{3.19}$$

which serves as a continuity equation. Similarly, using equation (3.12) to linearize equation (3.8), and eliminating the pressure term, the dimensionless momentum equations along ϕ_1 and ϕ_2 directions can be expressed as follows,

$$\begin{aligned}
&(e(v_t+v_z)+\frac{1}{4}\delta_{1ztt}+\frac{1}{2}\delta_{1zzt}+\frac{1}{4}\delta_{1zzz})+\frac{1}{We}(d_1\delta_{1zzz}+d_2\delta_{1z}+d_3\delta_{2z}+d_4\delta_{2zzz})\\
&+\frac{1}{Re}(2e\delta_{1zt}+2e\delta_{1zz}-\frac{1}{4}\delta_{1zzzt}-\frac{1}{4}\delta_{1zzzz}-2ev_{zz})=0,\\
&(e(v_t+v_z)+\frac{e^2}{4}\delta_{2ztt}+\frac{e^2}{2}\delta_{2zzt}+\frac{e^2}{4}\delta_{2zzz})+\frac{1}{We}(d_5\delta_{2zzz}+d_6\delta_{2z}+d_7\delta_{1z}+d_8\delta_{1zzz})\\
&+\frac{1}{Re}(2e\delta_{2zt}+2e\delta_{2zz}-\frac{e^2}{4}\delta_{2zzzt}-\frac{e^2}{4}\delta_{2zzzz}-2ev_{zz})=0
\end{aligned} \tag{3.20}$$

where *We* and *Re* are Weber and Reynolds numbers defined as $We=\rho RV^2/\sigma$ and $Re=\rho VR/\mu$, respectively. Aspect ratio is presented by *e* and defined as the ratio of minor to major axes, i.e. *b*/*a*. Coefficients "*d*" are functions of the aspect ratio and arise from the linearization of the surface tension term in equation (3.9). They have been defined in Appendix E. In equation

(3.20), the first, second, and third parts, represent inertial, capillary, and viscous effects, respectively.

Based on the spatial instability analysis of Keller et al. (1973), the jet-nozzle problem requires that in a nozzle-fixed frame, one considers solutions of the form $\exp[i(\alpha t - kz)]$, keeping α real and allowing k to be complex. Then the real part of k will be associated with wavelength while its imaginary part will correspond to the growth or attenuation in the axial direction, depending on its sign. Using the linear stability of the jet on the basis of this approach, the unstable spatial dispersion relation will be obtained which predicts the wave growth rate versus frequency as a function of Weber number. By eliminating the pressure term in equations (3.19) and (3.20) and replacing the exponential spatial forms of δ_1 and δ_2, two new equations are obtained (similar to equation (3.14)) and their nontrivial solution results in the spatial dispersion equation. Alternatively, one can perform a transformation of $z = z + Vt$ in temporal dispersion equation (3.15), which is equal to replacing ω in temporal dispersion equation with $\sqrt{We}(\beta - K)$ to provide the following spatial dispersion equation,

$$\sum_{j=0}^{8} b_j K^j = 0. \tag{3.21}$$

Coefficients b_j are functions of Weber number and Strouhal number and have been defined in Appendix F. Strouhal number is defined as $\beta = -\alpha_i R / V$. K is dimensionless wavenumber and is defined as $K=kR$. Equation (3.21) gives all wavenumbers that closely approximate those obtained from the three-dimensional theory by Keller et al. (1973) in circular case. In general, equation (3.21) has eight roots, four of which are not acceptable due to the radiation condition (Bogy 1978b) which states that energy must be outgoing towards downstream ($z \rightarrow \infty$). The excluded roots are of order $O(2)$ and $O(3)$. Among the other four roots, two of them are conjugate

imaginary that lead to the breakup while the other two are real roots lead to the axis-switching. The Jet profile includes the superposition of these two modes.

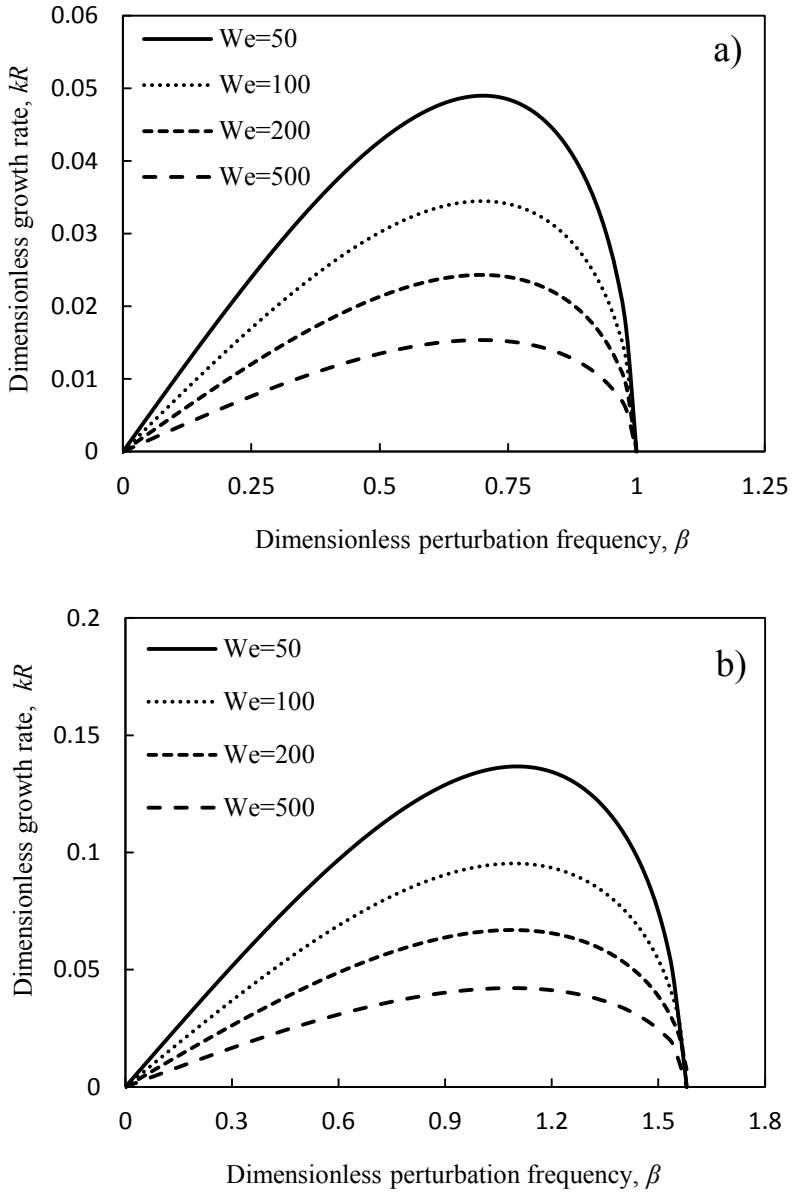

Figure 3.7: Dependence of dimensionless wavenumber *kR* on frequency *β* and Weber number *We* for semi-infinite inviscid jets with aspect ratios of (a) 1.0, and (b) 0.5.

Similar to the analysis of Keller et al. (1973), the root corresponding to the fundamental mode for which the imaginary part of k is negative, gives unstable disturbances for a jet with velocity in the z direction. Figures 3.7a and 3.7b show spatial growth rate for inviscid elliptic jets

with different aspect ratios under various jet velocities. Figures 3.8a and 3.8b show dependency of wavenumber to frequency for various *We* numbers in inviscid and viscous cases for a special case of *e*=0.7.

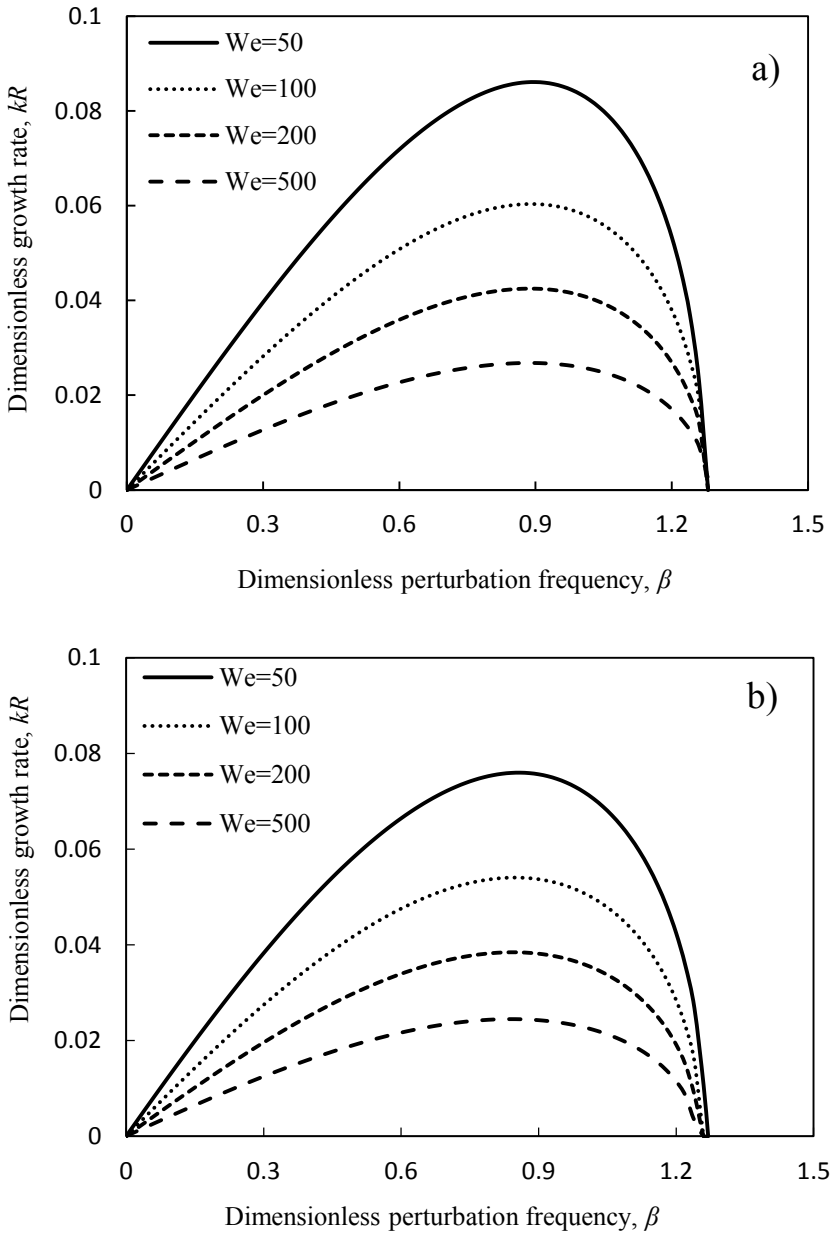

Figure 3.8: Dependence of dimensionless wavenumber *kR* on frequency *β* and Weber number *We* for semi-infinite elliptic jets with *e*=0.7, for (a) inviscid, and (b) viscous (*Oh*=0.15) cases.

As shown in the above results, by increasing the Weber number, instability growth rate is decreased; which is in agreement with the experimental results showing that by increasing the jet velocity, breakup length is increased. In the Rayleigh mode, viscosity always dampens perturbations and shifts the maximum growth rate toward longer waves.

Following Pimbley (1976) and Bogy (1978a, 1978b), the jet radius in the major and minor axes directions is written as,

$$\delta_1(z,t) = \sum_{j=1}^{4} D_j \exp i(\beta t - K_j z),$$
$$\delta_2(z,t) = \sum_{j=1}^{4} E_j \exp i(\beta t - K_j z) \tag{3.22}$$

where D_j and E_j are unknown coefficients that are determined using boundary conditions. K_j represents the relevant roots of the spatial dispersion equation (3.21). The following boundary conditions are valid,

$$\delta_1(0,t) = 0,\ \delta_2(0,t) = 0,\ v(0,t) = v_p \cos \beta t. \tag{3.23}$$

The first two boundary conditions are associated with the jet at the nozzle face and the last boundary condition represents the harmonic disturbance at the nozzle with dimensionless amplitude of v_p and dimensionless frequency of β. Solving the spatial equation requires one more boundary condition which is the jet slope $\delta_{1z}(0,t)$ defined at the nozzle face in the major axis view. Alternatively, the jet slope in the minor axis view could be selected, as the two are dependent on each other through the continuity equation. The jet slope at the nozzle face could be found by measurements (Bechtel et al. 1995).

The velocity modulation of the boundary conditions as presented in equation (3.23) can be generated by a piezoelectric transducer which contracts and expands periodically by applying a periodic voltage on it. The velocity modulation frequency is equal to the imposed frequency to piezoelectric transducer.

Based on equation (3.22), the following solutions are written for the dimensionless jet radius for the major and minor axes views,

$$\delta_1 = real\{([C_1(\exp(-iK_1z)-\exp(-iK_2z))]-[C_2(\exp(-iK_3z)-\exp(-iK_4z))])\exp(i\beta t)\},$$
$$\text{Unstable} \qquad \text{Stable} \tag{3.24}$$
$$\delta_2 = real\{([(1/e)C_1(\exp(-iK_1z)-\exp(-iK_2z))]+[C_2(\exp(-iK_3z)-\exp(-iK_4z))])\exp(i\beta t)\}.$$

It was shown in the temporal solution that the ratio of disturbances of the minor to major axes is equal to 1 for unstable roots and is equal to $-e$ for stable roots. Using the dimensionless forms in equation (3.18), these ratios for δ_2/δ_1 become $1/e$ and -1, respectively. These two coefficients appear in front of the unstable and stable parts in equation (3.24), respectively. Coefficients of C_1 and C_2 are found from boundary conditions in equation (3.23) as follows,

$$C_1 = \frac{v_p K_1 K_2}{\beta(1+1/e)(K_1-K_2)}, \tag{3.25}$$

and

$$C_2 = \frac{-i\delta_{1z}(0,t)}{(K_3-K_4)\exp(i\beta t)} - \frac{v_p K_1 K_2}{\beta(1+1/e)(K_3-K_4)}. \tag{3.26}$$

Based on the results of the temporal analysis, for asymmetric disturbances, the cross-section of the perturbed jet is an oscillating ellipse exchanging alternately its major and minor axes (See

figures 1.5 and 1.6). For unstable axisymmetric disturbances, the aspect ratio is approaching a value of unity, i.e. recovering a circular cross-section which has a smaller surface area (energy) for a given volume. The jet profile in equation (3.24) is composed of two parts; the first includes the imaginary roots which grow in space and lead to instability, and the second includes the real roots which are stable in space and lead to axis-switching phenomenon.

The spectrum of the roots K_1, K_2, K_3, and K_4 is required in order to determine their contribution to breakup and axis-switching. The real parts of K_1 and K_2 are equal to the imposed dimensionless frequency and the imaginary parts give the growth (positive root) and decaying (negative root) rates. Assuming K_1 is the root with positive imaginary part, it results in growing disturbances along the jet. Consequently, K_2 with negative imaginary part (as conjugate of K_1) represents the attenuating mode. K_3 and K_4 are real and contribute to the oscillatory modes which are stable along the jet axis. The variations of these four roots by Weber number, for an elliptic jet with aspect ratio of e= 0.5, are shown in figure 3.9. Although this figure has been plotted for an imposed frequency of unity, for any imposed frequency the trend of all roots will be similar. It is important to mention that only the real parts of roots K_1 and K_2 are plotted in this figure. The imaginary part of K_1 is in fact the growth rate which has been presented in figures 3.7 and 3.8. As expected, the real parts of K_1 and K_2 are equal to the imposed frequency except for very low *We* numbers due to the difference between spatial and temporal analysis results (Keller et al. 1973).

It is important to note that the first part of equation (3.24) which represents the dominant unstable mode, propagates at the frequency of the real part of K_1 (or K_2) which is equal to the excited frequency, ω. The breakup wave propagates with a phase velocity (i.e. wave speed) of ω/K_1 (or ω/K_2) which in dimensionless form is equal to one. In parallel, axis-switching mode is

propagated at the same phase velocity as the breakup mode which means that the axes of the jet are altered at a frequency equal to the imposed frequency (or natural frequency in free oscillations). However, it is better to calculate the group velocity (instead of monochromatic carrier waves) which is responsible for conveying breakup and axis-switching information. This task is out of the scope of the current work.

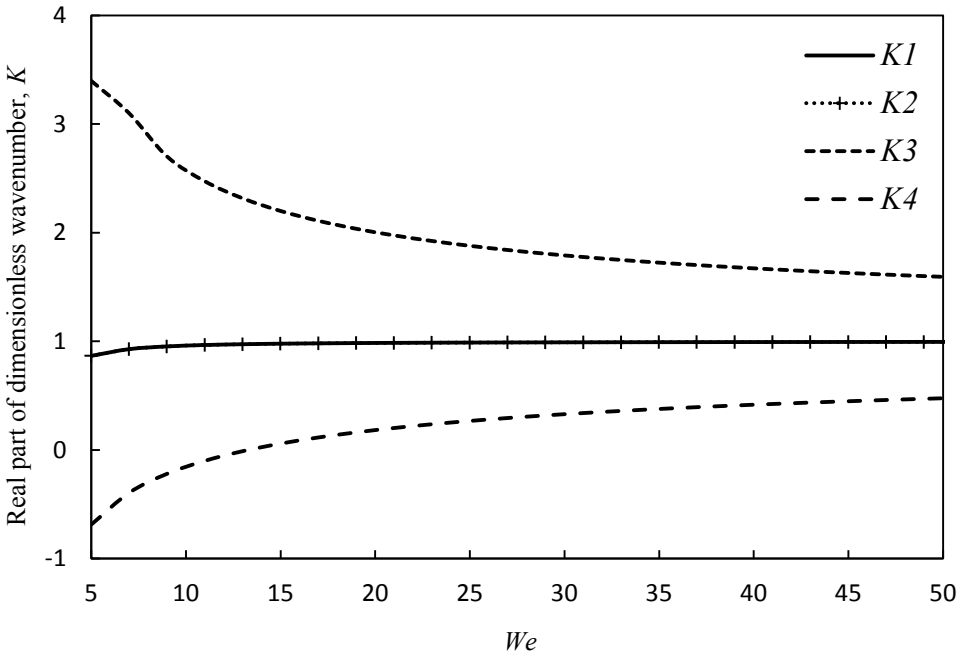

Figure 3.9: Variation of real parts of roots of spatial dispersion equation by Weber number for a specific perturbed frequency.

Based on the linear instability theory, breakup occurs when the amplitude of small perturbations grows and exceeds the radius of the undisturbed jet. Although such a large disturbance is not in the validity range of linear analysis, previous studies for circular jets (e.g. recently by Gonzalez & Garcia 2009) showed that the calculated breakup length is in good agreement with the experimental results. Using equation (3.24), spatial evolution of the circular and elliptic jets for specific values of fluid and perturbation parameters are shown in figure 3.10.

The breakup length (Z_b) can be computed from the jet profile where the jet radius becomes zero. This task will be performed in the next chapter and the predicted value will be compared with the corresponding breakup length measured from experiments. In general, small numbers of Fourier modes are not sufficient to give a correct representation of the shape evolution and non-linear behavior of the jet profile.

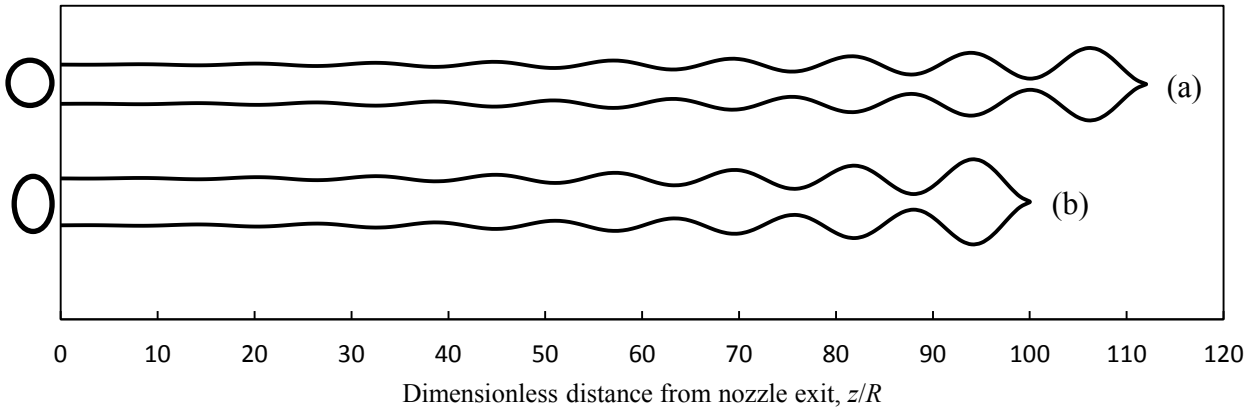

Figure 3.10: Jet radius as a function of distance from exit of (a) a circular nozzle and (b) an elliptic nozzle (major-axis view) (*We*=100, *Oh*=0.35, *e*=0.7, β= 0.525, v_p=0.01, δ_{1z} (0, *t*)=0.01).

The wavelength of axis-switching can be determined by a simple analysis. Using the linearized form of Cosserat equations in (3.14), it can be shown (Caulk & Naghdi 1979) that an elliptic jet with a small aspect ratio, oscillates at the dimensionless frequency of ω as,

$$\omega^2 = 2(3 + K^2) \tag{3.27}$$

where $\omega = \alpha \sqrt{\rho R^3 / \sigma}$ and $K = kR$. It is important to note that equation (3.27) has also been derived by Rayleigh (1879) through asymmetric stability analysis of circular jets. On the other hand, as shown in figure 3.9, for velocities larger than the capillary velocity, i.e. $We >> 1$,

$$K \approx \beta \tag{3.28}$$

and using the definition of dimensionless numbers, one may write,

$$\omega = \beta\sqrt{We}. \tag{3.29}$$

In conclusion, the dimensionless wavelength of axis-switching, λ_{as}, is given by,

$$\lambda_{as} = \frac{2\pi}{\sqrt{6}}\sqrt{We-2} \tag{3.30}$$

which means that the dimensionless axis-switching wavelength is proportional to $We^{0.5}$ by a factor of $2\pi/\sqrt{6}$.

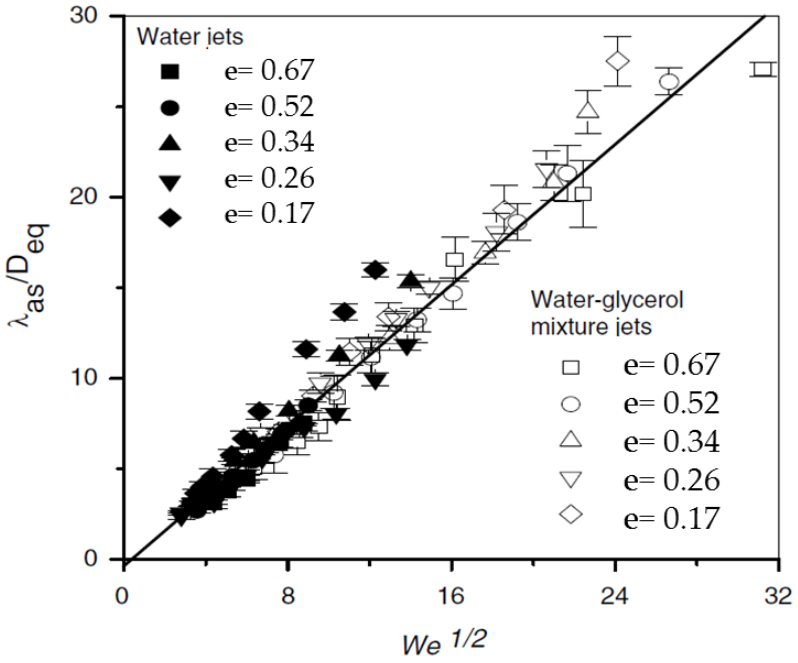

Figure 3.11: Variation of dimensionless axis-switching wavelength, λ_{as}/D_{eq} with $We^{0.5}$ for jets discharging from the elliptic orifices with different ellipticities. The solid line is the linear fit of the entire data. (From Kasyap et al. 2009).

Experiments of Kasyap et al. (2009) for an unforced elliptic jet showed that a straight line with a slope of 0.96 can be fitted to the measured dimensionless axis-switching wavelength versus $We^{0.5}$ (See figure 3.11). Considering the definition of Weber number and the dimensionless axis-switching wavelength in their work that is based on the equivalent jet

diameter ($2R$), according to equation (3.30) the slope of the line will be $\pi/\sqrt{12}$ or 0.9. This value is in good agreement with the measured value of 0.96 of Kasyap et al. (2009) where the jet is perturbed by its natural frequency. In fact, experimental results show that this slope is not a strong function of liquid jet ellipticity. It is important to note that according to equation (3.30), at small Weber numbers, the wavelength of axis-switching is of the same order as the jet diameter. This can be interpreted as invisibility of axis-switching at low Weber numbers as presented by Kasyap et al. (2009) and confirmed by our experiments.

Chapter 4

Experimental Analysis

This part includes the experimental work that has been performed to validate the linear analysis and also to investigate the nonlinearity effects along with the effects of the jet velocity profile. Both natural (free) and excited (forced) breakup behaviors are studied. In the natural instability case, breakup length of elliptic nozzles with different ellipticities and length to diameter ratios have been measured in a range of Weber numbers covering the Rayleigh regime. In the forced breakup case, the instability of liquid jets subject to sinusoidal perturbations is investigated. The curves of the breakup length versus the excitation frequency are plotted and examined against the theoretical dispersion curves derived in chapters 2 and 3. Results are compared with conventional circular nozzles which can be considered as a special case of an elliptic jet.

The present experimental results are interpreted based on a linear temporal analysis. Previous works revealed that although the linear theory cannot explain accurately some behavior of liquid streams such as satellite droplets, it is however useful in predicting other parameters such as breakup length. In addition, according to the results of Keller's spatial analysis (1973), the spatial and temporal approaches are equivalent if the jet velocity is greater than the capillary velocity (i.e. $We >> 1$). Therefore, the current experimental data are analyzed in the framework of temporal perturbation analysis.

The development of a liquid jet of unperturbed radius, R, with a velocity, V, in a quiescent atmosphere can be analyzed using linear methods as described below. It is assumed that the Fourier component of the perturbation with frequency, f, grows with a temporal rate of amplification, α, and a temporal wavenumber, k. For a monochromatic perturbation the radius of the jet, r, is given by,

$$r = R + \eta_0 e^{i(\alpha t - (2\pi f / V) z)} \tag{4.1}$$

where η_0 is the initial perturbation amplitude. Assuming that breakup occurs when the perturbation amplitude is equal to the unperturbed jet radius, the perturbation growth rate is written as,

$$\alpha_i = -\frac{V}{Z_b} \ln \frac{R}{\eta_0} \tag{4.2}$$

where Z_b is the breakup length. Under any particular experimental setup for jet velocity, disturbance amplitude and frequency, there is a specific minimum length for break up. This characteristic relates the growth rate of disturbances to the imposed frequency. Assuming that the initial disturbance amplitude of perturbations, η_0, is proportional to the applied voltage on the

liquid jet (Gonzalez & Garcia 2009, Kalaaji et al. 2003), equation (4.2) is written in the following form,

$$\alpha_i = V \frac{\Delta \ln U}{\Delta Z_b} \tag{4.3}$$

where U is the amplitude of the imposed voltage to the liquid jet (e.g. through a piezoelectric actuator). Delta indicates the difference between quantities in log of voltage ($\Delta \ln U$) and breakup length (ΔZ_b). In addition, dimensionless wavenumber, $K=kR$, is calculated from measurements of imposed frequency , f, and mean jet velocity, V, from relation,

$$K = \frac{2\pi Rf}{V}. \tag{4.4}$$

Equation (4.3) can be used to determine the experimental dispersion curve $\alpha(k)$ and compare it to the corresponding theoretical dispersion equations. This method was used before by Bruce (1976), Cline & Anthony (1978), Kalaaji et al. (2003), and Gonzalez & Garcia (2009). Similar to these works, the present approach is based on controlling the frequency and fixing the initial perturbation amplitude using piezoelectric transducers with a given pure sinusoidal disturbance. Chaudhary & Maxworthy (1980) used an alternative method consists in using a fixed frequency and a variable velocity. It is important to note that instead of imposing disturbances in terms of velocity modulation (e.g. by a piezoelectric actuator), one can produce and impose disturbances in the jet radius (e.g. by shielding electrodes). For a circular jet, results of Gonzalez & Garcia (2009) from two methods were the same and in excellent agreement with the linear instability analysis. Generally, disturbances also can be in the form of fluctuations in liquid properties such as viscosity, temperature, or surface tension coefficient.

4.1 Experimental setup

The experimental setup is schematically shown in figure 4.1. The experiments were performed in two different sections. In the first part, breakup of a liquid jet is studied under natural disturbances; and in the second part, external disturbances are imposed on the jet. In the second part, the disturbances are applied by a piezoelectric transducer in the form of a velocity modulation over the mean velocity field. A sinusoidal wave is formed by a function generator and is amplified with an amplifier which is fed to the piezoelectric actuator. The piezoelectric transducer contracts and expands periodically by applying a periodic voltage on it and produces pressure oscillations in the nozzle chamber which translates into sinusoidal disturbances of the jet velocity at the nozzle exit. Figure 4.2 shows the injector assembly including the piezoelectric actuator.

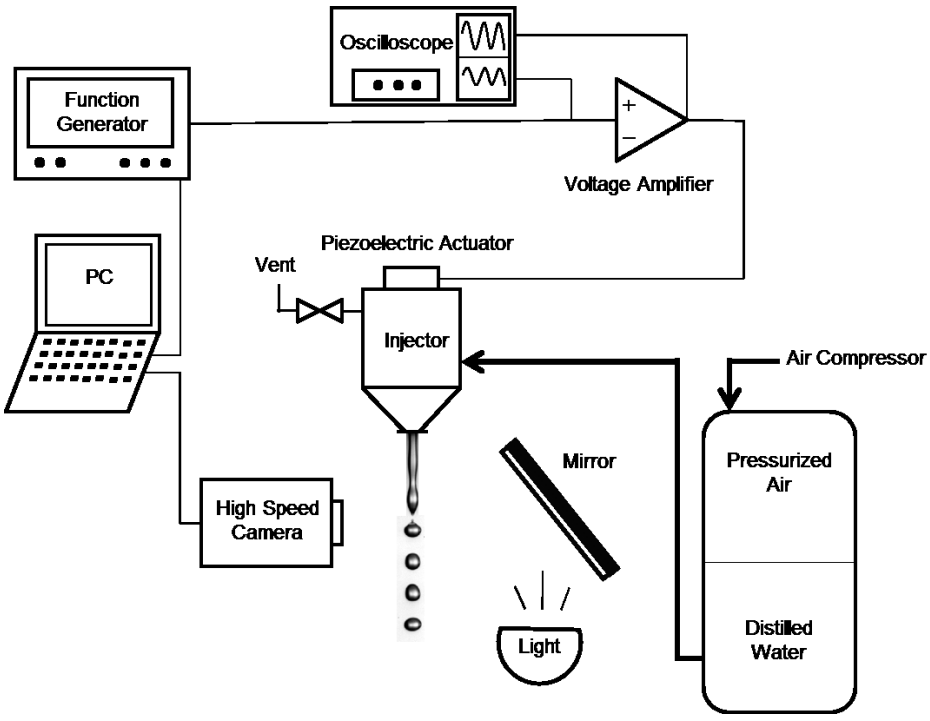

Figure 4.1: The schematic of experimental setup.

Low voltage values (less than 70 volts, peak-to-peak) were used to obtain results comparable with the linear stability analysis. High voltage values impose large perturbation amplitudes which create nonlinearity and are not covered in the mentioned theoretical analyses. It was assumed that the same disturbance applied to the actuator is transferred directly to the liquid jet and the effects of the actuator dynamics that may cause nonuniformities were ignored. The obtained data provides information about difference nozzle geometries which is the goal of this work.

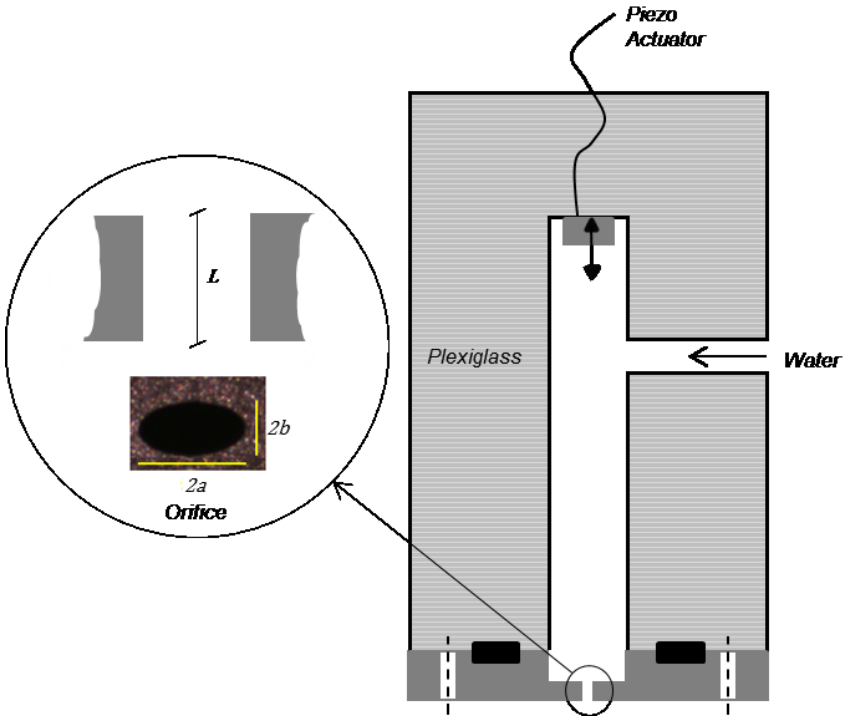

Figure 4.2: The injector assembly.

Fifteen elliptic nozzles with equal cross-sectional areas and different ellipticities and lengths were manufactured and tested. Details of geometry specification of the nozzles are listed in table 4.1. The orifices were fabricated from Aluminum by a wire-cut electrodischarge machining process. Due to the machining process, there were differences in the nozzles' cross-sectional area

Nozzle ID.	2*a* (mm)	2*b* (mm)	*b/a* *(e)*	2*R* (mm)	*L*/(2*R*)
#1	0.47	0.47	1.00	0.470	10
#2	0.46	0.47	0.98	0.465	5
#3	0.46	0.46	1.00	0.460	1
#4	0.58	0.39	0.67	0.475	10
#5	0.59	0.40	0.67	0.485	5
#6	0.60	0.42	0.70	0.502	1
#7	0.68	0.32	0.47	0.466	10
#8	0.69	0.35	0.51	0.491	5
#9	0.68	0.35	0.51	0.465	1
#10	0.80	0.28	0.35	0.487	10
#11	0.82	0.28	0.34	0.480	5
#12	0.80	0.27	0.33	0.464	1
#13	0.94	0.24	0.25	0.475	10
#14	0.93	0.25	0.27	0.482	5
#15	0.92	0.22	0.24	0.450	1

Table 4.1: Geometrical specification of the nozzles.

and the error is within 5% of the nominal equivalent diameter. Weber and Reynolds numbers were maintained equal for all nozzles by using an equivalent diameter of 475 μm and the same liquid flow rate; this allows comparison of the behavior of different nozzles. Five different aspect ratios were examined; 0.25, 0.33, 0.5, 0.7, and 1. An aspect ratio of one belongs to a circular nozzle which was used for comparison with other elliptic nozzles. Three different values of length to diameter ratio (i.e. *L/D*) were used; 1, 5, and 10. In the forced breakup experiments, only the nozzles with length to diameter ratio of one were examined. The reason for this selection is to minimize the velocity relaxation effects since the current theoretical models

assume that the velocity profile is uniform over the cross-section (i.e. plug flow). It is important to note that even for short nozzles due to the relaxation of the velocity profile there is a small difference between the nominal nozzle radius and the unperturbed jet radius which was ignored in the present work.

Water was supplied from a pressurized tank to supply liquid at a desired pressure. Distilled water was used for experiment which has a density of 997 kg/m^3, a surface tension of 0.073 N/m, and a viscosity of 0.0009 $kg/m.s$. The liquid flow to the nozzle is controlled by a pressure regulator along with a flow control valve. Although a water filter was mounted before the flow control valve, nozzles were blocked during the experiments and had to be cleaned regularly. In addition, a vent valve was provided just before the injector inlet to remove bubbles if any occurred. The velocity value was obtained from the volumetric flow rate and exit area of the nozzle. The injection assembly was mounted on an optic table with self-leveling supports for vibration isolation.

A diffused backlight system with adjustable intensity was used to illuminate the jet. The behavior of the elliptic jets was visualized using high speed photography. Depending on the jet velocity, nozzle geometry, and the imposed frequency, the resolution was adjusted, and up to 20,000 frames per second images were captured. In order to obtain perpendicular images of the major and minor axes simultaneously, a mirror was used. The image of the major axis direction was a direct view but that of the minor axis reflected off the mirror. Experiments were repeated four times for each run for a range of Weber number varying between 5 and 400, and Reynolds number of 500 to 5000. As mentioned before, the jet equivalent radius (R) is used as the characteristic length to calculate Weber and Reynolds numbers.

4.2 Results and discussion

Figure 4.3 presents the breakup of liquid jets that emerged naturally from nozzles with different aspect ratios. It is clear that by reducing the ratio of the minor to major axes, the breakup length is decreased. In the free breakup regime, i.e. where there is no excitation force, it is assumed that the jet is disturbed by the natural frequency of the nozzle system and there is a maximum wave growth rate α_{max}, which occurs at a wavelength of λ_{max}. The maximum wave growth rate and the corresponding wavelength characterize the fastest growing (or the most probable) waves on the liquid surface that are eventually responsible for the breakup.

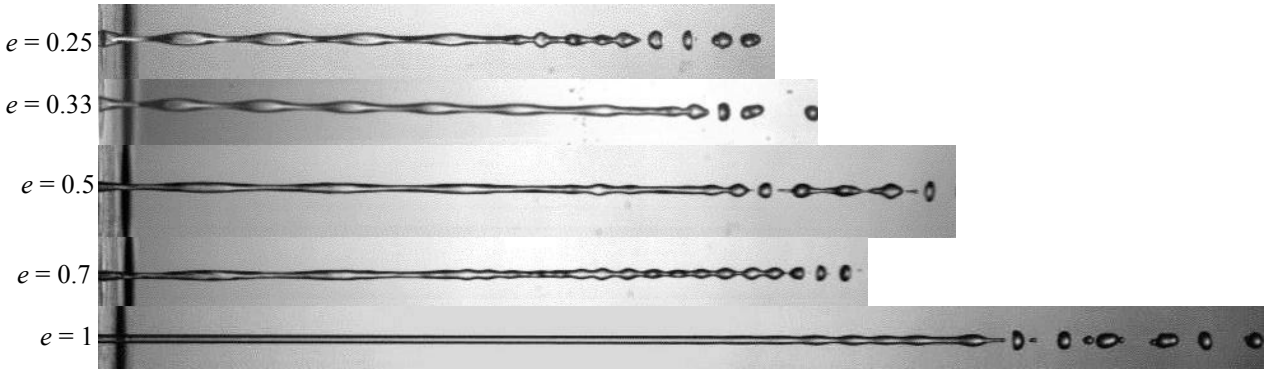

Figure 4.3: Images from major axis view of nozzles issuing water jets (*We*= 35, *Re*=1400).

Figure 4.4 shows the variations in the breakup length for different geometries and jet velocities under natural perturbations. Z_b is the breakup length which is made dimensionless using the jet equivalent diameter, D=2R. The horizontal axis is $\sqrt{We}$ which is proportional to the jet velocity. In figure 4.4 the shortest nozzles, i.e. L/D of one, were used to minimize the effect of velocity relaxation. In agreement with the results of Kasyap et al. (2009), figure 4.4 shows that breakup length of elliptic liquid jets is much smaller than that of equivalent circular jets. Furthermore, by increasing the ellipticity, the breakup length becomes shorter.

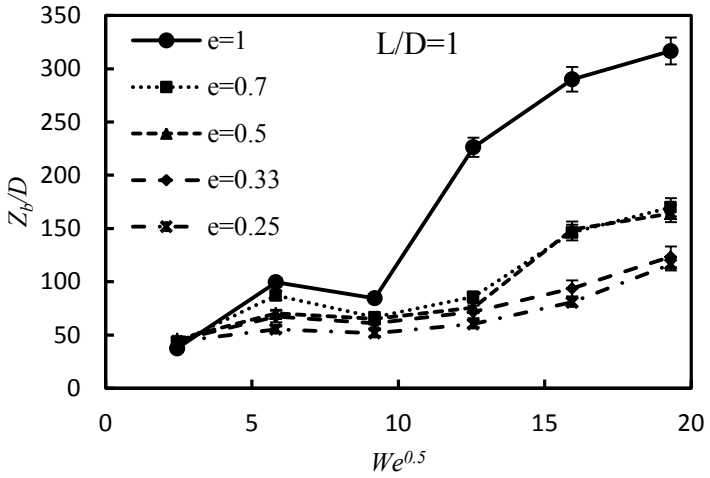

Figure 4.4: Dimensionless breakup length versus dimensionless jet velocity for different elliptic nozzles with the exit area.

One of the main geometrical parameters in circular nozzles is the length to diameter ratio (McCarthy and Molloy 1974, Birouk and Lekic 2009). By influencing the velocity profile and boundary layer thickness, this parameter contributes to the jet surface instability and breakup length. Exiting the long nozzles, liquid jet exercises relaxation of parabolic to flat profile. This process redistributes the jet's energy and creates a destabilizing force (McCarthy and Malloy 1974). However, linear instability analysis of Leib and Goldstein (1986) and Ibrahim and Marshall (2000) revealed that non-uniformity in the velocity profile (e.g., parabolic) would lead to a reduced instability. On the other hand, the source of the generation of turbulence within short tubes is usually more limited than in the longer tubes (e.g. by friction force). Therefore, jets with the more uniform velocity profile would require a higher Reynolds number than the longer tubes before they contain turbulent disturbances that are sufficient to promote the jet breakup (Delber and Yu 1988). It is important to note that turbulent flow profiles are significantly similar to the uniform profiles and thus are only slightly susceptible to velocity relaxation effects. As

the present theoretical model does not consider nonuniform jet profiles, investigating the effect of nozzle length and velocity profile is required.

Figure 4.5 presents the effect of length to diameter ratio on elliptic nozzles with different aspect ratios. For Weber numbers less than 100, which corresponds to the Reynolds number of 2400, the influence of the length to diameter ratio on the breakup length shows no clear trend. This can be explained by the dual effects of velocity profile. A perturbation begins to grow internally at a large rate for a fully developed laminar flow which needs a distance for velocity profile relaxation. On the other hand, for plug flow conditions, the perturbations which are imposed upstream will be small at the exit, but will grow at a larger rate. Additionally, the geometry of the current injection may create turbulence in the long tubes even at We numbers less than 100. As shown in figure 4.5, for Weber numbers greater than 100, the short tube produces jets which are markedly more stable than those produced from longer tubes. These results indicate that in this range of jet velocities, the main cause for the shorter jet lengths is the interactions with the turbulence that is generated within the longer tubes. Moreover, results reveal that the effect of nozzle's ellipticity is more significant than its length. As shown in figure 4.5, for the whole range of Weber numbers, by increasing the ellipticity, breakup curves for different length to diameter ratios collapse to each other.

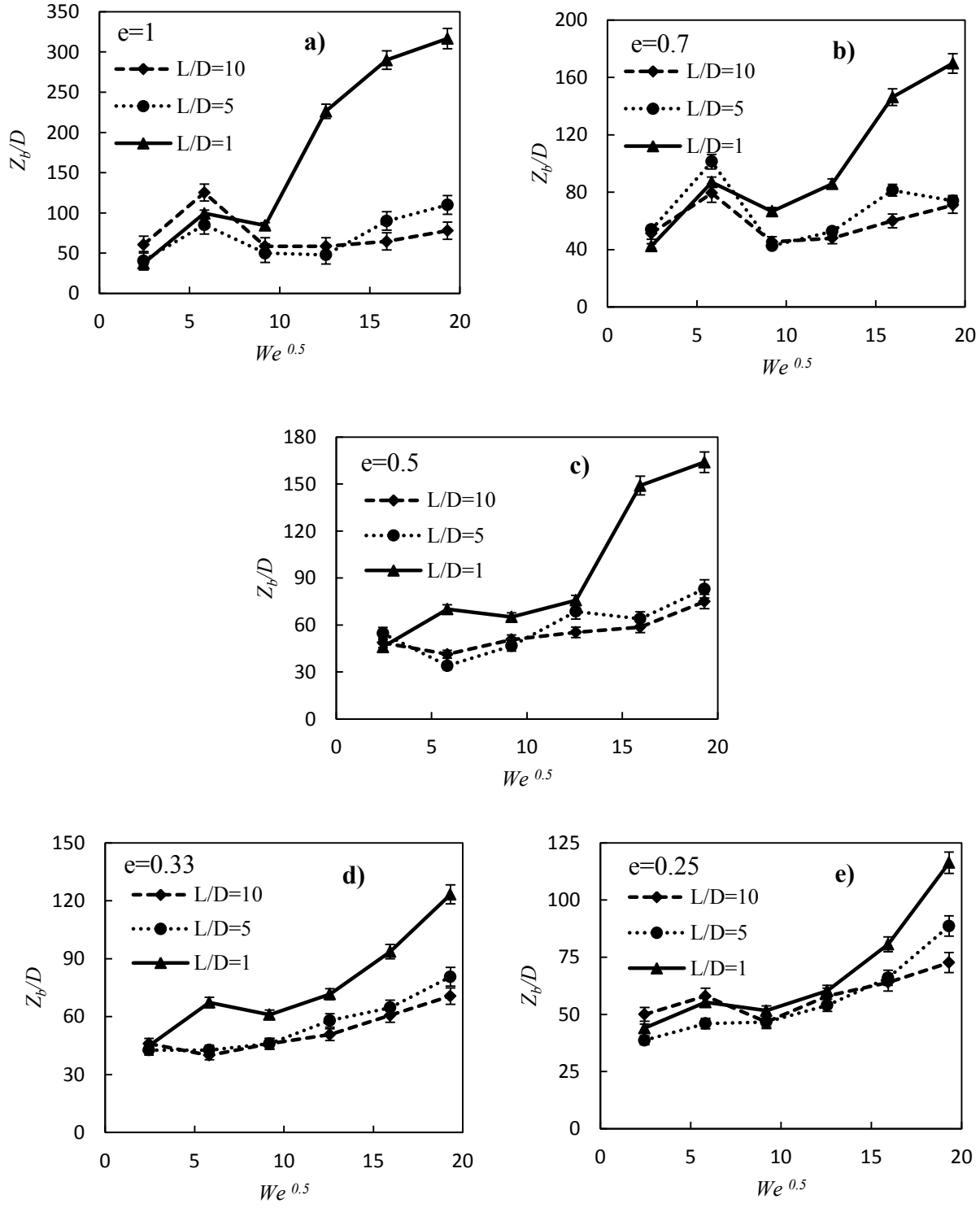

Figure 4.5: Effect of *L/D* (length to diameter ratio) and *e* (minor to major axis ratio) on breakup length of liquid jets.

Referring to equation (4.3), the disturbance growth rate can be calculated using the breakup length and the amplitude of the imposed voltage. Figure 4.6 shows the variation of the breakup length for a sample case of e=0.7 and three different dimensionless wavenumbers; 0.51, 0.71, and 1.16. For each measurement, the velocity was fixed and the frequency was varied so that the dimensionless wavenumber can be calculated from equation (4.4).

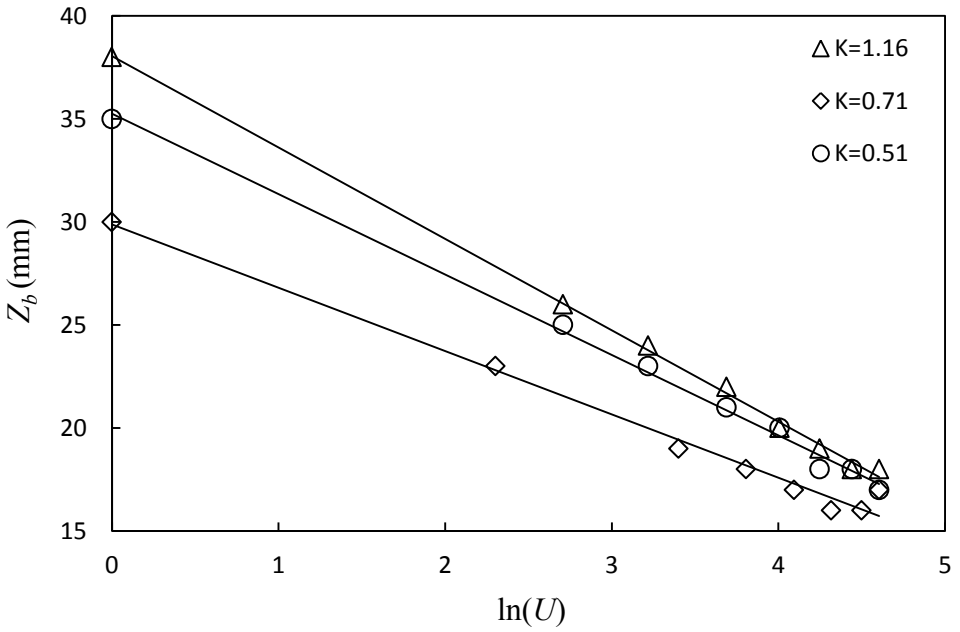

Figure 4.6: Breakup length versus log of amplitude of the applied voltage for aspect ratio of e=0.7. The solid lines are least-squares fit of the data.

By calculating the slope of the line of the breakup length versus the imposed voltage, the growth rate was found for a wide range of wavenumbers (figure 4.7). Using definition of dimensionless wavenumber by equation (4.4), a combination of frequency and velocity variation was used to cover the unstable range of K. The moderate velocity range (i.e. $30<We<100$) of experimental results was used because the mentioned quasi-one-dimensional theoretical model covers the Rayleigh mode only and not the dripping or wind-induced regimes. Gravity force in

the dripping regime, and the aerodynamic interactions with air in the wind-induced regimes, assist the capillary force in disintegrating the liquid jet.

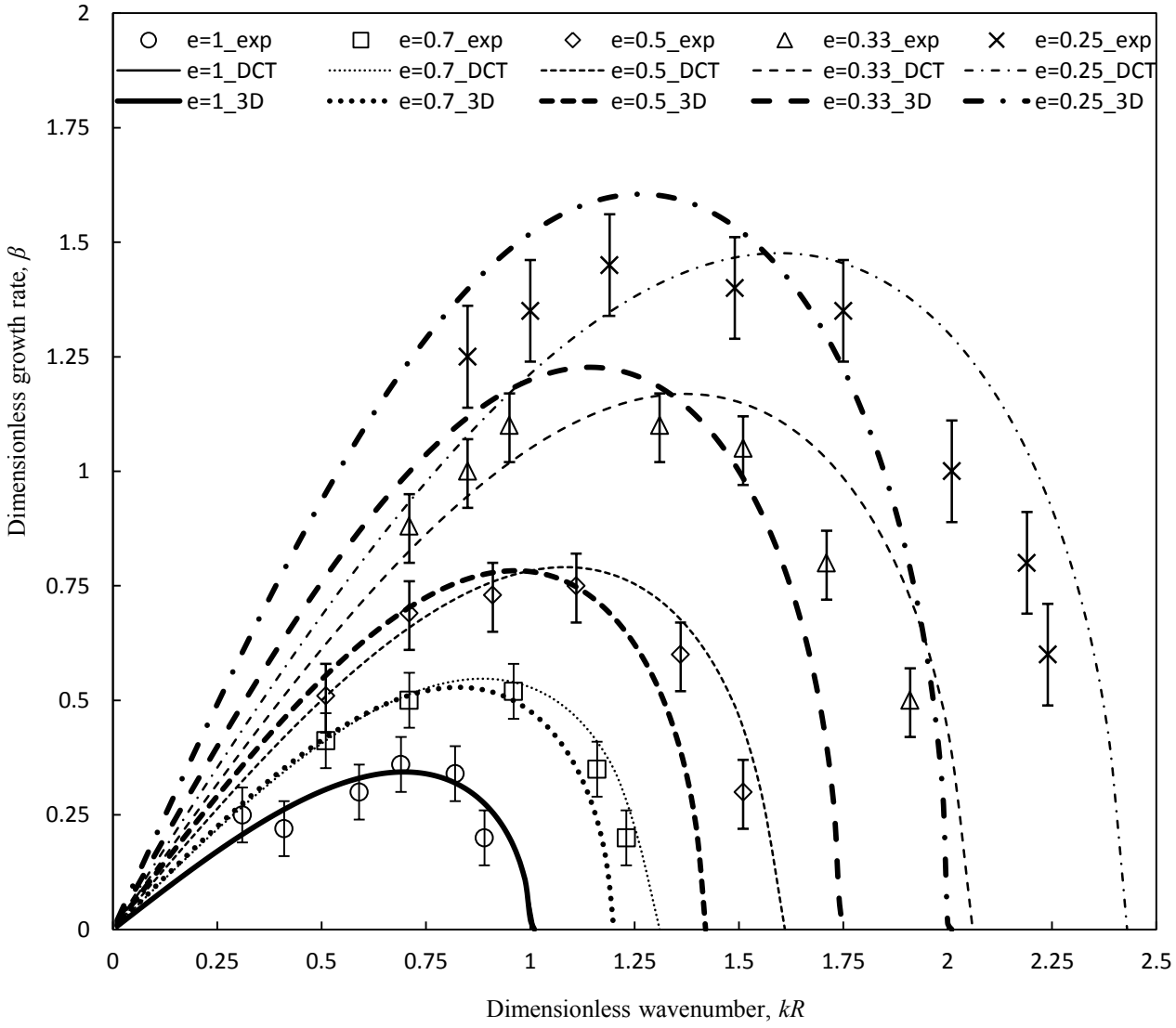

Figure 4.7: Comparison of temporal growth rate between results of 3-D, DCT (Directed Curve Theory) and experimental analyses.

Figure 4.7 depicts the variation of the instability growth rate versus imposed frequency for different elliptic jets. The dimensionless disturbance growth rate is defined as, $\omega = -\alpha_i \sqrt{\rho R^3 / \sigma}$ which varies by the dimensionless excitation wavenumber defined as, $K = kR$. As mentioned

previously, R is the radius of an equivalent area circle, and e is the aspect ratio, i.e. the ratio of minor to major axes. To compare the measurements with the theoretical predictions, results of the dispersion curves from 3-D linear analysis and directed curve (Cosserat) theory are also presented in this figure.

As shown in figure 4.7, by increasing the ellipticity (i.e. by decreasing e), the instability grows faster and the range of unstable wavenumbers increases. In addition, the peak of the curves shifts to higher frequencies, i.e. shorter disturbance waves. For aspect ratios close to one, the results of the 3-D and DCT models are in good agreement with each other and also with the experimental results. Similarly, excellent agreements were found before between the DCT results and those of Rayleigh (1879) and Weber (1931) for inviscid and viscous circular jets, respectively (See figure 3.4). Clearly, for an aspect ratio of one, results of 3-D analysis reduces to that of Rayleigh. In addition, figure 4.7 shows that, DCT predicts a smaller growth rate and a wider instability range than 3-D model. The reason for a different growth rate could be in the calculation of curvature which enters the capillary force calculation as the main source of instability; in 3-D analysis, the maximum value of curvature was used (equation (2.74)), whereas in directed curve theory, curvature was averaged over the jet cross-section (equation (3.9)).

However, results show that the disturbance growth rate of high ellipticity jets obtained from the 3-D and DCT models, deviate from the corresponding measured values. It is important to note that nonlinear effects are strong at locations of the surface that are close to the jet axis (Gertsenshtein & Shkadov 1973) which is the case for jets with high ellipticity. For disturbances with KR close to zero and cut-off zones, natural (background) noise is a source of error for the breakup length and yields non-accurate growth rate calculations. It is generally believed that for frequencies lower than a specific threshold or higher than the cut-off value, the breakup is

random and not periodical. These results could be due to nonlinear effects that become dominant in this range of frequencies (Kalaaji et al. 2003, Rohani et al. 2010,).

Figure 4.8 which has been adapted from Kasyap et al. (2009) shows unstable mode through major and minor axes views of water jets discharging from an elliptic orifice at different Weber numbers. Based on the notations in chapter 2, this mode is Ce_1 which shows that the flapping mode is observable only in the plane of major axis; in agreement with the previous results that growth rate of Ce_1 is larger than Se_1 in higher ellipticities (chapter 2). At high ellipticities, "the elliptical jet effectively behaves like a thin sheet whose plane is perpendicular to the major axis plane of the elliptical orifice. This liquid sheet then tends to develop transverse waves similar to waves seen on plane liquid sheets." (Kasyap et al. 2009).

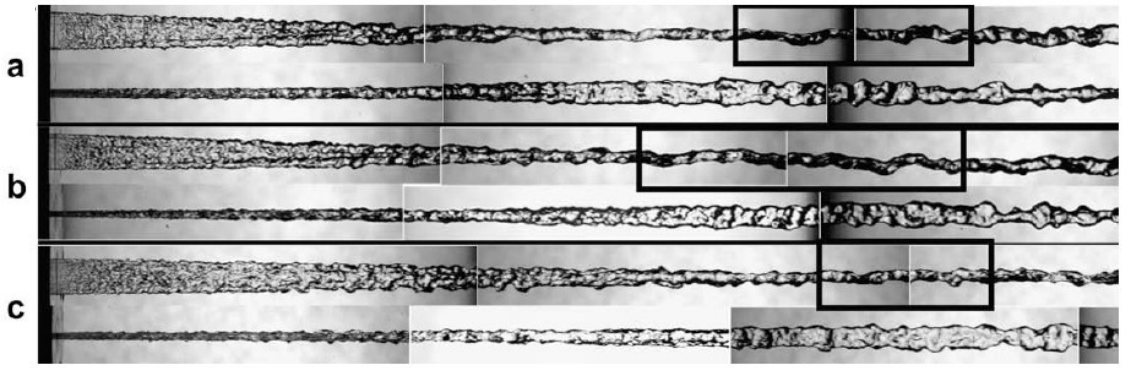

Figure 4.8: Images of water jets discharging from an elliptical orifice with e=0.17 at a) We=1655, b) We=2150, and c) We=3225 . Transverse waves are observed only in the major axis plane images (From Kasyap et al. 2009).

Chapter 5

Closure

The breakup of a liquid jet discharging from an orifice is a classical problem in fluid dynamics due to its theoretical and practical importance. A well-known practical application of the process of jet breakup is spray and droplet formation, which is of major interest to the combustion procedure of liquid-fuelled engines. In addition, this process is used in several other applications such as ink-jet printers, coating, medical tools, food preparation, and agricultural systems. The breakup of a liquid into spray increases the surface area of the liquid which subsequently increases the heat and mass transfer between the liquid and gas phases. The complexity of the breakup is related to the unusually large number of parameters involved namely the design of the nozzle, cavitation, turbulence, and the thermodynamic states of both liquid and gas. The different combinations of liquid inertia, viscosity, surface tension, and aerodynamic forces acting on the jet govern the main breakup regimes.

Among the above mentioned parameters, the role of the nozzle geometry on the jet breakup has been overlooked in the literature. Studies on liquid jets issuing from asymmetric nozzles have not been completely neglected but have certainly been very scarce. The reason could be greater mathematical difficulty encountered during the analysis specifically if analytical methods are used. Interest in the study of asymmetric jets arises, in particular, from the fact that jets issuing from these orifices may break up considerably earlier than symmetric jets. Among possible asymmetric shapes, the elliptic orifices have been examined the most. This is mainly due to the advantage provided by elliptic jets over circular jets in terms of rapid mixing and spreading when discharging into another fluid which is useful in applications such as combustion and irrigation systems. Geometrically, elliptic jets can be considered as an intermediate case between two simple configurations, the circular jets and the planar sheets, which have been studied extensively.

In this thesis, the motion of liquid jets issued from elliptic orifices was investigated using a combination of theoretical and experimental methods. Three main approaches were employed; a three-dimensional linear analysis for inviscid jets, the quasi-one-dimensional Cosserat theory for viscous jets, and experimental analysis. In the theoretical parts, a perturbation-based approach was used to investigate the governing equations for wave propagation on the jet surface. In the experimental part, measurements were taken to validate the linear results and also to investigate the effect of some parameters which were not covered by the theoretical analysis such as jet profile. The effect of the liquid viscosity, jet profile, and the aerodynamic forces were considered in the Cosserat theory, experimental analysis, and 3-D analysis, respectively. The methodology and results of these three approaches are summarized in the subsequent sections.

5.1 Summary and conclusion

The solution of viscous free-surface flow for an elliptic jet is complicated if 3-D analytical solutions are to be obtained. In chapter 3, the viscous free surface flow was studied using an approach based on the Cosserat theory (also called director theory). This model which inherently contains the radial inertia effects in its equations, gives the jet profile as a function of axial coordinate only and simplifies the analysis considerably. The quasi-one-dimensional Cosserat equations can be assumed as a low order form of the Navier-Stokes equations for slender jets. This model considers only long wavelengths disturbances whereas the case of short wavelength which occurs when aerodynamic forces become important is not covered. In addition, using this model, only uniform flow can be studied and the effect of the jet velocity profile cannot be captured. The Cosserat equations which were used here were derived originally by Caulk and Naghdi (1977, 1979) for liquid jets emerging from a nozzle with an elliptic cross-section. The governing equations are high order nonlinear partial differential equations (PDE) that are used to determine the position of the free surface.

Using perturbation methods, the linearized form of the quasi-one-dimensional directed curve equations was employed to study the wave propagation in viscous elliptic liquid jets. Temporal and spatial analyses were performed and the associated dispersion equations of waves on the jet column were derived to show the variation in the disturbance growth rate under various conditions. The liquid jet instability was studied for various ellipticities over a specific range of jet viscosity, velocity, and excitation frequency. Results were compared with the conventional circular nozzle which can be considered as a special case of an elliptic jet. Based on the spatial analysis results, an equation for the jet profile was suggested that describes the axis-switching phenomenon and breakup for various conditions as a function of time and axial space. The jet

profile has two parts; the first part grows in space and is associated with the jet breakup, whereas the second part is oscillatory and is associated with the axis-switching. The wavelength of axis-switching was predicted and was shown to be in good agreement with the experimental measurements of Kasyap et al. (2009).

The results revealed that in comparison with a circular jet in the capillary mode, the elliptic jet is more unstable and by increasing the ellipticity, the instability grows faster, while the range of unstable wavenumbers is increased. This excess of instability was attributed to a larger curvature in elliptic cylindrical jets which creates a larger surface tension force, the main source of instability in low-speed jets. For a given volume, the elliptic cylindrical jet has more surface area (and energy) than a circular cylindrical jet and tends to disintegrate faster. Similar to the circular case, the effect of viscosity is diminishing the growth rate and shifting the maximum growth rate to longer waves. In low-speed cases, the elliptic jet is unstable only when disturbances are symmetric, i.e. equal in the major and minor axes directions. These symmetric disturbances growing with time increase the initial aspect ratio of the ellipse toward unity corresponding to a circular cross-section with less surface energy. The jet is stable in asymmetric cases including the axis-switching mode where the aspect ratio reaches values greater than one. Similar to the circular jet, the asymmetric modes can grow only at higher Weber numbers, where aerodynamic forces cannot be ignored.

Considering the circumference of an elliptic jet cross-section, the curvature is maximum in the major axis and minimum in the minor axis directions and therefore, due to the Young-Laplace law, the local pressure in the major axis side is greater than that of the minor axis. As a result, the liquid flows from the major axis side toward the minor axis side. This motion changes the cross-section of the jet to another elliptic shape in which the location of major and minor

axes are changed, i.e. the axes are switched. These oscillations either continue after breakup (See figure 1.6) or damped by viscosity effects before breakup (Bechtel 1989).

The dispersion curve of an elliptic jet (e.g. figure 3.3) is similar to that of a circular jet with a smaller cross-sectional area. As confirmed in chapter 2, the capillary behavior of an elliptic jet is similar to that of a circle with a radius equal to its semi-minor axis (See figure 5.1). In other words, a circular core region inside the elliptic jet is responsible for the instability and breakup of the elliptic jet while the rest of the cross-section (two peaks in the circumference) is just oscillating and changes the location of major and minor axes, alternatively. It is important to mention that this discussion is valid only for small Weber numbers where aerodynamic forces are insignificant.

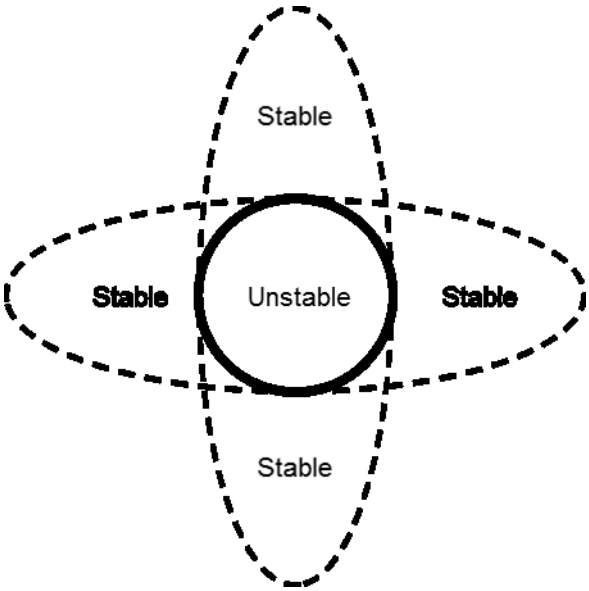

Figure 5.1: Axis-switching (stable) and breakup (unstable) regions of an elliptic liquid jet.

An experimental analysis was conducted to validate the linear analysis results and investigate the nonlinearity effects along with the effects of the jet velocity profile. Several nozzles with different ellipticities and lengths were designed and their behaviors were examined under free

(natural) and excited (forced) perturbations. Circular nozzles were analyzed as well to compare their behavior with that of elliptic nozzles. The evolution of the jet shape, axis-switching, and breakup was captured using a high speed camera. In the natural instability case, the breakup length of elliptic nozzles with different ellipticities and length to diameter ratios were measured for a range of Weber numbers covering the Rayleigh regime. In the forced breakup case, stimulations were performed by modulating the jet velocity with given sinusoidal perturbations using a piezoelectric actuator. Through the measurements of the jet breakup length and imposed frequency, the experimental dispersion curves were obtained and compared with the corresponding dispersion curves derived from the three-dimensional and quasi-one-dimensional Cosserat approaches.

It was observed that in the capillary mode, the breakup length of elliptic jets is much smaller than that of circular jets. In addition, jets with higher ellipticity have a shorter breakup length. Experimental results were in good agreement with linear analysis results which predicted that by increasing the ellipticity the instability grows faster and the range of unstable wavenumbers increases. Finally the effect of the jet velocity profile was studied by varying the nozzle's length to diameter ratio. Similar to the circular jets, and in agreement with the literature, there is not a clear trend for low-speed jets while at higher velocities longer nozzles produce jets with a shorter contact length. The measured data for instability growth rate were in good agreement with the theoretical predictions except at high ellipticities where nonlinear effects are strong.

In chapter two, using a three-dimensional analysis and including the effect of the surrounding gas, the linear evolution of initially small disturbances on the inviscid jets was investigated. An elliptical cylindrical column of liquid was considered and its response to a small perturbation to the shape of cross-section was modeled. The potential flow equation was solved in the elliptical

cylindrical coordinates and two boundary conditions were applied; the continuity of the radial velocity and the balance of normal stress on the free surface. The solution of the potential flow yielded a well-known Mathieu function. In case of equality between major and minor axes, the Mathieu function degenerates to a single Bessel function corresponding to a circular cylindrical case. The resulting system of equations admits a nontrivial solution, through which an explicit dispersion equation was derived. The growth of different azimuthal waves on an inviscid liquid jet was considered for a wide range of jet velocities. For various jet ellipticities, the growth rate of the symmetric and antisymmetric waves was plotted and compared with that of the circular jet. The well-known dispersion equations of circular and planar jets were recovered from the asymptotic solutions of the elliptic jet for extreme cases of small and large ellipticities, respectively.

It was shown that in the capillary dominant regimes, the growth rate and range of instability increase with increasing ellipticity due to the increasing surface area (energy). Modal analysis showed that in this regime only axisymmetric modes, i.e. the modes symmetric to both major and minor axes, can grow. As the jet velocity increases, i.e. for higher Weber numbers where capillary force stabilizes the disturbances, with increasing the ellipticity, the growth rate of disturbances decreases. For such Weber numbers, other azimuthal modes appear, while the axisymmetric mode still possesses the maximum growth rate. In some cases, the preferred mode switches from one that is symmetric with respect to both axes to one that is symmetric with respect to the major axis only. In general, for an inviscid elliptic liquid jet ejected into an inviscid gas, the growth rates of modes symmetric with respect to the major axis are larger than those antisymmetric with respect to major axis. This means that the preferred mode of the jet's motion is flapping in the plane of the major axis rather than flapping in the minor axis plane.

Similar to the circular jets, for elliptic jets in low-speed mode where long wave disturbances cause instability, increasing the Weber number decreases the instability growth rate. On the other hand, in high-speed modes, where short wave disturbances are responsible for the jet breakup, the instability increases with increasing the Weber number. The effect of increasing the ratio of gas to liquid density was found very significant. The higher the density ratio, the larger the instability growth rate and the wider the region where instability occurs. In addition, increasing the density ratio shifts the maximum growth rate toward shorter waves.

In effect, the curvature distribution of an elliptic jet is non-uniform whereas the curvature distribution of a circular jet is uniform and that of a planar sheet is zero. Therefore, the behavior of an elliptic jet is different than that of a circular jet or a planar sheet. This difference is visible only for low-speed regimes where drops are pinched off the liquid jet due to capillary instability. By increasing the jet velocity or ratio of gas to liquid density, the aerodynamic forces become dominant. In this case, the short wave disturbances (much smaller than the jet's radius of curvature) prevail and the disintegration occurs on the jet surface. Therefore, the curvature of the three configurations become ineffective and the above mentioned difference vanishes.

In general, the behavior of elliptic jets, even for high ellipticities, is more similar to that of the circular jets than that of the liquid sheets. The difference between elliptic and circular jets is more significant in surface tension dominant regimes. In Rayleigh and first wind-induced regimes where the capillary force is destabilizing, elliptic jets are more unstable than circular jets. At higher Weber numbers, where capillary force is stabilizing, circular jets are more unstable than elliptic jets. However, neither experiments nor theoretical results could show any tendency of the high ellipticity jets to behave similar to planar sheets in which sinuous (antisymmetric) waves are dominant. A nonlinear analysis or experimental investigation with

high ellipticity jets ($e < 0.1$) might show this sinuous behavior. Furthermore, the corner effects in a rectangular jet might show this difference. The corners of a planar sheet have no curvature while those of an elliptic jet have a considerable curvature.

5.2 Recommendations for future work

The present work is aimed at developing analytical tools to understand the main features of elliptic jets including axis-switching and breakup. The following topics are suggested to further expand the research and increase the fundamental knowledge in this field.

- To capture the exact amount of growth rate and cut-off wavenumber a nonlinear analysis is required. A nonlinear solution of the 3rd order is enough to capture quantitatively the main fluid parameters. With a nonlinear analysis, investigating the size of main and satellite drops can be performed as well. In the experimental part, high values of the imposed voltage can be used to enter the nonlinear regions. In addition, imposing the harmonics of the main wave, and waveforms other than the sinusoidal will be useful too.
- In the current theoretical models, the jet velocity was taken to be uniform, i.e. a plug flow was assumed. This assumption holds true only for short nozzles. To obtain quantitative results for any nozzle length, a realistic jet profile must be considered. Accordingly, longer nozzles (i.e. $L/D > 10$) should be used in the validating experiments.
- To yield a more practical solution, in the 3-D model, the effects of viscosity and swirl for liquid and gas phases can be added (e.g. through Helmholtz decomposition method and adding free vortex to the velocity potential).
- A numerical solution of three-dimensional inviscid and quasi-one-dimensional equations is highly recommended. The numerical solution of the quasi-one-dimensional equations yields the jet profile which shows the breakup and axis-switching modes better. The effect of various parameters such as viscosity, high ellipticity, and even turbulence can be more easily captured by using an efficient numerical analysis.

- The present results show that a combination of active and passive control can potentially produce liquid jets with desirable forms. Providing a closed-loop control system which can manipulate the size and distribution of the main and satellite droplets might have excellent applications.

References

1. Amini, G., Dolatabadi, A., Capillary instability of elliptic liquid jets. *Phys. Fluids* 23, 084109 (2011a).

2. Amini, G., Dolatabadi, A., Three-dimensional instability analysis of elliptic liquid jets, *J. Fluid Mech*. JFM-11-S-0865 (2011b, Submitted).

3. Amini, G., Dolatabadi, A., Axis-switching and breakup of low-speed elliptic liquid jets, *Int. J. Multip. Flow* IJMF-D-11-00261 (2011c, Submitted).

4. Ashgriz, N., Mashayekh, F., Temporal analysis of capillary jet breakup. *J. Fluid. Mech.* 291, 163-190 (1995).

5. Avital, E., Asymmetric instability of a viscid capillary jet in an inviscid media. *Phys. Fluids,* 7, 1162-1164 (1995).

6. Batchelor, G. K., Gill, A. E., Analysis of the stability of axisymmetric jets. *J. Fluid Mech.* 14, 529-551 (1962).

7. Bechtel, S. E., The oscillation of slender Elliptical inviscid and Newtonian jets: effects of surface tension, inertia, viscosity and gravity. *Trans. ASME* 56, 968-974 (1989).

8. Bechtel, S. E., Cooper, J. A., Forest, M. G., Petersson, N. A., Reichard, D. L., Saleh, A., Venkataramanan, V., A new model to determine dynamic surface tension and elongational viscosity using oscillating jet measurements. *J. Fluid Mech.* 293, 379-403 (1995).

9. Bechtel, S. E., Forest, M. G., Lin, K. J., Closure to all orders in 1-D models for slender viscoelastic free jets I. An integrated theory for axisymmetric torsionless flows. *Stability Appl. Anal. Cont. Media* 2, 59-100 (1992).

10. Bechtel, S. E., Forest, M. G., Holm, D. D., Lin, K. J., 1-D closure models for 3-D incompressible viscoelastic free jets: Von Karman flow geometry and elliptical cross section. *J. Fluid Mech.* 196, 241-262 (1988).

11. Bidone, G., Experiences sur la forme et sur la direction des viens des courans d'eau lances par diverses ouvertures. Academia delle scienze di Torino 34, 229-362 (1830).

12. Birouk, M., Lekic, N., Liquid breakup in quiescent atmosphere; a review. *Atomization and Sprays*, 19, 501-528 (2009).

13. Bogy, D. B., Use of one-dimensional Cosserat theory to study instability in a viscous liquid jet. *Phys. Fluids* 21, 190-197 (1978a).

14. Bogy, D. B., Wave propagation and instability in a circular semi-infinite liquid jet harmonically forced at the nozzle. *J. Appl. Mech*. 45, 469-474 (1978b).

15. Bogy, D. B., Break-up of a liquid jet: second perturbation solution for one-dimensional Cosserat theory. *IBM J. Res. Dev.* 23, 87-92 (1979a).

16. Bogy, D. B., Break-up of a liquid jet: third perturbation Cosserat solution. *Phys. Fluids* 22, 224-230 (1979b).

17. Bogy, D. B., Drop formation in a circular liquid jet. *Ann. Rev. Fluid. Mech*., 11, 207-228 (1979c).

18. Bogy, D. B., Shine, S. J., Talke, F. E., Finite difference solution of the Cosserat fluid jet equations. *J. Comp. Phys*. 38, 294-326 (1980).

19. Bohr, N., Determination of dynamic surface tension by the method of jet vibration. *Philos. Trans. R. Soc. Lond*. 209, 281–317 (1909).

20. Bruce, C. A., Dependence of ink jet dynamics on fluid characteristics. *IBM J. Res. Dev*. 1, 258- 268 (1976).

21. Caulk, D. A., Naghdi, P.M., On the onset of breakup in inviscid and viscous jets. *J. Appl. Mech.* 46, 291-297 (1979).

22. Caulk, D. A., Naghdi, P. M., The influence of twist on the motion of a straight elliptical jet. Univ. Calif., Berkeley, Dep. Mech. Eng. Rep. No. UCB/AM- 77-5 (1977).

23. Chaudhary, K. C., Redekopp, L. G., The nonlinear capillary instability of a liquid jet. Part 1. Theory. *J. Fluid Mech*., 96, 257-274 (1980).

24. Chaudhary, K. C., Maxworthy, T., The nonlinear capillary instability of a liquid jet. Part 2. Experiment on jet behavior before droplet formation. *J. Fluid Mech*., 96, 275-286 (1980).

25. Chigier, N., Reitz, R. D., Regimes of jet breakup and breakup mechanisms (physical aspects). In: Kuo, K. K., (ed) Recent advances in spray combustion: spray atomization and drop burning phenomena. Progress in Astronautics and Aeronautics, American Institute of Aeronautics and Astronautics, vol. I, chap. 4, 109-135 (1996).

26. Clark, C. J., Dombrowski, N., Aerodynamic instability and disintegration of inviscid liquid sheets. *Proc. R. Soc. Lond. Ser A*. 329, 467–78 (1972).

27. Cline, H. E., Anthony, T.R., The effect of harmonics on the capillary instability of liquid jets. *J. Appl. Phys.* 49, 3203-3208 (1978).

28. Crighton, D. G., Instability of an elliptic jet. *J. Fluid Mech*. 59, 665-672 (1973).

29. Cosserat, E., Cosserat, F., Theorie des Corps Deformables. Pads Hermann (1909).

30. Debler, W., Yu, D., The break-up of laminar liquid jets. *Proc. R. Soc. Lond*. A 415, 107-119 (1988).

31. Dityakin, Y. F., On the stability and breakup into drops of a liquid jet of elliptical cross section. *Izv. Akad. Nauk SSSR Otdel. Tekhn Nauk* 10, 124-130 (1954).

32. Dombrowski, N., Hooper, P. C., The effect of ambient density on drop formation in sprays. *Chem. Eng. Sci*. 17, 291– 305 (1962).

33. Dumouchel, C., Experimental analysis of a liquid atomization process at low Weber number. In: Proceedings of international symposium on heat and mass transfer in spray systems, Antalya, Turkey (2005).

34. Dumouchel, C., On the experimental investigation on primary atomization of liquid streams. *Exp. Fluids* 45, 371–422 (2008).

35. Eggers, J., Dupont, T. F., Drop formation in a one-dimensional approximation of the Navier–Stokes equations. *J. Fluid Mech*. 262, 205–221 (1994).

36. Garcia F. J., Castellanos, A., One-dimensional models for slender axisymmetric viscous liquid jets. *Phys. Fluids* 6, 2676-2689 (1994).

37. Geer, J. F., Strikwerda, J. C., Vertical slender jets with surface tension. *J. Fluid Mech*. 135, 155-169 (1983).

38. Gertsenshtein, S. Ya, Shkadov, V. Ya, Stability of asymmetric liquid jets. *Izvestiya Akademii Nauk SSSR, Mekhanika Zhidkosti i Gaza*, 1, 43-52 (1973).

39. Gonzalez, H., Garcia, F. J., The measurement of growth rates in capillary jets. *J. Fluid Mech.* 619, 179-212 (2009).

40. Green, A. E., On the non-linear behavior of fluid jets. *Int. J. Eng. Sci.* 14, 49-63 (1976).

41. Green, A. E., On the steady motion of jets with elliptical sections. *Acta Mech.* 26, 171-177 (1977).

42. Green, A. E., Laws, N., A general theory of rods. *Proc. R. Soc*., 293, 145-155 (1966).

43. Gutmark, E. J., Grinstein, F. F., Flow control with noncircular jets. *Annu. Rev. Fluid Mech.* 31, 239-272 (1999).

44. Hagerty, W. W., Shea, J. F., A study of the stability of plane fluid sheets. *J. Appl. Mech.* 22, 509-514 (1955).

45. Hiroyasu, H., Shimizu, M., Arai, M., The breakup of a high speed jet in a high pressure gaseous atmosphere. *ICLASS*-82, 69-74 (1982).

46. Ibrahim, E. A., Akpan, E. T., Three-dimensional instability of viscous liquid sheets. *Atomization and Sprays* 6, 649–665 (1996).

47. Ibrahim, E. A., Marshall, S. O., Instability of a liquid jet of parabolic velocity profile. *Chem. Eng. J.* 76, 17-21 (2000).

48. Jazayeri, S. A., Li, X., Nonlinear instability of plane liquid sheets. *J. Fluid Mech*. 406, 281-308 (2000).

49. Johns, L. E., Narayanan, R., Interfacial instability. *Springer*, (2002).

50. Kalaaji, A., Lopez, B., Attane, P., Soucemarianadin, A., Breakup length of forced liquid jets. *Phys. Fluids*, 15, 2469-2479 (2003).

51. Kasyap, V. D., Sivakumar, D., Raghunandan, B. N., Flow and breakup characteristics of elliptical liquid jets. *Int. J. Multip. Flow* 35, 8-19 (2009).

52. Keller, J. B., Rubinow, S. I., Tu, Y. O., Spatial instability of a jet. *Phys. Fluids* 16, 2052-2055 (1973).

53. Lafrance, P., Nonlinear breakup of a laminar liquid jet. *Phys. Fluids* 18, 428-432 (1975).

54. Lee, H. C., Drop formation in a liquid jet. *IBM J. Res. Dev*. 18, 364-369 (1974).

55. Leib, S. J., Goldstein, M. E., The generation of capillary instability on a liquid jet. *J. Fluid Mech*. 168, 479–500 (1986a).

56. Leib, S. J., Goldstein, M. E., Convective and absolute instability of a viscous liquid jet. *Phys. Fluids* 29, 952–954 (1986b).

57. Levich, V. G., Physicochemical Hydrodynamics. Prentice-Hall, New Jersey (1962).

58. Li, R., Ashgriz, N., Characteristics of liquid sheets formed by two impinging jets. *Phys. Fluid* 18, 087104 (2006).

59. Li, X., Tankin, R. S., On the temporal instability of a two-dimensional viscous liquid sheet. *J. Fluid Mech.* 226, 425–443 (1991).

60. Lin, S. P., Creighton, B., Energy budget in atomization. *J. Aero. Sci. Tech*. 12, 630–636 (1990).

61. Lin, S. P., Reitz, R. D., Drop and spray formation from a liquid jet. *Annu. Rev. Fluid Mech.* 30, 85-105 (1998).

62. McCarthy, M. J, Molloy, N. A., Review of stability of liquid jets and the influence of nozzle design. *Chem. Eng. J*. 7, 1–20 (1974).

63. McHale, R. M., Nurick, W. H., Clapp, S. D., Injector design criteria using noncircular orifice geometry. *J. Spacecraft Rockets*, 8, 408-410 (1971).

64. McLachlan, N. W., Theory and Application of Mathieu Functions. Dover Publications (1964).

65. Messina, T., Acharya, S., Characteristics of an acoustically modulated spray issued from circular and elliptical orifice nozzles. *Atomization and Sprays*, 16, 331-348 (2006).

66. Morris, P. J., Instability of elliptic jets. *AIAA J*. 26, 172-178 (1986).

67. Nayfeh, A. H., Nonlinear stability of a liquid jet. *Phys. Fluids* 13, 841-847 (1970).

68. Pimbley, W. T., Drop formation from a liquid jet: A linear one-dimensional analysis considered a boundary value problem. *IBM J. Res. Dev*., 20, 148-156 (1976).

69. Plateau, J., Statique experimentale et theorique des liquids soumie aux seules forces moleculaire, vols. 1, 2. Paris: Cauthier Villars. 450- 495 (1873).

70. Rangel, R. H., Sirignano, W. A., The linear and nonlinear shear instability of a fluid sheet. *Phys. Fluids* 3, 2392–2400 (1991).

71. Rayleigh, L., On the instability of a cylinder of viscous liquid under capillary force. *Phil. Mag*. 34,145–154 (1892).

72. Rayleigh, L., On the tension of recently formed surfaces. *Proc. R. Soc. Lond*. 41, 281-287 (1890).

73. Rayleigh, L., On the capillary phenomena of jets. *Proc. R. Soc*., 29, 71-97 (1879).

74. Reitz, R. D., Bracco, F. V., Mechanism of atomization of a liquid jet. *Phys. Fluids* 25, 1730-1742 (1982).

75. Rohani, M., Jabbari, F., Dunn-Rankin D., Breakup control of a liquid jet by disturbance manipulation. *Phys. Fluids* 22, 107103 (2010).

76. Senecal, P. K., Schmidt, D. P., Nouar, I., Rutland, C. J., Reitz, R. D., Corradini, M. L., Modeling high-speed viscous liquid sheet atomization. *Int. J. Multip. Flow* 25, 1073-1097 (1999).

77. Sirignano, W. A., Mehring, C., Review of theory of distortion and disintegration of liquid streams. *Prog. Energy Comb. Sci*. 26, 609-655 (2000).

78. Squire, H. B., Investigation on the instability of a moving liquid film. *J. Appl. Phys*. 4, 167–169 (1953).

79. Sterling, A. M., Sleicher, C. A., The instability of capillary jets. *J. Fluid Mech*. 68, 447-495 (1975).

80. Taylor, G. I., Generation of ripples by wind blowing over viscous fluids. In The Scientific Papers of G. I. Taylor, ed. Batchelor, G. K., Cambridge Univ. Press (1962).

81. Taylor, G. I., Formation of thin flat sheets of water. *Proc. R. Soc*., 259, 1-17 (1960).

82. Weber, C. Z., Zum Zerfall eines Flussigkeitsstrahles. *Math. Mech*. 11, 136-154 (1931).

83. Yang, H. Q., Asymmetric instability of a liquid jet. *Phys. Fluids* 4, 681-689 (1992).

84. Yunyi, G., Changwen, L., Yezhou, H., Zhijun, P., An experimental study on droplet size characteristics and air entrainment of elliptic sprays, *SAE International* fall fuels and lubricants meeting and exposition, San Francisco, California, paper no. 982546 (1998).

Appendices

Appendix A

Definitions of used Mathieu and modified Mathieu functions are as follows. I_m and K_m are the m^{th} order modified Bessel functions of the first and second kind respectively. The functions ce_m and se_m are analogous to cos($m\theta$) and sin($m\theta$) while Ce_m and Se_m are analogous to I_m and Fek_m and Gek_m to K_m in the case of the circular jet. A and B are expansion coefficients which have been calculated using an algorithm mentioned in McLachlan (1964).

$$ce_{2m}(\rho,-q) = (-1)^m \frac{ce_{2n}(0,q)}{A_0^{(2m)}} \sum_{r=0}^{\infty} (-1)^r A_{2r}^{(2m)} I_{2r}(2\sqrt{q}\cos\rho) \tag{A.1}$$

$$ce_{2m+1}(\rho,-q) = (-1)^m \frac{se_{2m+1}(0,q)}{\sqrt{q}B_1^{(2m+1)}} \sum_{r=0}^{\infty} (-1)^r B_{2r+1}^{(2m+1)} I_{2r+1}(2\sqrt{q}\cos\rho) \tag{A.2}$$

$$se_{2m+1}(\rho,-q) = (-1)^m \frac{ce_{2m+1}(0,q)}{\sqrt{q}A_1^{(2m+1)}} \tan\rho \sum_{r=0}^{\infty} (-1)^r (2r+1) A_{2r+1}^{(2m+1)} I_{2r+1}(2\sqrt{q}\cos\rho) \tag{A.3}$$

$$se_{2m+2}(\rho,-q) = (-1)^m \frac{se'_{2m+2}(0,q)}{qB_2^{(2m+2)}} \tan\rho \sum_{r=0}^{\infty} (-1)^r (2r+2) B_{2r+2}^{(2m+2)} I_{2r+2}(2\sqrt{q}\cos\rho) \tag{A.4}$$

$$Ce_m(\rho,-q) = ce_m(i\rho,-q) \tag{A.5}$$

$$Se_m(\rho,-q) = -ise_m(i\rho,-q) \tag{A.6}$$

$$Ce_{2m}(\rho,-q)=(-1)^m\frac{ce_{2m}(0,q)}{A_0^{(2m)}}\sum_{r=0}^{\infty}(-1)^r A_{2r}^{(2m)}I_{2r}(2\sqrt{q}\cosh\rho) \tag{A.7}$$

$$Fek_{2m}(\rho,-q)=(-1)^m\frac{ce_{2m}(0,q)}{\pi A_0^{(2m)}}\sum_{r=0}^{\infty}(-1)^r A_{2r}^{(2m)}K_{2r}(2\sqrt{q}\cosh\rho) \tag{A.8}$$

$$Ce_{2m+1}(\rho,-q)=(-1)^m\frac{se'_{2m+1}(0,q)}{\sqrt{q}B_1^{(2m+1)}}\sum_{r=0}^{\infty}(-1)^r B_{2r+1}^{(2m+1)}I_{2r+1}(2\sqrt{q}\cosh\rho) \tag{A.9}$$

$$Fek_{2m+1}(\rho,-q)=(-1)^m\frac{se'_{2m+1}(0,q)}{\pi\sqrt{q}B_1^{(2m+1)}}\sum_{r=0}^{\infty}(-1)^r B_{2r+1}^{(2m+1)}K_{2r+1}(2\sqrt{q}\cosh\rho) \tag{A.10}$$

$$Se_{2m+1}(\rho,-q)=(-1)^{m+1}\frac{ce'_{2m+1}(\frac{\pi}{2},q)}{\sqrt{q}A_1^{(2m+1)}}\sum_{r=0}^{\infty}A_{2r+1}^{(2m+1)}I_{2r+1}(2\sqrt{q}\sinh\rho) \tag{A.11}$$

$$Gek_{2m+1}(\rho,-q)=(-1)^{m+1}\frac{ce'_{2m+1}(\frac{\pi}{2},q)}{\pi\sqrt{q}A_1^{(2m+1)}}\sum_{r=0}^{\infty}A_{2r+1}^{(2m+1)}K_{2r+1}(2\sqrt{q}\sinh\rho) \tag{A.12}$$

$$Se_{2m+2}(\rho,-q)=(-1)^{m+1}\frac{se'_{2m+2}(\frac{\pi}{2},q)}{qB_2^{(2m+2)}}\coth\rho\sum_{r=0}^{\infty}(2r+2)B_{2r+2}^{(2m+2)}I_{2r+2}(2\sqrt{q}\sinh\rho) \tag{A.13}$$

$$Gek_{2m+2}(\rho,-q)=(-1)^{m+1}\frac{se'_{2m+2}(\frac{\pi}{2},q)}{\pi qB_2^{(2m+2)}}\coth\rho\sum_{r=0}^{\infty}(2r+2)B_{2r+2}^{(2m+2)}K_{2r+2}(2\sqrt{q}\sinh\rho) \tag{A.14}$$

Appendix B

Coefficients of mean curvature, κ, resulted from linearization in equation (2.64), are given by,

$$l_1 = \frac{(-e^{1.5}/R)}{(\sin^2\theta + e^2\cos^2\theta)^{1.5}} \tag{B.1}$$

$$l_2 = (-e^2/R^2)\left(\frac{1}{(\sin^2\theta + e^2\cos^2\theta)^{1.5}} - \frac{3\sin^2\theta}{(\sin^2\theta + e^2\cos^2\theta)^{2.5}}\right) \tag{B.2}$$

$$l_3 = (-e/R^2)\left(\frac{1}{(\sin^2\theta + e^2\cos^2\theta)^{1.5}} - \frac{3e^2\cos^2\theta}{(\sin^2\theta + e^2\cos^2\theta)^{2.5}}\right) \tag{B.3}$$

$$l_4 = \frac{e\cos^2\theta}{(\sin^2\theta + e^2\cos^2\theta)^{0.5}} \tag{B.4}$$

$$l_5 = \frac{\sin^2\theta}{(\sin^2\theta + e^2\cos^2\theta)^{0.5}} \tag{B.5}$$

Appendix C

The main kinematics and differential equations characterizing the motion of a directed elliptic liquid jet, designates as $\mathcal{R}$, in the form derived by Caulk and Naghdi (1977, 1979) are summarized here. Quasi-one-dimensional directed medium comprises a material line and a pair of directors attached to every point of the material line. Using a fixed system of rectangular Cartesian coordinates (x, y, z), we assume that the material line of $\mathcal{R}$ is identified along the z-axis and the director pair lies in the x-y plane (See figure 3.2). let $\mathcal{C}$, the curve occupied by the material line of $\mathcal{R}$ in the present configuration at time t, be described by its position vector r relative to a fixed origin, and let d_α (α=1,2) stand for the pair of directors at r. Then a motion of the directed curve $\mathcal{R}$ is specified by,

$$r = r(z,t), \;\; d_\alpha = d_\alpha(z,t). \tag{C.1}$$

The velocity and the director velocities are defined by,

$$v = r_t, \;\; w_\alpha = d_{\alpha t} \tag{C.2}$$

where subscript t designates the material time derivative holding z fixed. We restrict motions of the directed curve $\mathcal{R}$ such that in the present configuration at time t,

$$r = z(z,t)\vec{k}, \;\; d_1 = \phi_1\vec{i}, \;\; d_2 = \phi_2\vec{j} \tag{C.3}$$

where ϕ_1 and ϕ_2 are semi-major and semi-minor axes of the elliptic cross-section, respectively. The velocity, the acceleration, the director velocities, and the director accelerations assume the form,

$$\vec{v} = v\vec{k}, \quad v = z_t, \quad \vec{v}_t = v_t\vec{k} \tag{C.4}$$

and

$$w_1 = \phi_1\zeta_1\vec{i}, \quad w_2 = \phi_2\zeta_2\vec{j}, \quad w_{1t} = (\zeta_{1t} + \zeta_1^2)\phi_1\vec{i}, \quad w_{2t} = (\zeta_{2t} + \zeta_2^2)\phi_2\vec{j} \tag{C.5}$$

where

$$\phi_{1t} = -v\phi_{1z} + \phi_1\zeta_1, \quad \phi_{2t} = -v\phi_{2z} + \phi_2\zeta_2. \tag{C.6}$$

The condition expressing the incompressibility of the fluid medium is given by,

$$\zeta_1 + \zeta_2 + v_z = 0 \tag{C.7}$$

and the differential equations of motion of the elliptic jet described above are,

$$\frac{1}{4}\pi\rho\phi_1^3\phi_2(\zeta_{1t} + v\zeta_{1z} + \zeta_1^2) = p + \phi_1\phi_2 h(\phi_1,\phi_2) - 2\mu\pi\phi_1\phi_2\zeta_1 + \frac{1}{4}\mu\pi(\phi_1^3\phi_2\zeta_{1z})_z,$$

$$\frac{1}{4}\pi\rho\phi_2^3\phi_1(\zeta_{2t} + v\zeta_{2z} + \zeta_2^2) = p + \phi_1\phi_2 h(\phi_2,\phi_1) - 2\mu\pi\phi_1\phi_2\zeta_2 + \frac{1}{4}\mu\pi(\phi_2^3\phi_1\zeta_{2z})_z, \tag{C.8}$$

$$\pi\rho\phi_1\phi_2(v_t + vv_z) = -p_z - \phi_2\phi_{1z}h(\phi_1,\phi_2) - \phi_1\phi_{2z}h(\phi_2,\phi_1) + 2\mu\pi(\phi_1\phi_2 v_z)_z.$$

The process of linearization of above mentioned equations are as follows. The main parameters are expanded as,

$$\phi_1 = a + \bar{\phi}_1, \qquad \phi_2 = b + \bar{\phi}_2, \qquad p = p_0 + \bar{p}, \qquad v = V + \bar{v}. \tag{C.9}$$

The bar mark represents the value of the perturbed parameter. *a* and *b* are the initial semi-major and semi-minor axes, respectively (See figure 3.2). The uniform jet velocity is represented by *V*,

and p_0 is the initial pressure and is assumed constant inside the liquid column. Using equations (C.6) and (C.7), continuity equation takes the form of,

$$\frac{\phi_{1t}+v\phi_{1z}}{\phi_1}+\frac{\phi_{2t}+v\phi_{2z}}{\phi_2}+v_z=0 \tag{C.10}$$

By replacing expansion parameters (C.9) in equation (C.10), the form of continuity equation changes to,

$$\bar{v}_z ab+b\bar{\phi}_{1t}+a\bar{\phi}_{2t}=0 \tag{C.11}$$

Average of capillary force on the jet cross section, equation (3.9), is linearized as,

$$h(\phi_1,\phi_2)=\sigma\int_0^{2\pi}\frac{[(a^2\sin^2\theta+b^2\cos^2\theta)(\bar{\phi}_{1zz}b\cos^2\theta+\bar{\phi}_{2zz}a\sin^2\theta)-(ab+a\bar{\phi}_2+b\bar{\phi}_1)]}{[(a^2+2a\bar{\phi}_1)\sin^2\theta+(b^2+2b\bar{\phi}_2)\cos^2\theta]^{3/2}}d\theta \tag{C.12}$$

and after integration, this term will be equal to,

$$h(\phi_1,\phi_2)=k_1+k_2\bar{\phi}_1+k_3\bar{\phi}_2+k_4\bar{\phi}_{1zz}+k_5\bar{\phi}_{2zz} \tag{C.13}$$

and similarly,

$$h(\phi_2,\phi_1)=k_1+k_2\bar{\phi}_2+k_3\bar{\phi}_1+k_4\bar{\phi}_{2zz}+k_5\bar{\phi}_{1zz} \tag{C.14}$$

Constants have been defined at the end of this appendix. Other terms of momentum equation (C.8) are linearized as,

$$\zeta_{1t} + v\zeta_{1z} + \zeta_1^2 = \frac{\bar{\phi}_{1tt}}{a} \tag{C.15}$$

$$\zeta_{2t} + v\zeta_{2z} + \zeta_2^2 = \frac{\bar{\phi}_{2tt}}{b} \tag{C.16}$$

$$\frac{1}{4}\pi\rho\phi_1^3\phi_2(\zeta_{1t} + v\zeta_{1z} + \zeta_1^2) = \frac{1}{4}\pi\rho a^2 b\bar{\phi}_{1tt} \tag{C.17}$$

$$\frac{1}{4}\pi\rho\phi_2^3\phi_1(\zeta_{2t} + v\zeta_{2z} + \zeta_2^2) = \frac{1}{4}\pi\rho a b^2\bar{\phi}_{2tt} \tag{C.18}$$

$$2\mu\pi(\phi_1\phi_2 v_z)_z = 2\mu\pi ab v_{zz} \tag{C.19}$$

$$2\mu\pi\phi_1\phi_2\zeta_1 = 2\mu\pi b\bar{\phi}_{1t} \tag{C.20}$$

$$2\mu\pi\phi_1\phi_2\zeta_2 = 2\mu\pi a\bar{\phi}_{2t} \tag{C.21}$$

$$\frac{1}{4}\mu\pi(\phi_1^3\phi_2\zeta_{1z})_z = \frac{1}{4}\mu\pi a^2 b\bar{\phi}_{1tzz} \tag{C.22}$$

$$\frac{1}{4}\mu\pi(\phi_2^3\phi_1\zeta_{12})_z = \frac{1}{4}\mu\pi a b^2\bar{\phi}_{2tzz} \tag{C.23}$$

$$\phi_2\phi_{1z}h(\phi_1,\phi_2) = bk_1\bar{\phi}_{1z} \tag{C.24}$$

$$\phi_1\phi_{2z}h(\phi_2,\phi_1) = ak_1\bar{\phi}_{2z} \tag{C.25}$$

$$\phi_1\phi_2 h(\phi_1,\phi_2) = N_1 + N_2\bar{\phi}_2 + N_3\bar{\phi}_1 + N_4\bar{\phi}_{2zz} + N_5\bar{\phi}_{1zz} \tag{C.26}$$

$$\phi_2\phi_1 h(\phi_2,\phi_1) = M_1 + M_2\bar{\phi}_1 + M_3\bar{\phi}_2 + M_4\bar{\phi}_{1zz} + M_5\bar{\phi}_{2zz} \tag{C.27}$$

Coefficients of *M* and *N* have been defined at the end of this appendix. In conclusion, momentum equations (C.8) in three-directions become,

$$\begin{aligned}
&\frac{1}{4}\pi\rho a^2 b\bar{\phi}_{1tt} + 2\mu\pi b\bar{\phi}_{1t} = p_0 + \bar{p} + N_1 + N_2\bar{\phi}_2 + N_3\bar{\phi}_1 + N_4\bar{\phi}_{2zz} + N_5\bar{\phi}_{1zz} + \frac{1}{4}\mu\pi a^2 b\bar{\phi}_{1tzz} \\
&\frac{1}{4}\pi\rho a b^2\bar{\phi}_{2tt} + 2\mu\pi a\bar{\phi}_{2t} = p_0 + \bar{p} + M_1 + M_2\bar{\phi}_1 + M_3\bar{\phi}_2 + M_4\bar{\phi}_{1zz} + M_5\bar{\phi}_{2zz} + \frac{1}{4}\mu\pi a b^2\bar{\phi}_{2tzz} \\
&\pi\rho ab\bar{v}_t = -\bar{p}_z - bk_1\bar{\phi}_{1z} - ak_1\bar{\phi}_{2z} + 2\mu\pi ab v_{zz}.
\end{aligned} \tag{C.28}$$

By eliminating the pressure term among equations (C.26), two equations are derived,

$$\begin{aligned}
&[(-\frac{1}{4}\pi\rho a^2 b)\bar{\phi}_{1ttzz} + (\pi\rho b)\bar{\phi}_{1tt} + (-4\mu\pi b)\bar{\phi}_{1tzz} + (\frac{1}{4}\mu\pi a^2 b)\bar{\phi}_{1tzzzz} + (N_5)\bar{\phi}_{1zzzz} + (N_3 - bk_1)\bar{\phi}_{1zz}] + \\
&[(\pi\rho a)\bar{\phi}_{2tt} + (-2\mu\pi a)\bar{\phi}_{2tzz} + (N_2 - ak_1)\bar{\phi}_{2zz} + (N_4)\bar{\phi}_{2zzzz} = 0 \\
&[(\pi\rho b)\bar{\phi}_{1tt} + (-2\mu\pi b)\bar{\phi}_{1tzz} + (M_2 - bk_1)\bar{\phi}_{1zz} + (M_4)\bar{\phi}_{1zzzz}] + \\
&[(-\frac{1}{4}\pi\rho b^2 a)\bar{\phi}_{2ttzz} + (\pi\rho a)\bar{\phi}_{2tt} + (-4\mu\pi a)\bar{\phi}_{2tzz} + (\frac{1}{4}\mu\pi b^2 a)\bar{\phi}_{tzzzz} + (M_5)\bar{\phi}_{2zzzz} + (M_3 - ak_1)\bar{\phi}_{2zz}] = 0
\end{aligned} \tag{C.29}$$

Replacing a Fourier form for perturbed part of ϕ_1 and ϕ_2 as,

$$\begin{aligned}
&\bar{\phi}_1 = f_1(k)\exp[i(\alpha t - kz)] \\
&\bar{\phi}_2 = f_2(k)\exp[i(\alpha t - kz)].
\end{aligned} \tag{C.30}$$

in equation (C.29), will result equation (3.14). Coefficients of system of equations (3.14) resulted from linearization of Cosserat equations are as follows,

$$S_1 = (D_2\beta^2 + D_1\beta + D_0)(e^2\pi\sigma / R^2) \tag{C.31}$$

$$S_2 = (D_2'\beta^2 + D_1'\beta + D_0')(e^2\pi\sigma / R^2) \tag{C.32}$$

$$S_3 = (C_2\beta^2 + C_1\beta + C_0)(e^2\pi\sigma / R^2) \tag{C.33}$$

$$S_4 = (C_2'\beta^2 + C_1'\beta + C_0')(e^2\pi\sigma / R^2) \tag{C.34}$$

where

$$C_0 = (1/\pi)(E_5K^4 - (3e^2E_3 - E_1)K^2) \tag{C.35}$$

$$C_1 = Oh(2K^2) \tag{C.36}$$

$$C_2 = 1 \tag{C.37}$$

$$C_0' = (e/\pi)(E_4K^4 - (3E_2 - E_1)K^2) \tag{C.38}$$

$$C_1' = Oh(0.25eK^4 + 4K^2/e) \tag{C.39}$$

$$C_2' = 0.25eK^2 + 1/e \tag{C.40}$$

$$D_0 = (e/\pi)(E_4K^4 - (3E_2 - E_1)K^2) \tag{C.41}$$

$$D_1 = Oh(0.25K^4 + 4K^2) \tag{C.42}$$

$$D_2 = 0.25K^2 + 1 \tag{C.43}$$

$$D_0' = (1/\pi)(E_5K^4 - (3e^2E_3 - E_1)K^2) \tag{C.44}$$

$$D_1' = Oh(2K^2/e) \tag{C.45}$$

$$D_2' = 1/e \tag{C.46}$$

and

$$E_1 = \int_0^{2\pi} \frac{\cos^2\theta \quad d\theta}{(\sin^2\theta + e^2\cos^2\theta)^{1.5}} \tag{C.47}$$

$$E_2 = \int_0^{2\pi} \frac{\sin^2\theta\cos^2\theta \quad d\theta}{(\sin^2\theta + e^2\cos^2\theta)^{2.5}} \tag{C.48}$$

$$E_3 = \int_0^{2\pi} \frac{\cos^4\theta \quad d\theta}{(\sin^2\theta + e^2\cos^2\theta)^{2.5}} \tag{C.49}$$

$$E_4 = \int_0^{2\pi} \frac{\cos^4\theta \quad d\theta}{(\sin^2\theta + e^2\cos^2\theta)^{0.5}} \tag{C.50}$$

$$E_5 = \int_0^{2\pi} \frac{\sin^2\theta\cos^2\theta \quad d\theta}{(\sin^2\theta + e^2\cos^2\theta)^{0.5}}. \tag{C.51}$$

In the above equations, following parameters have been used,

$$k_1 = -\sigma\frac{b}{a^2}E_1 \tag{C.52}$$

$$k_2 = \sigma \frac{b}{a^3}(-E_1 + 3E_2) \tag{C.53}$$

$$k_3 = \sigma \frac{1}{a^2}(-E_1 + 3e^2 E_3) \tag{C.54}$$

$$k_4 = \sigma e E_4 \tag{C.55}$$

$$k_5 = \sigma E_5 \tag{C.56}$$

$$M_1 = -\sigma a e^2 E_1 \tag{C.57}$$

$$M_2 = \sigma(-eE_1 + 3e^3 E_3 - e^2 E_1) \tag{C.58}$$

$$M_3 = \sigma(-e^2 E_1 + 3e^2 E_2 - eE_1) \tag{C.59}$$

$$M_4 = \sigma a^2 e E_5 \tag{C.60}$$

$$M_5 = \sigma a^2 e^2 E_4 \tag{C.61}$$

$$N_1 = -\sigma a e^2 E_1 \tag{C.62}$$

$$N_2 = \sigma(3e^3 E_3 - 2eE_1) \tag{C.63}$$

$$N_3 = \sigma(3e^2 E_2 - 2e^2 E_1) \tag{C.64}$$

$$N_4 = \sigma a^2 e E_5 \tag{C.65}$$

$$N_5 = \sigma a^2 e^2 E_4 \tag{C.66}$$

Appendix D

Coefficients of temporal dispersion relation in equation (3.15) are given by,

$$a_0 = A_0^{(6)}K^6 + A_0^{(4)}K^4 + A_0^{(2)}K^2 \tag{D.1}$$

$$a_1 = A_1^{(6)}K^6 + A_1^{(4)}K^4 + A_1^{(2)}K^2 \tag{D.2}$$

$$a_2 = -(A_2^{(6)}K^6 + A_2^{(4)}K^4 + A_2^{(2)}K^2 + A_2^{(0)}) \tag{D.3}$$

$$a_3 = -(A_3^{(4)}K^4 + A_3^{(2)}K^2 + A_3^{(0)}) \tag{D.4}$$

$$a_4 = A_4^{(2)}K^2 + A_4^{(0)} \tag{D.5}$$

where

$$A_0^{(2)} = (1/\pi^2)(2e^4(-E_1 + 3E_2)^2 - 2e^2(E_1 - 3e^2E_3)^2) \tag{D.6}$$

$$A_0^{(4)} = (1/\pi^2)(4e^4E_1E_4 - 12e^4E_2E_4 - 4e^2E_1E_5 + 16e^4E_3E_5) \tag{D.7}$$

$$A_0^{(6)} = (2/\pi^2)(e^4E_4^2 - e^2E_5^2) \tag{D.8}$$

$$A_1^{(2)} = (Oh/\pi)((8e^3 - 4e)E_1 - (24e^3 + 24e^2)E_2 + (12e^4 + 12e^3)E_3) \tag{D.9}$$

$$A_1^{(4)} = (Oh/\pi)((0.5e^4 + 0.5e^3)E_1 - (1.5e^4 + 1.5e^3)E_2 + (8e^3 + 8e^2)E_4 - (4e^2 + 4e)E_5) \tag{D.10}$$

$$A_1^{(6)} = (0.5Ohe^3/\pi)(1+e)E_4 \tag{D.11}$$

$$A_2^{(0)} = (2/\pi)((-e^3 + e)E_1 + (3e^3 + 3e^2)E_2 - (3e^4 + 3e^3)E_3) \tag{D.12}$$

$$A_2^{(2)} = (0.5e^2/\pi)(-(e + e^2)E_1 + (3e + 3e^2)E_2 - (4e + 4)E_4 + (4 + 4/e)E_5 - 48\pi Oh^2/e) \tag{D.13}$$

$$A_2^{(4)} = (-0.5e^2/\pi)((e + e^2)E_4 + 4\pi Oh^2(1 + e^2)/e) \tag{D.14}$$

$$A_2^{(6)} = -0.125Oh^2e^3 \tag{D.15}$$

$$A_3^{(0)} = -8Ohe \tag{D.16}$$

$$A_3^{(2)} = -2.5Ohe(1 + e^2) \tag{D.17}$$

$$A_3^{(4)} = -0.25Ohe^3 \tag{D.18}$$

$$A_4^{(0)} = 0.5e(1 + e^2) \tag{D.19}$$

$$A_4^{(2)} = 0.125e^3. \tag{D.20}$$

Appendix E

Coefficients of jet profile in equation (3.20) are as follows,

$$d_1 = -\frac{e\sqrt{e}}{\pi} E_4 \tag{E.1}$$

$$d_2 = \frac{e^2\sqrt{e}}{\pi}(E_1 - 3E_2) \tag{E.2}$$

$$d_3 = \frac{e^2\sqrt{e}}{\pi}(E_1 - 3e^2E_3) \tag{E.3}$$

$$d_4 = -\frac{e\sqrt{e}}{\pi} E_5 \tag{E.4}$$

$$d_5 = -\frac{e^2\sqrt{e}}{\pi} E_4 \tag{E.5}$$

$$d_6 = \frac{e^3\sqrt{e}}{\pi}(E_1 - 3E_2) \tag{E.6}$$

$$d_7 = \frac{e^2\sqrt{e}}{\pi}(E_1 - 3e^2E_3) \tag{E.7}$$

$$d_8 = -\frac{\sqrt{e}}{\pi} E_5 \tag{E.8}$$

Appendix F

Coefficients of spatial dispersion polynomial in equation (3.21) are given by,

$$b_0 = \beta^4 We^2 A_4^{(0)} + \beta^3 We^{1.5} A_3^{(0)} + \beta^2 We A_2^{(0)} \tag{F.1}$$

$$b_1 = -(4\beta^3 We^2 A_4^{(0)} + 3\beta^2 We^{1.5} A_3^{(0)} + 2\beta We A_2^{(0)}) \tag{F.2}$$

$$\begin{aligned} b_2 = {} & 6\beta^2 We^2 A_4^{(0)} + 3\beta We^{1.5} A_3^{(0)} + We A_2^{(0)} + \beta^4 We^2 A_4^{(2)} + \beta^3 We^{1.5} A_3^{(2)} + \beta^2 We A_2^{(2)} \\ & + \beta We^{0.5} A_1^{(2)} + A_0^{(2)} \end{aligned} \tag{F.3}$$

$$b_3 = -(4\beta We^2 A_4^{(0)} + We^{1.5} A_3^{(0)} + 4\beta^3 We^2 A_4^{(2)} + 3\beta^2 We^{1.5} A_3^{(2)} + 2\beta We A_2^{(2)} + We^{0.5} A_1^{(2)}) \tag{F.4}$$

$$\begin{aligned} b_4 = {} & We^2 A_4^{(0)} + 6\beta^2 We^2 A_4^{(2)} + 3\beta We^{1.5} A_3^{(2)} + We A_2^{(2)} + \beta^3 We^{1.5} A_3^{(4)} + \beta^2 We A_2^{(4)} \\ & + \beta We^{0.5} A_1^{(4)} + A_0^{(4)} \end{aligned} \tag{F.5}$$

$$b_5 = -(4\beta We^2 A_4^{(2)} + We^{1.5} A_3^{(2)} + 3\beta^2 We^{1.5} A_3^{(4)} + 2\beta We A_2^{(4)} + We^{0.5} A_1^{(4)}) \tag{F.6}$$

$$b_6 = We^2 A_4^{(2)} + 3\beta We^{1.5} A_3^{(4)} + We A_2^{(4)} + \beta^2 We A_2^{(6)} + \beta We^{0.5} A_1^{(6)} + A_0^{(6)} \tag{F.7}$$

$$b_7 = -(We^{1.5} A_3^{(4)} + 2\beta We A_2^{(6)} + We^{0.5} A_1^{(6)}) \tag{F.8}$$

$$b_8 = We A_2^{(6)} \tag{F.9}$$